

# System size and centrality dependence of thermal radiation measured by HADES

Abhängigkeit thermischer Strahlung von der Systemgröße und Zentralität

Master thesis by Niklas Schild

Datum: 09.08.2021, Date of submission: 09.08.2021

1. Review: Prof. Dr. Tetyana Galatyuk

2. Review: Dr. Szymon Harabasz

Darmstadt



TECHNISCHE  
UNIVERSITÄT  
DARMSTADT

Physics Department  
Institut für Kernphysik  
AG Galatyuk

---

## **Erklärung zur Abschlussarbeit gemäß §22 Abs. 7 und §23 Abs. 7 APB der TU Darmstadt**

---

Hiermit versichere ich, Niklas Schild, die vorliegende Masterarbeit ohne Hilfe Dritter und nur mit den angegebenen Quellen und Hilfsmitteln angefertigt zu haben. Alle Stellen, die Quellen entnommen wurden, sind als solche kenntlich gemacht worden. Diese Arbeit hat in gleicher oder ähnlicher Form noch keiner Prüfungsbehörde vorgelegen.

Mir ist bekannt, dass im Fall eines Plagiats (§38 Abs. 2 APB) ein Täuschungsversuch vorliegt, der dazu führt, dass die Arbeit mit 5,0 bewertet und damit ein Prüfungsversuch verbraucht wird. Abschlussarbeiten dürfen nur einmal wiederholt werden.

Bei der abgegebenen Thesis stimmen die schriftliche und die zur Archivierung eingereichte elektronische Fassung gemäß §23 Abs. 7 APB überein.

Bei einer Thesis des Fachbereichs Architektur entspricht die eingereichte elektronische Fassung dem vorgestellten Modell und den vorgelegten Plänen.

Darmstadt, 09.08.2021

---

Niklas Schild

---

# Abstract

---

Electromagnetic probes offer a unique opportunity to study the conditions in heavy-ion collisions throughout their whole evolution. Due to their lack of color charge, they can escape the strongly interacting medium without re-scattering and bring direct insights from the fireball to the surrounding detectors. Thermal dilepton pairs, emitted from the locally thermalised medium, are especially valuable in this regard. Their invariant mass distributions entail information about the temperature of the hot and dense fireball, while the integrated dilepton yield can be connected to the fireballs lifetime.

In this thesis, the invariant mass spectra of these thermal dilepton pairs are reconstructed for two heavy-ion collision experiments performed at HADES: Au+Au in April 2012 and Ag+Ag in March 2019, both at beam energies of  $\sqrt{s_{NN}} = 2.42$  GeV. This allows for an investigation of the thermal radiation not only in dependence of the centrality, but also of the system size. By extension of the Au+Au analysis to peripheral events up to 60% centrality, events of Au+Au and Ag+Ag with the same mean number of participants are identified and compared. In this way, any remaining differences in the dilepton signal can then be traced back to the underlying ion species of the collision.

Chapter 1 will introduce the foundations of heavy-ion collisions and the QCD phase diagram, as well as a discussion of electromagnetic probes. Chapter 2 will present the HADES experiment and the most important detector components. Chapter 3 will focus on the steps of the Ag+Ag analysis which were taken to reconstruct the invariant mass spectra. A large focus is set on the determination of necessary efficiency and acceptance corrections. Chapter 4 will introduce the additional challenges of the Au+Au analysis for peripheral events. In particular, the effect of Au+C contamination and a subsequent implementation of an event-purifier is examined. The finally resulting Ag+Ag and Au+Au invariant mass spectra are then evaluated in chapter 5. Here, the fireball temperature as well as the excess yield are determined. Chapter 6 provides a summary and outlook of the findings.

---

# Zusammenfassung

---

Elektromagnetische Sonden bieten eine einzigartige Möglichkeit, die Bedingungen in Schwerionenkollisionen während ihrer gesamten Entwicklung zu untersuchen. Da sie keine Farbladung haben, können sie dem stark wechselwirkenden Medium ohne weitere Streuung entkommen und damit direkte Erkenntnisse aus dem Feuerball zu den umliegenden Detektoren bringen. Thermische Dileptonenpaare, die aus dem lokal thermalisierten Medium emittiert werden, sind in dieser Hinsicht besonders wertvoll. Ihre invarianten Massenverteilungen liefern Informationen über die Temperatur des heißen und dichten Feuerballs, während die integrierte Dileptonenausbeute mit der Lebensdauer des Feuerballs in Verbindung gebracht werden kann.

In dieser Arbeit werden die invarianten Massenspektren dieser thermischen Dileptonenpaare für zwei am HADES durchgeführten Schwerionenkollisionsexperimente rekonstruiert: Au+Au im April 2012 und Ag+Ag im März 2019, beide bei Strahlenergien von  $\sqrt{s_{NN}} = 2.42$  GeV. Dies ermöglicht eine Untersuchung der thermischen Strahlung nicht nur in Abhängigkeit von der Zentralität, sondern auch von der Systemgröße. Durch Ausweitung der Au+Au Analyse auf periphere Kollisionsereignisse bis zu 60% Zentralität werden Kollisionen von Au+Au und Ag+Ag mit der gleichen mittleren Teilnehmerzahl identifiziert und verglichen. Auf diese Weise können alle verbleibenden Unterschiede im Dileptonensignal auf die der Kollision zugrunde liegenden Ionenspezies zurückgeführt werden.

In Kapitel 1 werden die Grundlagen der Schwerionenkollisionen und das QCD-Phasendiagramm vorgestellt, sowie elektromagnetische Sonden diskutiert. In Kapitel 2 wird das HADES-Experiment und dessen wichtigste Detektorkomponenten vorgestellt. Kapitel 3 konzentriert sich auf die Schritte der Ag+Ag Analyse, welche zur Rekonstruktion der invarianten Massenspektren durchgeführt wurden. Ein großer Schwerpunkt liegt dabei auf der Bestimmung der notwendigen Effizienz- und Akzeptanzkorrekturen. Kapitel 4 wird die zusätzlichen Herausforderungen der Au+Au Analyse für periphere Kollisionsereignisse vorstellen. Insbesondere wird die Auswirkung von Au+C Kontamination und die anschließende Implementierung eines Event-Purifiers untersucht. Die schließlich resultierenden Ag+Ag und Au+Au invarianten Massenspektren werden dann in Kapitel 5 ausgewertet. Dabei werden sowohl die Feuerballtemperatur als auch die Überschussausbeute bestimmt. Kapitel 6 gibt eine Zusammenfassung der Ergebnisse und einen Ausblick.

---

# Contents

---

<b>1</b>	<b>Introduction</b>	<b>1</b>
1.1	The Standard Model . . . . .	1
1.1.1	Running Coupling Constant . . . . .	2
1.1.2	Chiral Symmetry . . . . .	3
1.2	QCD Phase Diagram . . . . .	5
1.3	Heavy Ion Collisions . . . . .	6
1.3.1	Glauber Monte Carlo Model . . . . .	8
1.3.2	Centrality Determination . . . . .	9
1.4	Dileptons as Probe of Hot and Dense Matter . . . . .	11
1.4.1	Dilepton Sources . . . . .	11
1.4.2	Dilepton Emission . . . . .	12
1.5	Goal of this Analysis . . . . .	12
<b>2</b>	<b>HADES</b>	<b>13</b>
2.1	START Detector and Target . . . . .	13
2.2	Ring Imaging Cherenkov Detector . . . . .	14
2.3	Multiwire Drift Chamber and Magnet . . . . .	15
2.4	Multiplicity Electron Trigger Array . . . . .	15
2.5	Electromagnetic Calorimeter . . . . .	15
2.6	Data Summary Tape . . . . .	16
<b>3</b>	<b>Analysis of Ag+Ag Data</b>	<b>17</b>
3.1	Event Selection . . . . .	18
3.1.1	Centrality Selection . . . . .	18
3.2	Lepton Identification . . . . .	20
3.2.1	Relativistic Mass Cut . . . . .	20
3.2.2	Spatial Correlation between RICH Ring Center and MDC Track . . . . .	21
3.2.3	Conversion and Opening Angle Cut . . . . .	24
3.3	Estimation of Combinatorial Background . . . . .	24
3.4	Acceptance and Efficiency Corrections . . . . .	28
3.4.1	Single Lepton Efficiencies . . . . .	28
3.4.2	Momentum Smearing . . . . .	29
3.4.3	Pair Efficiency Corrections . . . . .	31
3.4.4	Freeze-out Cocktail Multiplicities . . . . .	33
3.4.5	Comparison of Dilepton Cocktail to Data . . . . .	35
3.4.6	Acceptance Corrections . . . . .	38

---

<b>4</b>	<b>Analysis of Au+Au Data</b>	<b>40</b>
4.1	Differences to the Ag+Ag Analysis . . . . .	40
4.1.1	Inclusion of PT2 Events . . . . .	40
4.1.2	Lepton Identification via Multivariate Analysis . . . . .	41
4.2	Removal of Au+C Contamination . . . . .	41
4.2.1	Functionality of Event-Purifier . . . . .	43
4.2.2	Effects of the Event-Purifier . . . . .	43
4.2.3	Influence of Purifier on Centrality Selection . . . . .	46
4.3	Isolation of Excess Pairs . . . . .	47
4.4	Estimation of Systematic Uncertainties . . . . .	49
<b>5</b>	<b>Evaluation of Dilepton Invariant Mass Spectra</b>	<b>50</b>
5.1	Comparison of Excess Spectra between System Sizes . . . . .	52
5.2	Excess Yield Dependence on System Size and Centrality . . . . .	54
5.3	Temperature Dependence on System Size and Centrality . . . . .	56
5.4	Comparison to UrQMD Simulations . . . . .	57
<b>6</b>	<b>Summary and Outlook</b>	<b>59</b>

---

# List of Figures

---

1.1	Summary of the Standard Model. . . . .	2
1.2	Energy dependence of the strong coupling constant. . . . .	3
1.3	Comparison of vacuum $\rho$ and $a_1$ spectral function. . . . .	4
1.4	Evolution of chiral partners particle spectra. . . . .	5
1.5	QCD phase diagram. . . . .	6
1.6	Evolution of heavy-ion collisions. . . . .	7
1.7	Excess yield ratio for various collision systems. . . . .	8
1.8	Cross section as function of $N_{TOF+RPC}$ for Au+Au (left panel) and Ag+Ag (right panel) collisions. . . . .	10
2.1	Schematic Layout of the HADES experiment. . . . .	13
2.2	Photos of gold (left panel) and silver (right panel) targets segmented into 15 target foils. . . . .	14
3.1	Schematic overview of analysis steps needed for the reconstruction of the invariant mass spectra. . . . .	17
3.2	Number of events in dependence of event selection criteria for Ag+Ag collisions at $\sqrt{s_{NN}} = 2.42$ GeV. . . . .	19
3.3	Momentum dependent lepton mass cut. . . . .	21
3.4	Lepton distribution over $\Delta\Theta$ for Ag+Ag collisions at $\sqrt{s_{NN}} = 2.42$ GeV. . . . .	22
3.5	Mean and standard deviation of $\Delta\Theta$ distributions over $\Theta$ for Ag+Ag collisions at $\sqrt{s_{NN}} = 2.42$ GeV. . . . .	23
3.6	Number of particle candidates over RICH matching quality and momentum before and after RICH ring quality cut for Ag+Ag collisions, 0-40% centrality, at $\sqrt{s_{NN}} = 2.42$ GeV. . . . .	23
3.7	Number of particles over charge momentum and velocity before and after lepton selection for Ag+Ag collisions, 0-40% centrality, at $\sqrt{s_{NN}} = 2.42$ GeV. . . . .	24
3.8	Charge asymmetry factor $k$ (left panel) and ratio of mixed-event to same-event combinatorial background (right panel) in dependence of invariant mass $M_{ee}$ for Ag+Ag collisions, 0-40% centrality, at $\sqrt{s_{NN}} = 2.42$ GeV. . . . .	26
3.9	Example of combinatorial background subtraction and the resulting signal for Ag+Ag collisions, 0-40% centrality, at $\sqrt{s_{NN}} = 2.42$ GeV. . . . .	27
3.10	Signal to background ratio (left panel) and significance (right panel) as a function of invariant mass for Ag+Ag collisions, 0-40% centrality, at $\sqrt{s_{NN}} = 2.42$ GeV. . . . .	27
3.11	Single lepton efficiencies projected on the momentum for Ag+Ag collisions, 0-40% centrality, at $\sqrt{s_{NN}} = 2.42$ GeV. . . . .	29
3.12	Distributions of ideal vs reconstructed momentum of electrons at $0^\circ < \theta < 35^\circ$ for Ag+Ag collisions at $\sqrt{s_{NN}} = 2.42$ GeV. . . . .	30
3.13	Single lepton efficiencies with and without smearing for Ag+Ag collisions, 0-40% centrality, at $\sqrt{s_{NN}} = 2.42$ GeV. . . . .	31
3.14	Pair efficiency factors in dependence of the invariant mass for Ag+Ag collisions, 0-40% centrality, at $\sqrt{s_{NN}} = 2.42$ GeV. . . . .	32

3.15	Mean pair efficiency factors with embedding to UrQMD vs embedding to real data in dependence of the invariant mass for Ag+Ag collisions, 0-40% centrality, at $\sqrt{s_{NN}} = 2.42$ GeV. . . . .	33
3.16	$\eta$ and $\pi^0$ multiplicity for different systems and energies. . . . .	34
3.17	Efficiency corrected signal in comparison with Pluto cocktail for Ag+Ag collisions, 0-40% centrality, at $\sqrt{s_{NN}} = 2.42$ GeV. . . . .	36
3.18	Efficiency corrected signal in comparison with Pluto cocktail for Ag+Ag collisions at $\sqrt{s_{NN}} = 2.42$ GeV. . . . .	37
3.19	Single lepton acceptances projected on $\phi$ and $p$ for Ag+Ag collisions, 0-40% centrality, at $\sqrt{s_{NN}} = 2.42$ GeV. . . . .	38
3.20	Pair acceptance factor in dependence of the invariant mass for Ag+Ag collisions at $\sqrt{s_{NN}} = 2.42$ GeV. . . . .	39
4.1	Event Counter for different centrality classes with and without the effects of the down scaling procedure for Au+Au collisions at $\sqrt{s_{NN}} = 2.42$ GeV. . . . .	41
4.2	Events vertex positions in x-z plane for Au+Au collisions at $\sqrt{s_{NN}} = 2.42$ GeV. . . . .	42
4.3	Number of events over number of TOF+RPC hits for Au+Au collisions at $\sqrt{s_{NN}} = 2.42$ GeV. . . . .	44
4.4	Number of events over number of TOF+RPC hits with different purifier settings for Au+Au collisions at $\sqrt{s_{NN}} = 2.42$ GeV. . . . .	45
4.5	Number of events per centrality class with different purifier settings for Au+Au collisions at $\sqrt{s_{NN}} = 2.42$ GeV. . . . .	45
4.6	Comparison of cross section as function of $N_{TOF+RPC}$ with different purifier settings for Au+Au collisions at $\sqrt{s_{NN}} = 2.42$ GeV. . . . .	47
4.7	Relative systematic errors over mass due to extrapolated $\eta$ -spectrum for peripheral Au+Au collisions at $\sqrt{s_{NN}} = 2.42$ GeV. . . . .	48
5.1	Acceptance corrected excess spectrum and temperature Boltzmann fit, see equation 5.2, for Ag+Ag collisions at $\sqrt{s_{NN}} = 2.42$ GeV. . . . .	50
5.2	Acceptance corrected excess spectrum and temperature Boltzmann fit, see equation 5.2, for Au+Au collisions at $\sqrt{s_{NN}} = 2.42$ GeV. . . . .	51
5.3	Reconstructed invariant mass spectrum of excess pairs. Au+Au is from 0-60% centrality. Ag+Ag is from 0-40% centrality. . . . .	52
5.4	Reconstructed invariant mass spectrum of excess pairs. Au+Au is from 30-40% centrality. Ag+Ag is from 10-20% centrality. . . . .	53
5.5	Excess yield of Au+Au collisions over $\langle A_{part} \rangle$ with different purifier settings. . . . .	54
5.6	Excess yield over $\langle A_{part} \rangle$ of Au+Au vs Ag+Ag collisions. . . . .	55
5.7	Fireball temperature of Au+Au collisions over $\langle A_{part} \rangle$ with different purifier settings. . . . .	56
5.8	Fireball temperature over $\langle A_{part} \rangle$ of Au+Au vs Ag+Ag collisions. . . . .	57
5.9	UrQMD predictions of the invariant mass spectrum in Ag+Ag and Au+Au collisions at the same energy of 1.23AGeV and centrality of 0-10 %. The right panel shows their ratio . . . . .	58

---

# List of Tables

---

1.1	Average number of participants for various centrality classes and Au+Au and Ag+Ag collision systems. . . . .	7
1.2	Summary of vector mesons properties. . . . .	11
3.1	Centrality class definitions based on the number of measured hits $N_{TOF+RPC}$ for Ag+Ag collisions at $\sqrt{s_{NN}} = 2.42$ GeV. . . . .	19
3.2	Freeze out cocktail sources for Ag+Ag at $\sqrt{s_{NN}} = 2.42$ GeV. . . . .	35
4.1	Decision thresholds for different Purifier settings. . . . .	44
4.2	Centrality class definitions for Au+Au collisions at $\sqrt{s_{NN}} = 2.42$ GeV. . . . .	46

---

# 1 Introduction

---

## 1.1 The Standard Model

---

Today, it is believed that the entire visible universe is made out of only a handful of elementary particles interacting via four fundamental interactions: Gravitation, electromagnetism, the weak and strong interaction. While gravity is explained by Einsteins general relativity, the remaining three forces are all described in one overarching theory, the Standard Model. Here, every interaction is understood by the exchange of a virtual particle with spin one. For electromagnetic interactions, this is the photon. For weak interactions, it is the W and Z Boson. For the strong force, it is the gluon. In all instances, these force carriers are referred to as gauge bosons. In addition, there are fermions which act as the building blocks of atoms and all visible matter in the universe. The Standard Model assumes two groups of elementary fermions. On the one hand, the quarks, which carry color charge and can interact via all four fundamental forces. On the other hand, the leptons, which carry no color charge and are "blind" to strong interactions.

The last fundamental particle to complete our current understanding of the Standard Model is the Higgs Boson. Originally proposed by Peter W. Higgs in 1964[1], it is a scalar boson with spin zero, whose underlying quantum field gives mass to the other elementary particles. While a number of questions remain unexplained by the Standard Model [2], the observation of the Higgs Boson in 2012 [3] serves as conformation of the described particle picture and lead to the bestowal of the Nobel prize in physics in 2013 [4].

A summary of the Standard Model can be seen in figure 1.1.

Mathematically, the Standard Model is build upon relativistic quantum field theory. For instance, electromagnetic interactions can be described by quantum electrodynamics (QED). In this case, the Lagrangian is written as [6]:

$$\mathcal{L}_{QED} = \bar{\psi}(i\gamma^\mu \mathcal{D}_\mu - m)\psi - \frac{1}{4}F_{\mu\nu}F^{\mu\nu} \quad (1.1)$$

Where  $F_{\mu\nu} = \partial_\mu A_\nu - \partial_\nu A_\mu$  is the electromagnetic field tensor and  $D_\mu = \partial_\mu + ieA_\mu$  is the covariant derivative. One can further identify  $e$  as the electric charge which acts as the underlying property to allow electromagnetic interactions.

In a similar vein, the strong force is described by the theory of quantum chromodynamics (QCD). Its Lagrangian can be written as [7]:

$$\mathcal{L}_{QCD} = \bar{\psi}_i(i(\gamma^\mu \mathcal{D}_\mu)_{ij} - m\delta_{ij})\psi_j - \frac{1}{4}G_{\mu\nu}^a G_a^{\mu\nu} \quad (1.2)$$

Where, analogous to  $F_{\mu\nu}$ , one can identify the gluon field tensor  $G_{\mu\nu}^a$ :

$$G_{\mu\nu}^a = \partial_\mu A_\nu^a - \partial_\nu A_\mu^a + gf^{abc}A_{\mu a}^b A_{\nu c}^a \quad (1.3)$$

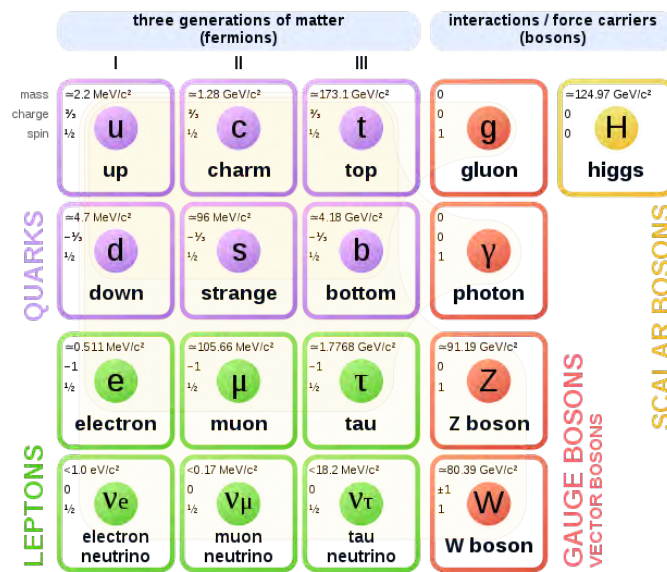


Figure 1.1: Summary of the Standard Model of particle physics. All known fundamental particles and their properties are shown. One can identify four different types of particles in the quarks, leptons, gauge bosons and scalar bosons. Figure taken from [5].

At first glance, the Lagrangians of QCD and QED show a similar mathematical form. However, at closer inspection, a key difference can be identified in equation 1.3. Gluons, acting as gauge bosons, carry color charge which allows them to interact with other gluons. This is in stark contrast to QED, where self-interaction of photons is impossible. Mathematically, this is described in the additional term in equation 1.3 and the dependence on a structure constant  $f^{abc}$ .

This fact gives rise to a number of particular behaviors and characteristics unique to the strong interaction.

### 1.1.1 Running Coupling Constant

In the Standard Model, the strength of an interaction is determined by a coupling constant. There is the weak coupling constant  $\alpha_w$ , electromagnetic coupling constant  $\alpha_{em}$ , and strong coupling constant  $\alpha_s$ . In all cases, the magnitude of these constants depends on the momentum transfer  $Q^2$  between the two interacting particles, a phenomenon known as running coupling constants. This can be seen in figure 1.2 for the example of the strong coupling constant. It turns out that this dependency of  $\alpha_s$  on  $Q^2$  is by far the greatest relative to running coupling of other forces. This, in turn, gives rise to two distinct properties of QCD.

On the one hand, the principle of confinement, which dictates that color charged particles can not be encountered isolated, but only in color neutral configurations, i.e. hadrons. It can be understood as the result of the increasing force for longer and longer distances. The energy required to separate a quark from a colorless hadron will eventually exceed the necessary production energy of a quark-antiquark pair. Hence, it leads to the creation of a new quark pair and the renewed formation of colorless hadrons.

On the other hand, a strongly interacting particle can move almost freely at high energies and correspondingly small distances. Consequently, the state of matter can change from the hadronic phase to the so-called quark-gluon plasma (QGP). Here, a distinction between hadrons can longer be made because quarks and

gluons, from formerly different hadrons, interact directly. This gives rise to some interesting occurrences which are discussed in more detail in section 1.2.

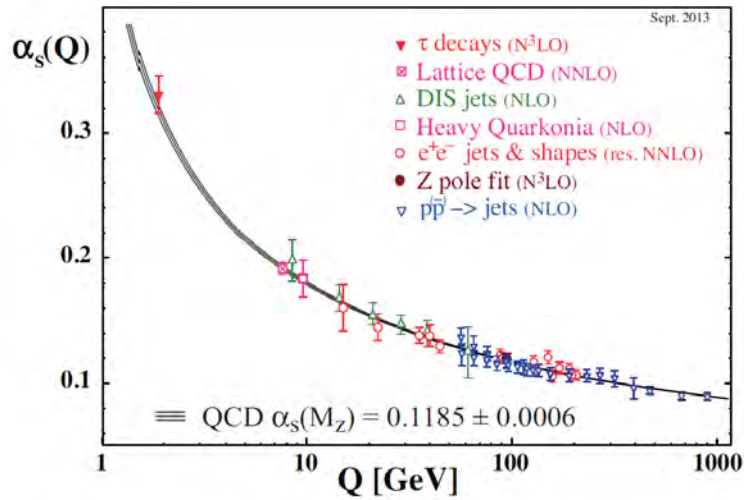


Figure 1.2: Energy dependence of the strong coupling constant  $\alpha_s$ . Data points indicate measurements made at varying energies, while the continuous lines represent QCD predictions assuming  $\alpha_s(M_z) = 0.1185 \pm 0.0006$ . Figure taken from [8].

### 1.1.2 Chiral Symmetry

Chiral Symmetry is characterised by the invariance of the Lagrangian under chiral transformations [9]. In general, the QCD Lagrangian breaks this symmetry explicitly by the non-vanishing quark masses  $m_q \neq 0$ . Yet, the approximate chiral symmetry with the assumption of  $m_q = 0$  allows insights into otherwise unexplained experimental observations, namely the mass splitting between two chiral partners, e.g. comparing  $\rho$  mesons at  $775 \text{ MeV}/c^2$  [8] to  $a_1$  mesons at  $1260 \text{ MeV}/c^2$  [8]. This observation can be understood by the spontaneous symmetry breaking of chiral symmetry.

A symmetry is spontaneously broken if the Hamiltonian fulfils the symmetry except for the ground state. In the vacuum, quark-antiquark pairs are created constantly and make up a quark condensate. This condensate carries a chiral charge leading to the spontaneous breaking of chiral symmetry. Experimentally, the strength of this breaking can be investigated by comparing the properties of two chiral partners. Figure 1.3 shows the spectral functions for  $\rho$  and  $a_1$  which clearly have separate masses in the vacuum.

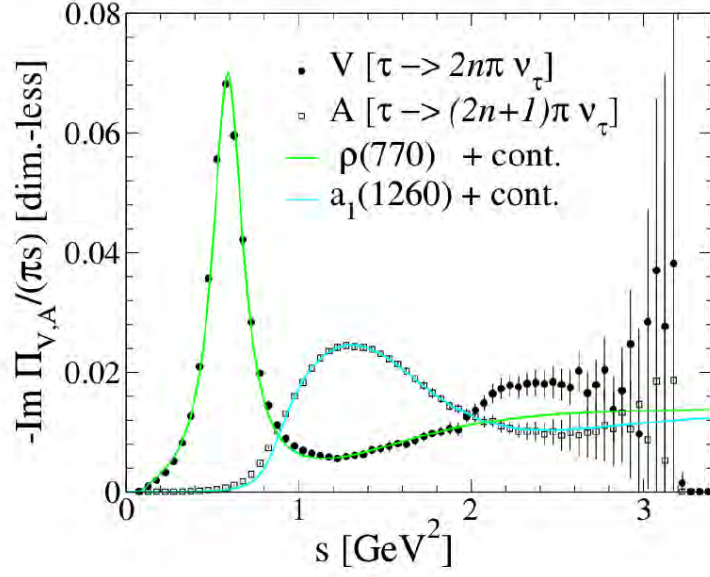


Figure 1.3: Comparison of vacuum  $\rho$  and  $a_1$  spectral function. Black points indicate measurements made of the vectormeson  $V$  and axial-vector meson  $A$  from  $\tau$  decays [10], while the continuous lines represent fits using the spectral functions [11]

If the reason for the observed mass gap is the spontaneous chiral symmetry breaking due to the quark condensate, one could expect the chiral partner masses to converge once the quark condensates decreases. Such a decrease of the quark condensate is predicted by various models [12, 13, 14] with increasing temperatures and densities. Further calculations [16, 15] additionally investigate possible impacts and signatures of the chiral symmetry restoration on the spectral functions. This is demonstrated in figure 1.4 [16] for  $\rho$  and  $a_1$ . It indicates two important possible effects:

First, the mass of the axial-vector  $a_1$  meson is dropping with increasing temperatures. One can identify a shift of its spectral shape peak towards the ground state, i.e.  $\rho$ . Second, an overall melting of the spectral functions is noticeable, especially for the  $\rho$  meson. While the overall mass stays the same, the spectral functions broadens towards a flat continuum. In the end, both effects may contribute to a convergence of the spectral functions.

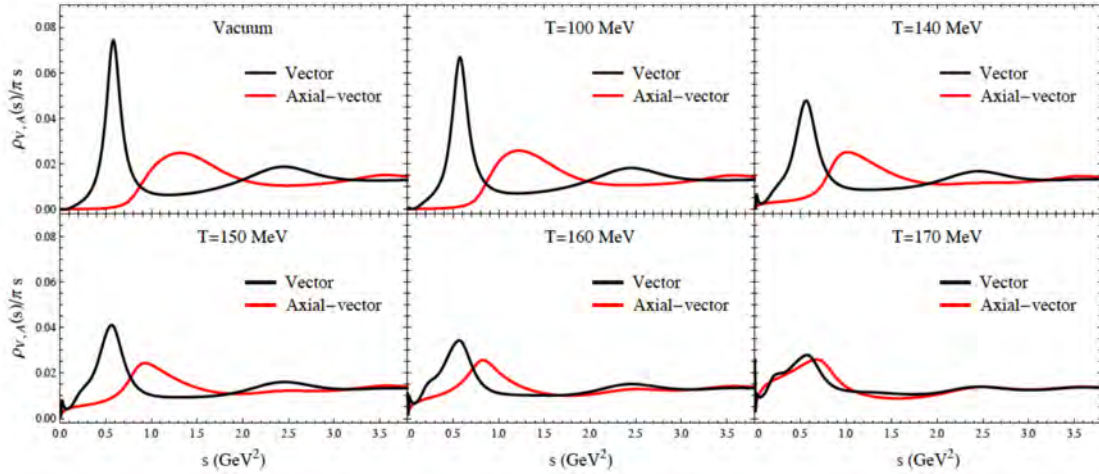


Figure 1.4: Evolution of chiral partners particle spectra with increasing temperature. Figure taken from [16].

## 1.2 QCD Phase Diagram

The ultimate goal in QCD will be a full understanding of strongly interacting matter and its behavior in all conditions. For one, this will mean describing the formation of hadronic matter when quarks and gluon form nucleons. For another, one expects a phase transition with increasing temperatures and densities, which will lead to the formation of new phases of matter. This is most notably the previously mentioned quark-gluon plasma. Currently, a great effort is put into reproducing these extreme states in the laboratory to identify how this transition is taking place. The current picture of the QCD phase diagram is shown in figure 1.5. Lattice QCD calculations predict a crossover region at high temperatures and baryochemical potentials close to zero. The central question to be answered is how far this crossover extends to higher baryochemical potentials, or if it turns into a first order phase transition with a critical point [17].

The study of the QCD phase diagram gives insights into the behavior of strongly interacting matter at extreme conditions, as they were present during very early times of the universe, or are still found today in compact stellar objects. One of the tools to indicate a deconfinement transition, is potentially the observation of chiral symmetry restoration discussed in the previous section.

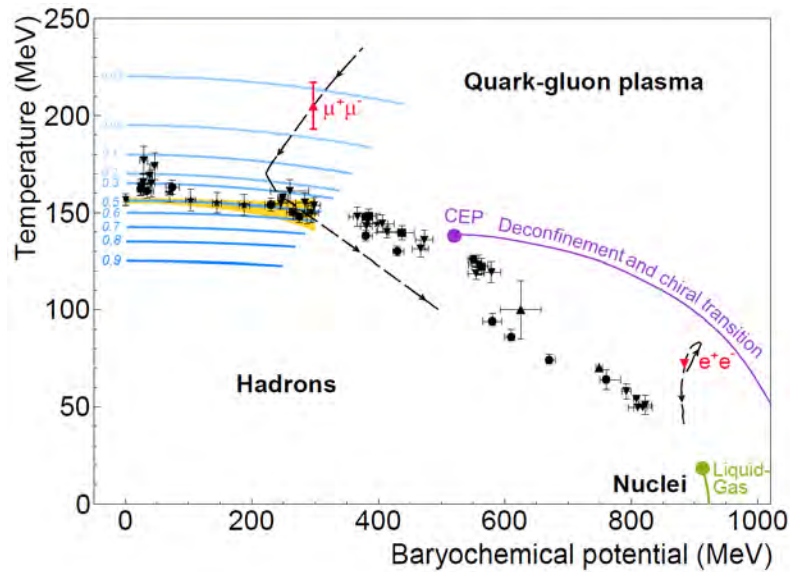


Figure 1.5: QCD phase diagram. Black points show measurements from various experiments worldwide. Depending on the collision system and available energies, different temperatures and baryochemical potentials can be reached. At HADES, heavy-ion collisions with energies of a few GeV per nucleon lead to baryochemical potentials of several hundred MeV with temperatures below 100 MeV. Hence, it investigates the regions of the QCD phase diagram relevant for neutron star mergers. In contrast, high temperatures at low baryochemical potentials are characteristic for the conditions in the early universe. Here, the yellow band represents the crossover region as predicted by Lattice QCD. A possible transition with the critical point CEP is shown in purple. Blue lines show theoretical estimations of the chiral condensate which decreases with increasing temperatures [16].

### 1.3 Heavy Ion Collisions

Heavy ion collisions serve as the central tool to produce and investigate extreme matter conditions in the laboratory. In general, one can identify three distinct stages that such a collision goes through:

- **First-chance NN collisions:** Before two colliding nuclei fully overlap, there are first-chance NN-collisions between individual nucleons (left panel of figure 1.6).
- **Hot and dense fireball:** At the height of the collision, the most extreme conditions in terms of temperature and density are reached. This is called the hot and dense fireball and it is in this stage of hot and dense hadron phases that a quark-gluon plasma is potentially created (middle panel of figure 1.6).
- **Freeze out:** In time, the whole system expands and cools down. First, the individual quarks from the potential QGP will hadronise again. These hadrons might scatter inelastically with themselves, creating excited states and new particles. The end of inelastic scattering marks the point of chemical freeze out. Once elastic scattering ceases as well, the so-called kinetic freeze out is reached (right panel of figure 1.6).

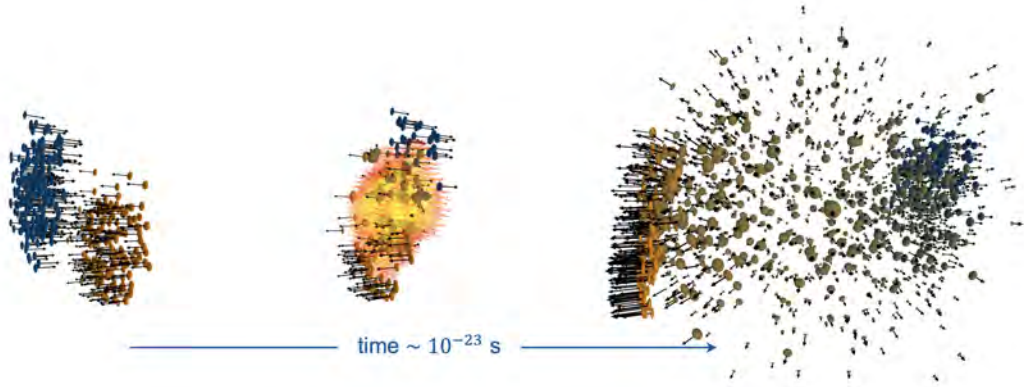


Figure 1.6: Evolution of heavy-ion collisions.

The produced particles are then detected in surrounding detector facilities. Based on their properties, one can draw conclusions about the state of matter during their creation.

The temperatures and densities reached in a heavy-ion collision depend on a number of factors. First and foremost, the beam energy determines how much energy will be available in the system. Therefore, it dictates directly the maximum mass of produced particles and which particles are most likely to be found.

In addition, another key characteristic is the centrality in which a collision is taking place. One can define an impact parameter  $b$  as the distance between the center of the nuclei in a plane transverse to the beam [18]. Small impact parameter translate to central collisions where most nucleons within one nucleus will hit and interact with nucleons from the other nucleus. It is intuitive that a large number of participating nucleons  $\langle A_{part} \rangle$  will reflect in higher multiplicities of outgoing and detected particles. In contrast, a large impact parameter means only a few nucleons on the edge of nucleus will take part in the collision. This leads to less extreme conditions and fewer produced particles. The remaining nucleons, which are not contributing to the collision, are referred to as spectators. The centralities of Au+Au and Ag+Ag collisions, as they are discussed in this work, can be summarised in table 1.1. The underlying method to identify the number of participants per centrality class is described in the following sections 1.3.1 and 1.3.2.

Centrality class [%]	$\langle A_{part} \rangle^{AuAu}$	$\langle A_{part} \rangle^{AgAg}$
0-10	303	<b>168</b>
10-20	213	<b>103</b>
20-30	<b>150</b>	76
30-40	<b>103</b>	53
40-50	68	<b>33</b>
50-60	<b>42</b>	
<b>0-40</b>	193	<b>102</b>
<b>0-50</b>	<b>165</b>	

Table 1.1: Average number of participants for various centrality classes and Au+Au and Ag+Ag collision systems. Matching centrality classes with approximately the same average number of participants are colored. They serve as possibilities to compare dilepton radiation for different systems at the same  $\langle A_{part} \rangle$ .

Together, the collision centrality as well as the beam energy are arguably the two major determinants for the conditions reached in heavy-ion collisions. However, a last important contribution might also be the ion species. It defines the shape of nuclei, as well as the total system size and maximum number of participating nucleons. The question arises, if a collision of two different systems, but at the same energy and with the same number of participating nucleons, leads to the same outcomes. A first approach to investigate this has been made at HADES by comparing the dilepton yield of several system sizes. In figure 1.7 the excess yield ratio  $R_{AA}$  is shown. Here, the spectrum of any A+A collision is normalised by the elementary reference spectrum of single nucleon-nucleon collisions N+N as well as  $\langle A_{part} \rangle$  [19]:

$$R_{AA} = \frac{1}{\langle A_{part}^{AA} \rangle} \frac{dN^{AA}}{dM_{ee}} \left( \frac{dN^{NN}}{dM_{ee}} \right)^{-1} \quad (1.4)$$

This normalisation allows for a comparison of the yield between different system. Beyond the  $\pi^0$  mass region, a clear dependence on the system size is found. The heavier ions of Au+Au and Ar+KCl show a clear excess yield in comparison to elementary N+N collisions and light ions like C+C.

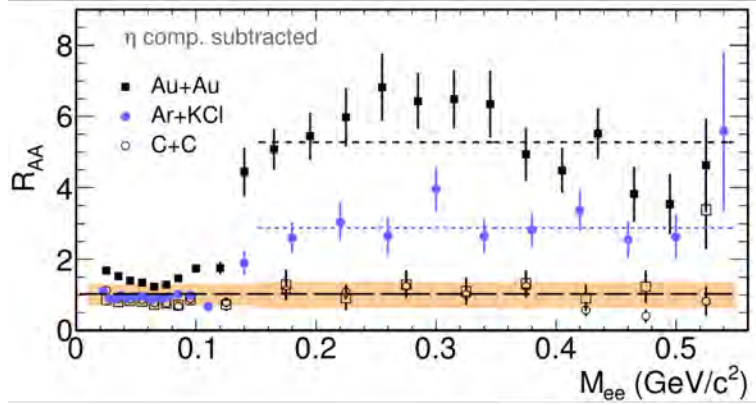


Figure 1.7: Ratio  $R_{AA}$  over invariant mass for various collision systems. Vertical bars represent the statistical errors while the yellow band represents the systematic uncertainties. The two dashed lines correspond to the average excess ratio. Figure taken from [19].

### 1.3.1 Glauber Monte Carlo Model

In a collision experiment, the impact parameter  $b$  is not directly observable. Instead, the measured overall particle multiplicity  $N$  at the detector can be employed to draw conclusions about the underlying centrality. Assuming  $N$  to be directly proportional to  $\langle A_{part} \rangle$ , the centrality  $C$  is defined as the fraction of the total cross section  $\sigma_{AA}$  [18]:

$$C \approx \frac{1}{\sigma_{AA}} \int_{N^{thr}}^{\infty} \frac{d\sigma}{dN'} dN' \quad (1.5)$$

Where  $N^{thr}$  is the lower multiplicity threshold of a given centrality class.

Therefore, the challenge then lies in estimating  $\sigma_{AA}$  as well as relating the centrality bins to the underlying  $\langle A_{part} \rangle$  and impact parameter  $b$ . For the centralities shown in table 1.1, the general framework for this determination is based on the Glauber Monte Carlo approach [18].

The Glauber model provides a theoretical description of heavy-ion collisions. It assumes that nucleons at sufficiently high energies have such large momenta that they will traverse essentially undeflected and that the motion of individual nucleons is independent of the full nucleus [20]. This is established well for higher energies of around  $\sqrt{s_{NN}} \geq 10$  GeV [18], but newer investigations support the validity of these assumptions even to lower energies [21].

With this in mind, the central idea is to describe the whole collision as the sum of independent binary collisions between individual nucleons. First, a random impact parameter  $b$  is sampled from a probability distribution  $P(b)$ . Based on this impact parameter, two colliding nuclei are simulated by generating individual nucleons. These nucleons are assigned a random position in 3d space based on  $b$  as well as the shape of nucleus. In the end, two nuclei with randomly distributed nucleons but separated by a given impact parameter are assembled. Finally, when the two nuclei are moved along the beam axis, a decision is made whether two approaching nucleons collide via the black disk approximation. It states that the impact parameter  $b_{NN}$  between the two potentially colliding nucleons has to be smaller than the inelastic nucleon-nucleon cross section  $\sigma_{inel}^{NN}$  [18]:

$$b_{NN} \leq \sqrt{\frac{\sigma_{inel}^{NN}}{\pi}} \quad (1.6)$$

In the end, every nucleon which fulfils this criterion is counted to the overall sum of participating nucleons  $A_{part}$ . The number of nucleons which do not undergo any collision are marked as spectators  $A_{spec}$ .

The input needed for the Glauber Monte Carlo model is threefold. First, a uniform distribution between 0 and  $b_{max}$  is used for sampling of the impact parameter. Hereby,  $b_{max}$  is given by the sum of radii from projectile and target nucleus. These radii, as well as the whole radial charge distribution of the nuclei, are the second input. For the Au+Au and Ag+Ag analysis, a two-parameter Fermi distribution is used for parameterisation:

$$\rho(r) = \frac{1 + w(r/R)^2}{1 + \exp(\frac{r-R}{a})} \quad (1.7)$$

Where  $R_{Au} = 6.55$  fm and  $a_{Au} = 0.52$  fm for gold nuclei and  $R_{Ag} = 5.3$  fm and  $a_{Ag} = 0.52$  fm for silver nuclei [18]. The parameter  $w$  is set to zero. In addition to this description, a last constraint is made by requiring a minimum separation between two nucleons at  $d_{min} = 0.9$  fm. Finally, the third input are the nucleon-nucleon cross sections  $\sigma_{inel}^{pp}$  and  $\sigma_{inel}^{np}$  for proton-proton and nucleon-proton scattering respectively. They are known from experiments [8] and set to  $\sigma_{inel}^{pp} = 26.4$  mb and  $\sigma_{inel}^{np} = 21.0$  mb.

### 1.3.2 Centrality Determination

The results from the Glauber Monte Carlo simulation give access to the relationship between the number of participating nucleons  $\langle A_{part} \rangle$  and the impact parameter  $b$ . They also give an estimation of the total cross section, e.g.  $\sigma_{AA} = 6833 \pm 430$  mb has been determined for Au+Au collisions at  $\sqrt{s_{NN}} = 2.42$  GeV [18]. In

the next step, the number of participating nucleons  $\langle A_{part} \rangle$  can then be related to the actually measurable charged particle multiplicity  $N_{ch}$  on the basis of the wounded nucleon assumption:

$$\langle N_{ch} \rangle = \mu \langle A_{part} \rangle \quad (1.8)$$

It states that the number of produced charged particles is, on average, proportional to the number of participants. In order to allow for event-by-event fluctuations from this average, an additional sampling via a negative binomial probability distribution (NBD) is made:

$$P_{\mu,k}(n) = \frac{\Gamma(n+k)}{\Gamma(n+1)\Gamma(k)} \cdot \frac{(\mu/k)^n}{(\mu/k+1)^{n+k}} \quad (1.9)$$

Where  $\Gamma$  is the gamma function and  $k$  a dispersion parameter.

Furthermore, a last addition to equation 1.8 is made with an efficiency term  $\epsilon(\alpha)$ , which describes reconstruction inefficiencies as well as secondary particle production:

$$\epsilon(\alpha) = 1 - \alpha A_{part}^2 \quad (1.10)$$

By combination of all these components, the  $A_{part}$  distribution from the Glauber Monte Carlo simulations can then be fitted to the distribution of measured events over  $N_{ch}$ . The fit parameters are  $\mu$ ,  $k$  and  $\alpha$ . Figure 1.8 shows the resulting fit on the Au+Au and Ag+Ag data which will be discussed in this work. As indicated in equation 1.5, the integral over  $d\sigma/dN$  gives access to the centrality classes via the measured charged particle multiplicity.

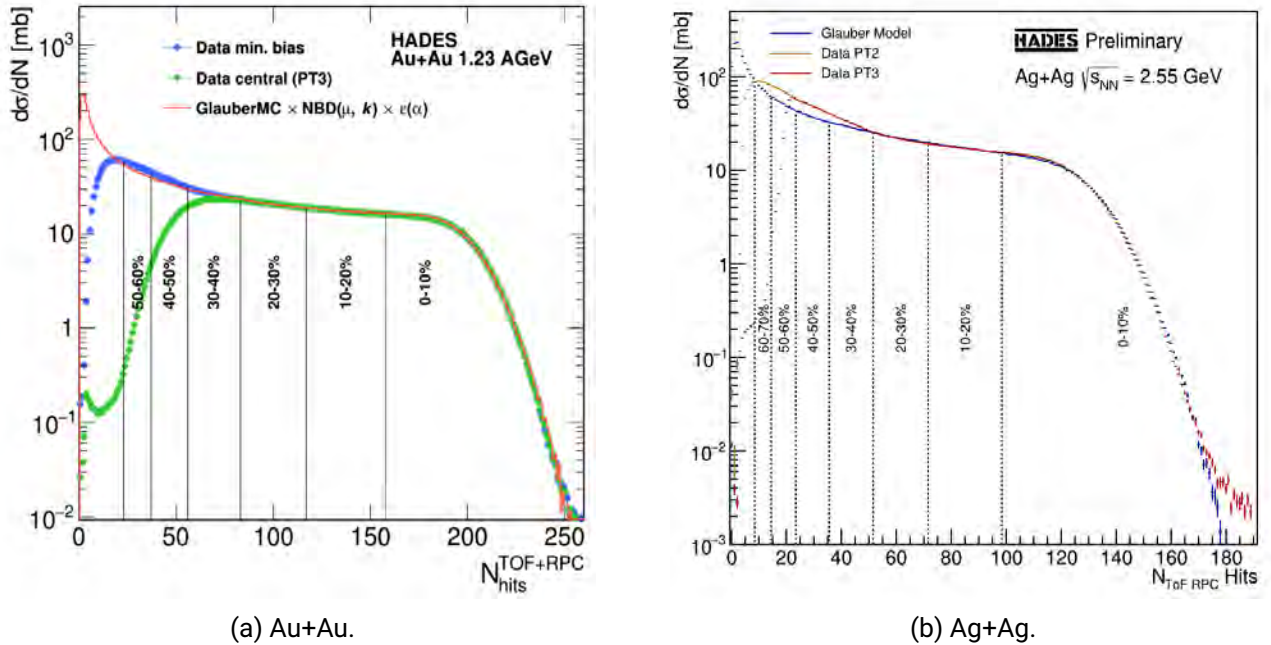


Figure 1.8: Cross section as function of  $N_{TOF+RPC}$  for Au+Au (left panel) and Ag+Ag (right panel) collisions.  $N_{TOF+RPC}$  can be identified as the number of measured charged particles  $N_{ch}$  at HADES.

---

## 1.4 Dileptons as Probe of Hot and Dense Matter

---

Typically, the greatest interest in today's research is to characterise the hottest and densest phase in a heavy-ion collision. Several observables have been introduced to access various stages of a collision, for example hadron yields, hadron flows or hadron correlations and fluctuations. However, all that is detectable in practice are the produced particles after the whole evolution of the collision has ended. By this time, due to elastic and inelastic scattering in the final stages, most strongly interacting particles will have lost most, if not all, direct information about the conditions at the early stages of the heavy-ion collision. Only a probe which is undisturbed by the strongly interacting medium can deliver immediate information from the time of its creation.

Leptons, or more precisely  $e^+e^-$  dilepton pairs from virtual photons, as well as real photons can fulfil this requirement. As mentioned in section 1.1, they do not interact strongly, which makes them blind to the further scattering in other stages of the reaction. Consequently, once created, they can reach the detector largely unhindered.

### 1.4.1 Dilepton Sources

In the course of a heavy-ion collision dileptons are produced via a number of varying processes and different decays. For SIS-18 energies of about 1-2A GeV one can identify the following: First, in the first-chance NN-collisions, Bremsstrahlung and  $\Delta$  Dalitz decays produce dileptons. Then, during the hottest and densest phase, vector mesons  $\rho$ ,  $\omega$ ,  $\phi$  and higher baryonic resonances are formed. With the branching ratios and lifetimes listed in table 1.2, they serve as potential dilepton sources which probe the hot and dense medium. Finally, during the freeze out stages,  $\pi^0$  and  $\eta$  mesons decaying into dileptons can be identified as the main sources.

It can be noted, that virtual photons are produced in every stage of the collision. As a consequence, any dilepton signal will always serve as an integral over the whole evolution of the collision. If the fireball is the region of interest, the contributions from NN-collisions and sources from freeze out stages need to be subtracted.

Particle	Mass [MeV/c <sup>2</sup> ]	Branching Ratio: $e^+e^-$	Lifetime [fm/c]
$\rho$	775	$4.72 \cdot 10^{-5}$	1.32
$\omega$	783	$7.28 \cdot 10^{-5}$	23.4
$\phi$	1019	$2.95 \cdot 10^{-4}$	46.2

Table 1.2: Summary of vector mesons properties [8]

Table 1.2 indicates one of the main challenges in dilepton analysis: The small decay probability. Because of this, high statistics, in the order of billions of events, are necessary to measure a sufficient number of dileptons for a detailed analysis.

Nonetheless, once adequate statistics are achieved, the dilepton signal gives direct insights into the spectral function of the vector mesons in the hot and dense medium. The  $\rho$  meson, with the smallest lifetime of 1.32 fm/c serves as a particularly interesting probe. With a lifetime of the fireball  $\tau$  of about  $\tau \leq 15$  fm/c [22], the  $\rho$  meson is most likely to decay in the fireball itself, allowing for the investigation of medium modifications in the hottest and densest phase.

---

## 1.4.2 Dilepton Emission

The dilepton emission rate of a thermalised source per unit four-volume  $d^4x$  and four-momentum  $d^4q$  is given by [19]:

$$\frac{dN}{d^4x d^4q} = -\frac{\alpha_{em}^2}{M^2 \pi^3} f_B(q_0 : T) \frac{L(M)}{M^2} Im\Pi_{em}^\mu(M, q; T, \mu_B) \quad (1.11)$$

where  $f_B(q_0 : T)$  is the thermal Bose function,  $Im\Pi_{em}^\mu$  is the electromagnetic spectral function, and  $M = M_{ee}$  is the invariant mass of the dilepton pair. Regions of invariant masses with  $M \leq 1\text{GeV}/c^2$  are typically classified as low mass regions (LMR). Here, as discussed in section 1.4.1, the  $\rho$ ,  $\omega$  and  $\phi$  meson are the dominating dilepton sources in the fireball. This translates to a saturation of the spectral function  $Im\Pi_{em}^\mu$  by the light vector mesons and allows a description of the interactions of photons with hadronic matter via the Vector Meson Dominance Model [23].

Equation 1.11 demonstrates how measurements of dileptons generally allow insights into the thermal properties of the medium in terms of the temperature  $T$  and baryochemical potential  $\mu_b$ . One can also realise that dileptons carry unique information through their invariant mass  $M$ . Due to the mass dependence found in equation 1.11, it can be understood that the reconstructed invariant mass spectrum entails the sought-after information about thermal properties.

On its basis, some of the unique insights available through the analysis of dileptons can be listed [24]:

- **Lifetime of the fireball:** The amount of thermal dileptons is known to depend on the volume  $V$  and the lifetime  $\tau$  of the fireball. If the volume is determined, for example via the number of charged particles, the measured dilepton yield can be traced back to a determination of  $\tau$ .
- **Chiral symmetry restoration:** As discussed in sections 1.1.2 and 1.2, the spectral functions of the  $\rho$  meson and its chiral partner  $a_1$  are expected to align themselves with the restoration of chiral symmetry at extreme conditions. Reconstruction of the dilepton thermal radiation provides one way to reconstruct these spectral functions experimentally and possibly observe the theoretically predicted effects.
- **Azimuthal anisotropy and flow parameters:** Dilepton analysis also allows access to the radial distribution of their emission [26, 25]. Since flow effects grow larger at later phases of the collision, such an investigation allows insights into the time evolution of the system.

---

## 1.5 Goal of this Analysis

---

This analysis is based on data recorded at the HADES experiment: Au+Au in April 2012 and Ag+Ag in March 2019, both at 1.23A GeV. For these collision systems, the dilepton signal is to be extracted and the excess dilepton radiation is to be isolated. This allows for a direct comparison of the system size dependence on the thermal dilepton radiation. In addition, the analysis of each collision system is to be performed at varying centralities, thereby allowing an investigation into the centrality dependence.

The two key observables to be determined are the excess yield and the temperature of the fireball. For this purpose the invariant mass spectra are to be reconstructed. While this has been started for central Au+Au collisions in existing studies [27], the investigation of the HADES Ag+Ag data will need to be done from the ground up.

---

## 2 HADES

---

The High-Acceptance-Di-electron-Spectrometer (HADES) [28] at the GSI Helmholtzzentrum für Schwerionenforschung in Darmstadt, Germany, is a fixed target experiment optimised for the analysis of high multiplicity heavy-ion collisions. The beam is supplied by the adjoining SIS-18 accelerator, providing energies of around 1-3.5A GeV depending on the ion species. The HADES is divided into 6 detector segments, also called sectors, which are fitted in a ring structure behind the target. This leads to a large geometrical acceptance, covering a polar angle from  $18^\circ$ - $85^\circ$ [28] and an azimuthal angle of almost  $360^\circ$ [28]. With the additional high trigger rate capabilities, namely 8 kHz for the Au+Au experiment in 2012 [29] and 30 kHz for the Ag+Ag experiment in 2019 [30], the HADES allows detection and analysis of the rare dilepton pairs. By virtue of upgraded detector systems, three days of Ag+Ag beam time allowed the detection of a comparable amount of dilepton signal as during the four weeks campaign of Au+Au measurements.

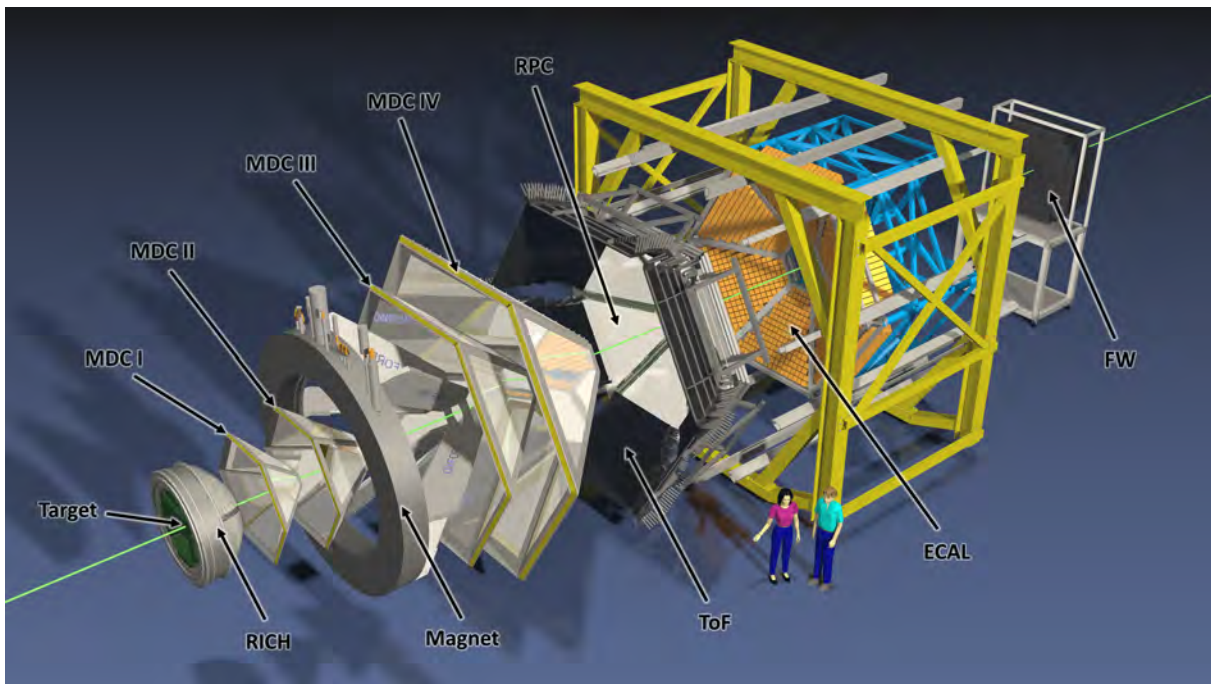


Figure 2.1: Schematic Layout of the HADES experiment. Figure taken from [31].

---

### 2.1 START Detector and Target

---

The START detector is located within the beam line in front of the target. Here, a signal is generated for every beam particle flying through the target. This, in turn, gives rise to a starting time which can later be used

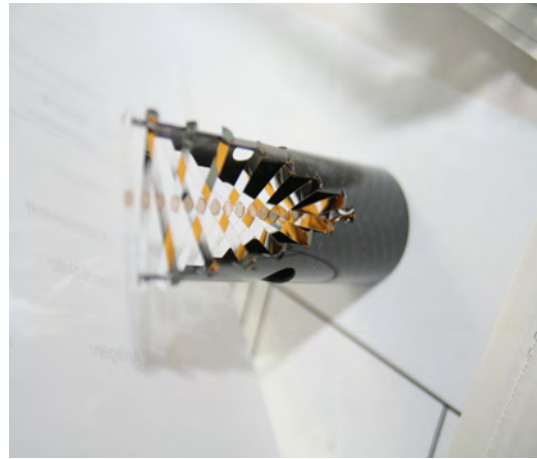
---

for time-of-flight and velocity calculations. The START detector also provides the opportunity to monitor the incoming beam, in order to improve alignment and focus.

The target itself is designed to reduce  $e^+e^-$  background from photon conversion pairs. For this purpose, it is segmented into several thin pallets, separated by a given distance and rotated to each other. This way, photons from the collision do not need to travel through the remaining target material but have a good chance to pass the upcoming foils without any further interaction. For the Au+Au experiment in 2012, the target consisted out of 15 pallets of  $25\ \mu\text{m}$  thickness, 2.2 mm diameter and gaps between the pallets of 3 mm. For the Ag+Ag experiment in 2019, a similar structure is utilised. The only exception is a larger pallet thickness of  $40\ \mu\text{m}$  due to the smaller atomic number, and thereby larger interaction length, of silver. In the end, the chosen target geometry limits the average photon conversion probability to below 1% [29].



(a) Gold target.



(b) Silver target.

Figure 2.2: Photos of gold (left panel) and silver (right panel) targets segmented into 15 target foils in order to avoid photon conversion pairs.

---

## 2.2 Ring Imaging Cherenkov Detector

---

Particles produced in the reaction will continue to fly towards the detector systems. On their way, they pass through the Ring Imaging Cherenkov detector (RICH) which is dedicated solely to the identification of  $e^\pm$  tracks. It works on the basis of Cherenkov radiation and by exploiting the fact that electrons and positrons are the lightest charged particles coming from the collision. More precisely, the RICH detector consists out of gas chamber and a reflective mirror at its edge. If the chamber is filled with a gas of suitable refractive index  $n$ , the light electrons and positrons from the collision move faster than the speed of light, leading to the emission of Cherenkov radiation. This radiation is then reflected on the mirrors and detected using photon detectors. Since no other particles are light-weight enough to produce Cherenkov radiation, this allows for the identification of  $e^\pm$ .

In the Au+Au experiment in 2012, the chamber was filled with perfluorobutane ( $C_4F_{10}$ ). Since then, the RICH detector has been upgraded with a new photo tube based photon detector and electronic read out chain. In addition, the perfluorobutane has been replaced by isobutane ( $C_4H_{10}$ ). These changes allow for an enhancement in the detectable photon yield.

---

## 2.3 Multiwire Drift Chamber and Magnet

---

The central system for reconstruction of the tracks and momenta of all particles are the Multiwire Drift Chambers (MDC) in combination with a superconducting toroidal magnet.

A single MDC consists out of multiple parallel wires, which are set up in several gas filled chambers. When a charged particle traverses such a chamber, it leaves a trail of ionised gas atoms, leading to a signal at an adjacent anode wire. By overlaying several cells, each at an angle to one another, the exact position of the travelling particle can be estimated with accuracies of less than a millimeter [32]. Furthermore, two MDC cell layers are placed in sequence to reconstruct the trajectory of a particle. This entails the comparison between the signal of the first and second MDC layers to estimate the most probable path.

In addition to the MDCs, a magnet is employed to determine the momentum of charged particles. At HADES, two MDCs are placed in front of, and two MDCs are placed behind the magnet. In that way, the track is reconstructed before and after the particle passed through the magnetic field. The measured change of the trajectory gives information about how far the particle was bend. With the knowledge of the particles charge  $q$  and the magnetic field strength  $B$ , the momentum can be determined. At HADES, Runge–Kutta methods are employed for this reconstruction.

---

## 2.4 Multiplicity Electron Trigger Array

---

After a particle went through the RICH detector and the tracking system, it will hit a further set of detectors known as the Multiplicity Electron Trigger Array (META). This array is split into two systems depending on the polar angle: The time-of-flight (TOF) detector at polar angles of about  $\Theta \geq 45^\circ$ , or the Resistive Plate Chambers (RPC) at polar angles of  $\Theta \leq 45^\circ$ . The former is referred to as system 1 and the latter as system 0.

Both the TOF detector as well as the RPC are used for the purpose of time-of-flight measurements. As the distance between the START detector and the META is known, this also allows to reconstruct a particles velocity. The main difference between the two detector systems lies in the technology used for this purpose. On the one hand, the Resistive Plate Chambers are capable in handling high multiplicities, which is why they are located at smaller polar angles. On the other hand, the TOF detector is based scintillator technology. Here, the incoming particles produce light, which is picked up by photomultiplier tubes. This allows to estimate the energy loss  $dE/dx_{TOF}$  in the TOF detector, but it limits the number of detectable particles per scintillator strip to one. Consequently, it is only applicable for reliant usage at larger polar angles. In this area, however, the additional information about the energy loss can be used to improve the particle identification.

---

## 2.5 Electromagnetic Calorimeter

---

In 2018, HADES has been upgraded with an electromagnetic calorimeter (ECAL) [33] which serves as a final detector layer at polar angles of  $12^\circ$  to  $45^\circ$ [34] and with almost full azimuthal coverage. It consists out of 978 lead glass elements [34], each of which are connected to a photomultiplier tube. When electromagnetic probes traverse through the lead medium, they deposit energy. In case of photons, the main interaction process is via pair production. In case of electrons or positrons, Bremsstrahlung is emitted. Either way, new photons and

---

dilepton pairs are created. These new particles, in turn, interact with the surrounding material in the same way, leading to the overall generation of an electromagnetic shower.

In order to measure the extent of this shower, the Cherenkov effect is exploited. With a refraction index of  $n = 1.708$  [34] in lead, the newly produced electrons and positrons will travel through the medium faster than light. This generates Cherenkov radiation, which is measured at the adjacent photomultiplier tubes. In the end, provided that the module is long enough for the whole energy of the initial particle to be transferred into the medium, the number of detected Cherenkov photons  $N_\gamma$  allows for the determination of the incoming particles energy. For this purpose,  $N_\gamma$  can be assumed to be approximately proportional to the deposited energy [34].

With the addition of the ECAL detector system, the possibility to directly detect photons and to determine their energy is introduced. Therefore, additional decay channels, for example  $\pi^0 \rightarrow \gamma\gamma$  and  $\eta \rightarrow \gamma\gamma$ , have become accessible.

---

## 2.6 Data Summary Tape

---

At HADES, the raw detector signals, measured during a collision experiment, are saved in Hades List Data (HLD) files. These files entail information about the times, locations and magnitudes of signals made by all detector parts. In a first step, this raw data needs to be translated into a format suitable for physics analysis. This is a multi-step process [29]. First, the raw data is unpacked. Then, values from arbitrary detector units are calibrated into consistent physical quantities. Finally, using the detector systems described above, a hit and track reconstruction is performed. The results are saved in a data summary tape (DST).

In the end, the separate events are identified. For every event, a list of potential particle candidates is found, and for each candidate the physical properties, e.g. momentum or electric charge, are determined. As such, DST files are structured in a tree format and consists of hierarchically ordered classes.

Since this transformation of raw data into a DST is necessary for virtually all physics analysis, it is usually done centrally and only repeated when software updates or other newly incorporated information are expected to lead to improvements in the reconstruction process.

---

## 3 Analysis of Ag+Ag Data

---

The reconstruction of the  $e^+e^-$  invariant mass, transverse or rapidity spectra can generally be divided into several steps as illustrated in figure 3.1. They are common to both the Ag+Ag and Au+Au analysis performed in this thesis and shall be discussed in detail in the following sections.

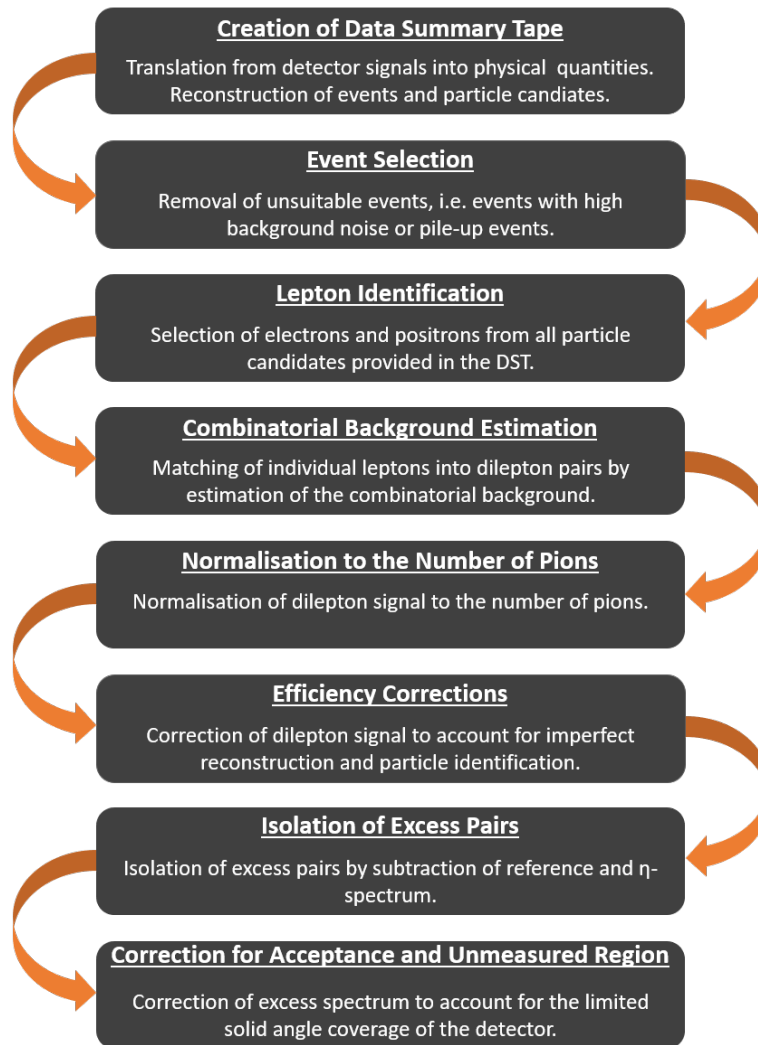


Figure 3.1: Schematic overview of analysis steps needed for the reconstruction of the invariant mass spectra.

---

## 3.1 Event Selection

---

The foundation of this analysis is the data summary tape (DST), see section 2.6, which entails information about all measured events and the particles therein. Although sophisticated algorithms are utilised to ensure a high accuracy in this transformation from raw detector signals to DST, it is important to emphasise that the reconstructed tracks and properties can, by the very nature of the experiment, only ever serve as best guesses of how particles really travelled through the detector. It is likely that some events and tracks have been identified and matched incorrectly.

Starting with the event identification, one can imagine a scenario where two events occur in such short succession that they are not registered as separate, a phenomenon referred to as pile-up events. Similarly, some registered events might come from collisions outside the target region. Furthermore, background and statistical noise could lead to unreliable measurements, for example in the timing of the event.

For these reasons, the first steps for a precise dilepton analysis is the selection of suitable events and lepton candidates where uncertainties and mismatches are very unlikely.

In this analysis, the following conditions are used to filter out unsuitable events:

- **goodStart:** Removes events that do not have a well defined start time.
- **noPileUpStart:** Removes events if a second cluster has been detected by the START detector, in order to prevent pile up events.
- **NoVeto:** Removes nuclei that signaled in START detector but did not collide with target.
- **goodSTARTVETO:** Removes events in which an additional START hit occurred within 15-350 ns for which there is no correlated VETO hit in the windows  $\pm 2$  ns.
- **goodSTARTMETA:** Removes events in which an additional START hit occurred after 80-350 ns which is also correlated to META hits.
- **goodVertex:** Removes collision events that are not Ag+Ag, e.g. collisions of beam nuclei with surrounding material, by reconstruction of reaction vertices.

They will be summarised as the condition **isGoodEvent**.

An additional requirement is further established for the number of active sectors. During an experiment, some hardware components of the detector might fail temporarily. This will translate to some sectors not recording or not properly recording events. In order to secure a consistent acceptance, all events, where not all six sectors were active, are removed from this analysis. This shall be referred to as the **isGoodSector** selection.

### 3.1.1 Centrality Selection

A major focus of this analysis is the centrality dependence of the measured thermal radiation. As discussed in section 1.3, a direct measurement of the centrality and impact parameter is not possible. Instead, the measured charged particle multiplicity  $N_{TOF+RPC}$  from the META detectors is used to estimate the underlying number of participating nucleons  $\langle A_{part} \rangle$ . Details of this procedure are discussed in section 1.3.1. The resulting definitions of the Ag+Ag centrality classes are summarised in table 3.1:

Centrality Classes	$\langle A_{part} \rangle$	$N_{TOF+RPC}$
0-10%	168	91 - 154
10-20%	103	69 - 90
20-30%	76	50 - 68
30-40%	53	34 - 49
0-40%	102	34 - 154

Table 3.1: Centrality class definitions based on the number of measured hits  $N_{TOF+RPC}$  for Ag+Ag collisions at  $\sqrt{s_{NN}} = 2.42$  GeV.

Based on these multiplicities  $N_{TOF+RPC}$ , a final event selection is made to only include 0-40% centrality events, referred to as **isCentral** selection. Using 10% centrality bins, this still allows the investigation of centrality dependence, but avoids problems of more peripheral events, namely smaller statistics and the rising probability of Ag+C contamination from beam collisions with detector material.

In the end, from around  $8.1 \cdot 10^8$  initial events recorded during the beam time,  $5.8 \cdot 10^8$  events remain for this analysis.

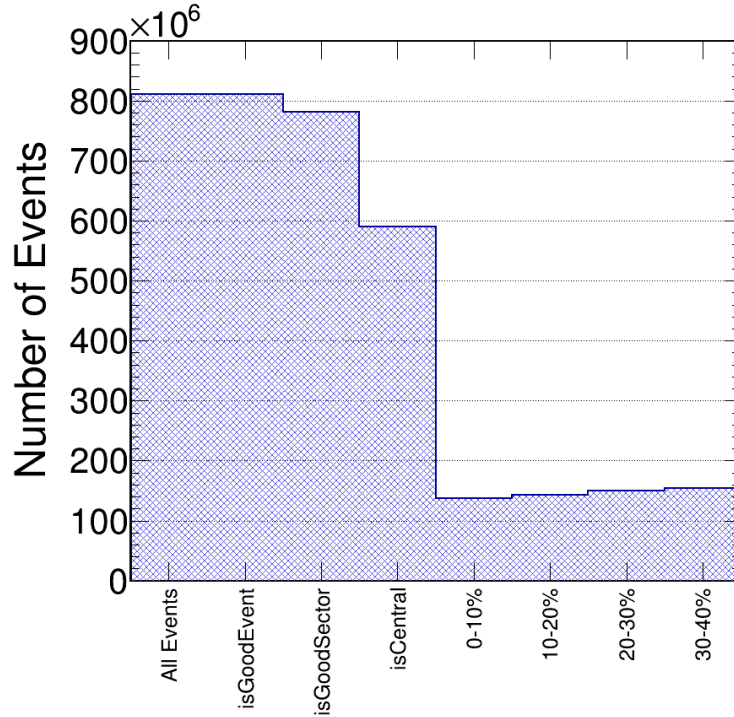


Figure 3.2: Number of events in dependence of event selection criteria for Ag+Ag collisions at  $\sqrt{s_{NN}} = 2.42$  GeV. After the **isCentral** requirement, the events are distributed roughly equally over the 10% centrality bins.

---

## 3.2 Lepton Identification

---

Leptons from the hot and dense fireball are rare probes and require sufficient statistics to allow for a meaningful analysis. Since the number of recorded events is limited, it is important to achieve a high probability for a single lepton to be detected and to be properly distinguished from other particles. At the same time, false classifications lead to an increased background which is also to be avoided. With these two opposing objectives in mind, the lepton selection criteria for this work have been selected.

The starting point is again the DST, which provides a list of possible particle candidates for a given event. Further, every one of these particle candidates is assigned the most likely track candidate and corresponding detector hits. However, false matches and wrong combinations, e.g. of track segments before and after the magnet, are possible and need to be taken into account. The main tool for this task is a track sorting algorithm. In such an algorithm, one can first define a number of minimum track requirements. Then, every track, which fulfils these conditions, is compared to all the other tracks. If two or more tracks share the same detector hit, they are sorted based on a quality parameter, namely the Runge-Kutta quality  $\chi_{RK}^2$ . Based on this sorting, only the track with the smallest  $\chi_{RK}^2$  is taken into the final particle pool of the analysis since it is the most likely scenario of what really happened.

The minimum quality requirements in this analysis are:

- Velocity  $\beta > 0.9$ .
- Momentum  $p$  between  $100 \text{ MeV}/c < p < 2000 \text{ MeV}/c$ .
- $\chi_{RK}^2 < 1000$ .
- Track has a fitted inner and outer track segment, as well as a matching META detector hit.
- Track has a matching RICH ring, allowing a maximum deviation from MDC track to RICH ring of  $8^\circ$ .

The remaining pool of tracks is then suitable for further analysis. The momentum and velocity requirements also act as a first loose electron and positron cut. In the following, the further selection criteria for adequately differentiating leptons from other particles are introduced.

### 3.2.1 Relativistic Mass Cut

The main property used for electron and positron identification is their low mass relative to hadrons. At SIS-18 energies, the outgoing leptons will have relativistic speeds and their effective mass  $m$  can be calculated via the measured velocity  $\beta$  and momentum  $p$ :

$$m^2 = p^2 \frac{1 - \beta^2}{\beta^2 c^2} \quad (3.1)$$

In order to find typical relativistic masses of electrons and positrons, all particle candidates are divided into several momentum bins of around  $100 \text{ MeV}/c$  in size. For every momentum bin, the effective mass distribution is plotted. This reveals an electron peak, while background sources, namely pion contamination, are mostly outside the peak region. On this basis, a relativistic mass cut is introduced which removes all particle candidates not within 4 sigma of the mean electron mass  $m_e$ . This exercise is repeated for both META

systems in order to gain even better purity. The resulting (momentum dependent) maximum effective mass is shown in figure 3.3:

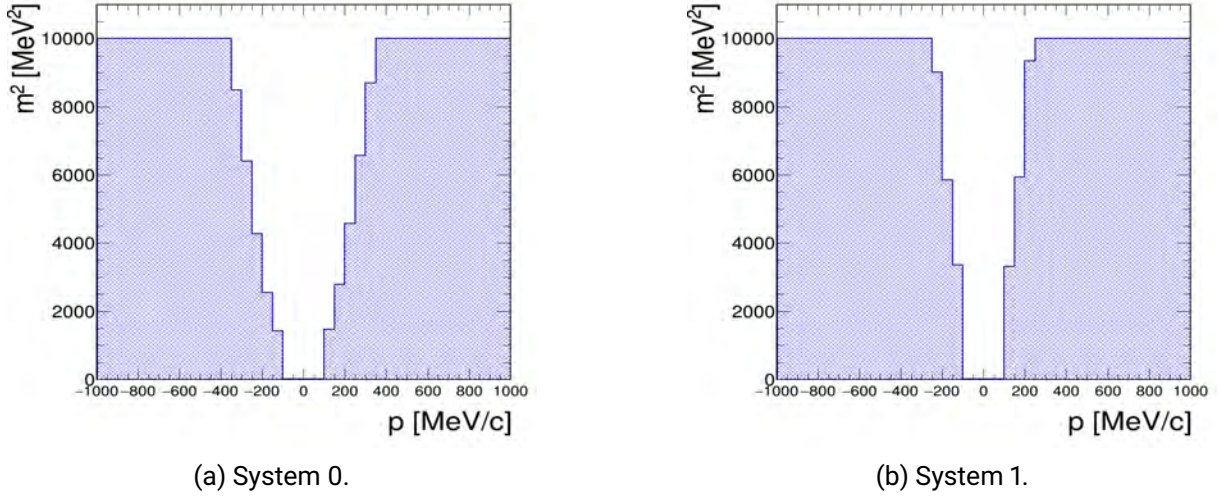


Figure 3.3: Momentum dependent lepton mass cut. All particles outside the filled area are removed from the dilepton analysis.

### 3.2.2 Spatial Correlation between RICH Ring Center and MDC Track

The HADES includes some dedicated detector components for the identification of leptons. Their information, especially from the RICH detector, are another cornerstone utilised in this analysis. A first straightforward condition for every lepton candidate can easily be articulated: A RICH signal must be matched with the particles track. However, in practice, the challenge lies in determining how strict the ring matching needs to be in order to recognise the majority of electrons and positrons correctly, but also to reliably remove random matches with hadrons, whose tracks coincidentally lie close to a RICH ring.

To quantify how well a ring matches with the rest of the track, a ring matching quality  $richQa$  is calculated. If  $\Delta\Phi = \sin\Theta \cdot |\Phi_{RICH} - \Phi_{MDC}|$  and  $\Delta\Theta = |\Theta_{RICH} - \Theta_{MDC}|$  are the azimuthal and polar angle differences of MDC to RICH track,  $richQa$  can be defined as follows:

$$richQa = \sqrt{\Delta\Phi^2 + \Delta\Theta^2} \quad (3.2)$$

On this basis, one can introduce a RICH matching quality cut, rejecting all particle candidates which are above a set threshold  $richQa \geq richQa^{cut}$ .

In order to find suitable values of such a threshold, the distributions of  $\Delta\Phi$  and  $\Delta\Theta$  have been calculated in dependence of the polar angle  $\Theta$  and for every individual sector. This is demonstrated in figure 3.4 for simulated and measured leptons in sector 0.

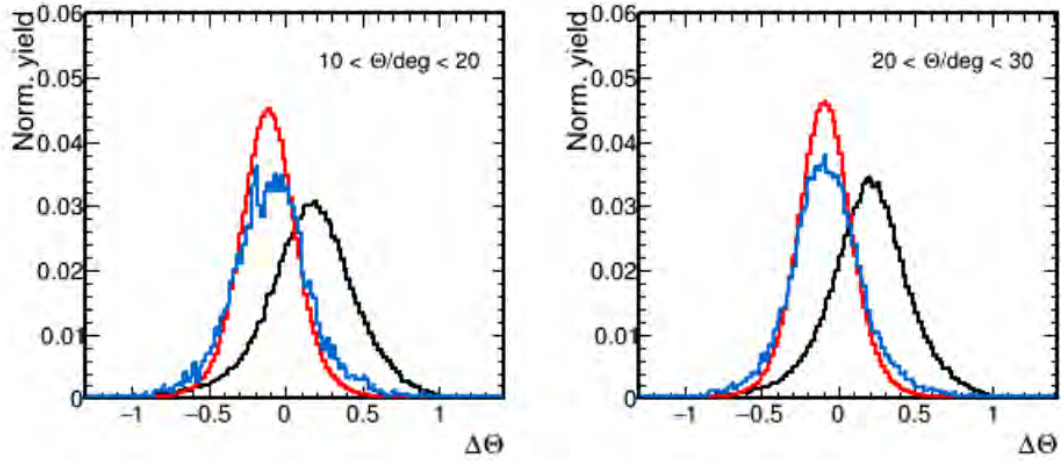


Figure 3.4: Lepton distribution in sector 0 over  $\Delta\Theta$  for Ag+Ag collisions at  $\sqrt{s_{NN}} = 2.42$  GeV. The black line represents leptons from experimental data. The red line represents simulated white leptons. The blue line represents leptons simulated in UrQMD events. Figure taken from [35].

Here, one can identify the distributions to follow roughly a Gaussian shape. However, a noticeable shift of the mean from the center  $\Delta\Theta = 0$  is noticeable for the experimental data. This effect needs to be taken into account when defining the *richQa* thresholds. Otherwise, the cut is not symmetric and a major deviation of experimental data to simulated events is not regarded.

Therefore, the matching quality can be based on the maximum allowed standard deviations  $\sigma$  from the mean. With the distributions as shown in figure 3.4, the mean and  $\sigma$  have been determined in dependence of the polar angle  $\Theta$ . Similarly, analogous investigations have been made in dependence of the momentum  $p$  [35]. In this latter case, no significant change of  $\Delta\Phi$  or  $\Delta\Theta$  with the momentum was found, such that the final cut is chosen to be momentum independent.

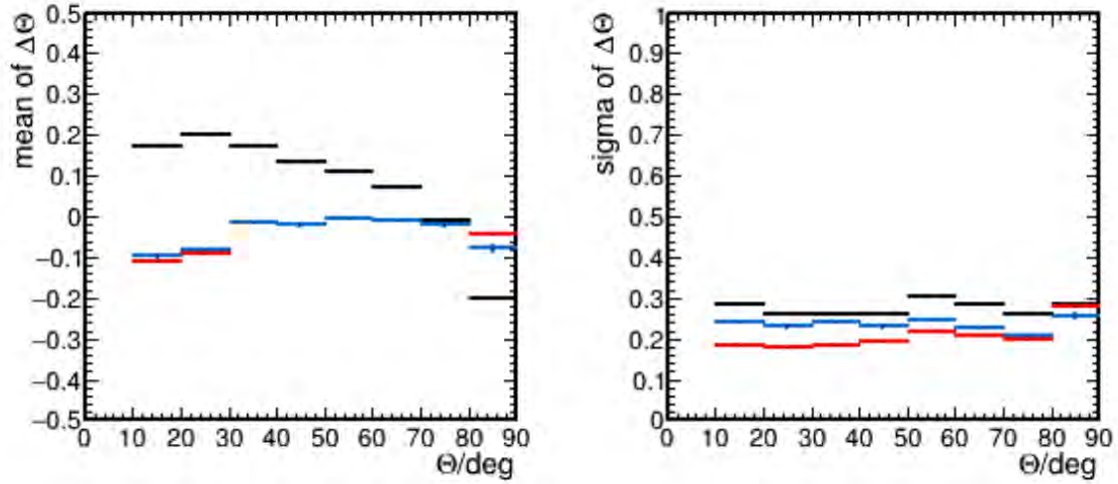


Figure 3.5: Mean and standard deviation of  $\Delta\Theta$  distributions over  $\Theta$  in sector 0 for Ag+Ag collisions at  $\sqrt{s_{NN}} = 2.42$  GeV. Black lines represents leptons from experimental data. Red lines represents simulated white leptons. Blue lines represents leptons simulated in UrQMD events. Figure taken from [35].

In this analysis, a  $2\sigma$  cut is applied, such that over 95% of leptons are kept in the sample. The resulting lepton pool can be seen in figure 3.6.

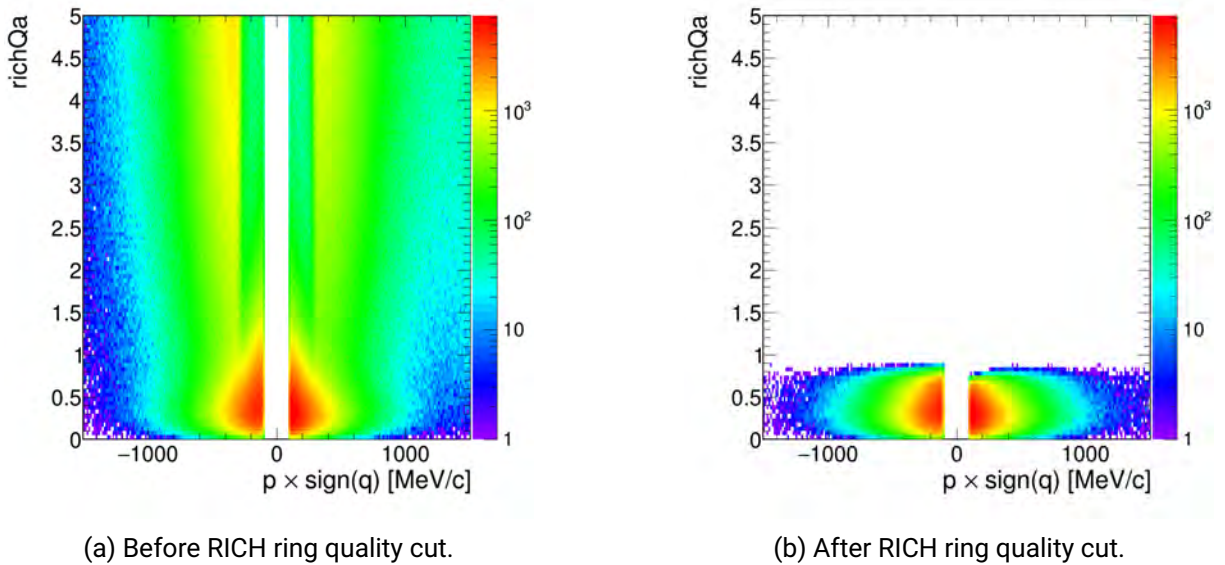


Figure 3.6: Number of particle candidates over RICH matching quality and momentum before and after RICH ring quality cut for Ag+Ag collisions, 0-40% centrality, at  $\sqrt{s_{NN}} = 2.42$  GeV. Filled with particle candidates from system 0, sector 0.

### 3.2.3 Conversion and Opening Angle Cut

The RICH matching quality and mass cut provide the necessary tools to separate electrons and positrons from pions and other hadronic particles. However, not all detected leptons are a direct product of the collision. There are also photons which interact with the detector material, creating  $e^+e^-$  pairs via pair production, but without offering any sizeable information about the heavy and dense collision phases. These conversion pairs are characterised by small opening angles relative to the dileptons created in the collision [36], something that is exploited in some additional cuts aiming to remove unnecessary background.

First, a region of 9 degrees around any RICH ring must not hold another signal. If any two leptons have an opening angle below this 9 degree threshold, they are removed from the sample. In previous analysis, this cut has been made using the track information from MDC. For Ag+Ag, it has been realised that the RICH angle determination is more precise and, therefore, provides more accurate results in this close pair rejection.

Second, it is possible that two RICH rings are so close to each other, that they can no longer be properly distinguished from one another. In this case, only one RICH track would be reconstructed and a simple 9 degree cut based on separate rings is insufficient. The only feasible way to detect such a scenario is counting the number of Cherenkov photons detected. For two leptons, sharing one RICH track, the number of detected photons is likely to be higher than for tracks made by only one. In this analysis, a particle candidate with more than 25 hits in the RICH photon detectors is removed from the sample.

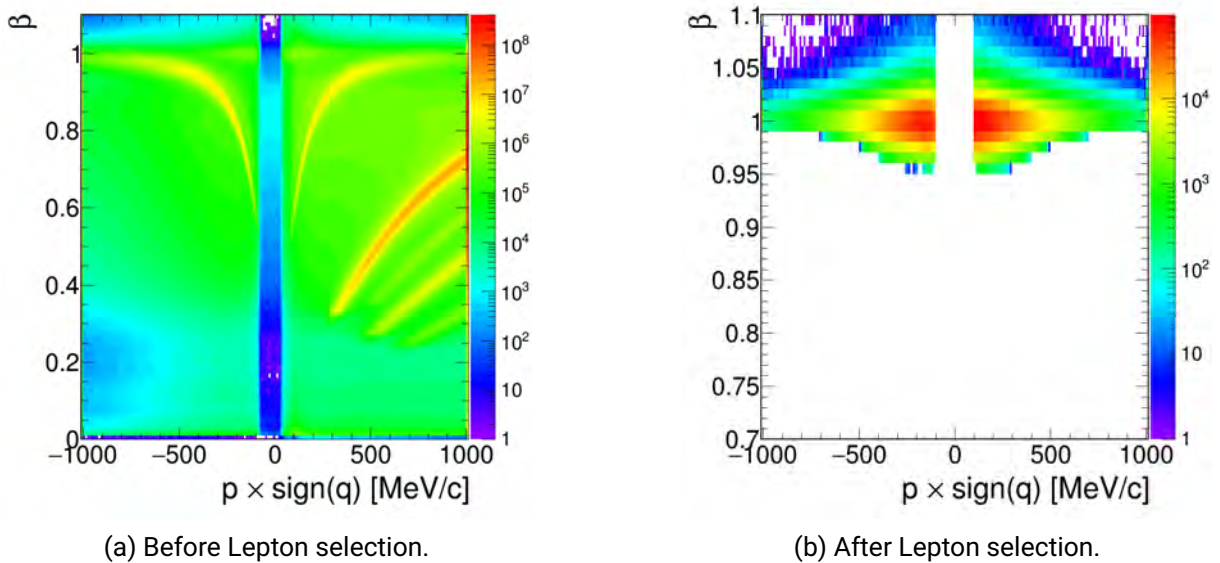


Figure 3.7: Number of particles over charge momentum and velocity before and after lepton selection for Ag+Ag collisions, 0-40% centrality, at  $\sqrt{s_{NN}} = 2.42$  GeV. Filled with particle candidates from system 0.

## 3.3 Estimation of Combinatorial Background

After individual electrons and positrons have been identified, they need to be paired up with their corresponding antiparticle. For this purpose, an invariant mass spectrum  $\frac{dN_{+-}}{dM}$  is first filled with all possible  $e^+e^-$

combinations. Then, a combinatorial background (CB)  $\frac{dN_{CB}}{dM}$ , which represents the amount of falsely matched pairs, is subtracted to calculate the actual signal [37]:

$$\frac{dN_{Signal}}{dM} = \frac{dN_{+-}}{dM} - \frac{dN_{CB}}{dM} \quad (3.3)$$

The challenge is thereby shifted from identification of actual pairs to the identification of the false combinations. In this analysis, the main method to estimate the CB is the same-event like sign method. Let  $\frac{dN_{++}}{dM}$  and  $\frac{dN_{--}}{dM}$  be the invariant mass spectra of all possible positron and electron pairs respectively, then the background is given by the geometrical mean of same-event like-sign pairs:

$$\frac{dN_{CBSE}}{dM} = 2\sqrt{\frac{dN_{++}}{dM} \cdot \frac{dN_{--}}{dM}} \quad (3.4)$$

For this equation to be valid, perfect charge symmetry is assumed. That means, positrons and electrons are equally likely to be detected and reconstructed. In practice, this symmetry is known to be violated since efficiencies for electron reconstruction are slightly higher than for positrons, see section 3.4. As a consequence, a charge asymmetry correction factor  $k$  needs to be included in equation 3.4. Furthermore, the same-event like sign method leads to large uncertainties if the amount of measured particles in an event is low. This is the case for the higher invariant mass regions where fewer dileptons are produced, possibly having a negative impact on the confidence of any findings made.

Both issues can be addressed with event-mixing methods. Here, a pool of similar events is considered simultaneously, and leptons from different events can be paired up to fill mixed invariant mass spectra  $\frac{dN_{+-}^{mix}}{dM}$ ,  $\frac{dN_{++}^{mix}}{dM}$  and  $\frac{dN_{--}^{mix}}{dM}$ . On the one hand, this will fail to describe any correlations that leptons might have within one event. An example of this is the decay of  $\pi^0 \rightarrow \gamma e^+ e^-$ , where the photon might convert into an additional  $e^+ e^-$  pair by interaction with the target material, resulting in correlations between the dilepton pairs. However, on the other hand, event-mixing does allow for virtually unlimited statistics. In this analysis, events have been mixed based on three conditions:

- **Centrality:** Only events of the same 10% centrality bin are mixed.
- **Reaction Vertex:** The vertex position of an event describes the location of where the collision took place in the target. Only events within 4 mm are mixed.
- **Event Plane Angle:** The event plane is defined by the beam axis and impact parameter vector. Only events with a maximum difference in event plane angle of  $15^\circ$  are mixed.

Based on the resulting spectra, a first addition to the same-event like sign is made by estimating a charge asymmetry factor  $k$ :

$$k = \frac{\frac{dN_{+-}^{mix}}{dM}}{\sqrt{\frac{dN_{++}^{mix}}{dM} \cdot \frac{dN_{--}^{mix}}{dM}}} \quad (3.5)$$

Furthermore, a comparison of shapes between  $\frac{dN_{+-}^{mix}}{dM}$  and  $\frac{dN_{CBSE}}{dM}$ , plotted in the right panel of figure 3.8, reveals that the mixed-event method is suitable to describe the background for invariant masses beyond around

0.3 GeV/c<sup>2</sup>. Only below this point are significant deviations due to correlations visible. At higher invariant masses of above 0.7 GeV/c<sup>2</sup> statistical fluctuations, due to limited statistics in the same-event background, become noticeable. In addition, the introduced factor  $k$  (see figure 3.8, left panel) has a peak of about 1.05 at  $M_{ee} \approx 0.15$  GeV/c<sup>2</sup>, but afterwards converges to one with increasing invariant mass  $M_{ee}$ .

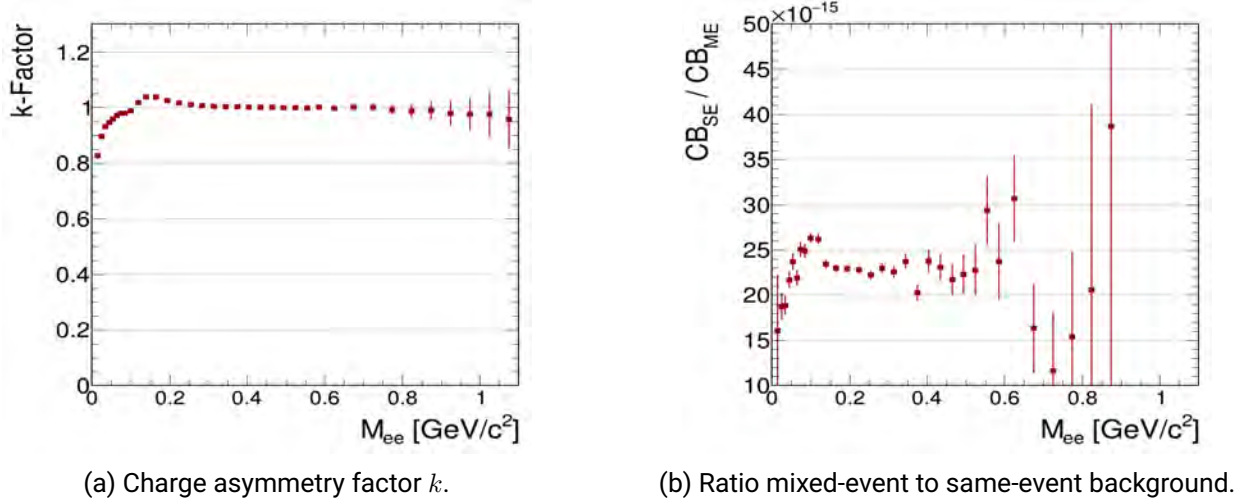


Figure 3.8: Charge asymmetry factor  $k$  (left panel) and ratio of mixed-event to same-event combinatorial background (right panel) in dependence of invariant mass  $M_{ee}$  for Ag+Ag collisions, 0-40% centrality, at  $\sqrt{s_{NN}} = 2.42$  GeV. Vertical lines represent statistical errors.

In the end, the advantages of both methods are combined. Up to  $M_{ee} = 0.4$  GeV/c<sup>2</sup> the background is described by the same-event method, corrected with the charge symmetry factor  $k$ . Afterwards, for  $M_{ee} \geq 0.4$  GeV/c<sup>2</sup> the normalised event-mixing spectrum  $\frac{dN_{+-}^{mix}}{dM}$  is employed. The region for normalisation is chosen to be at between  $M_{ee} = 0.3$  GeV/c<sup>2</sup> and  $M_{ee} = 0.4$  GeV/c<sup>2</sup>. In this way, the correlations at low masses are properly considered, while the uncertainties at high invariant masses, due to lower statistics, are kept small. The resulting background subtraction can be seen in figure 3.9 for Ag+Ag collisions at 0-40% centrality. Figure 3.10 further shows the achieved signal to background ratio  $S/B$  (left panel) and significance  $sgn = \frac{S}{\sqrt{S+B}}$  (right panel) as a function of invariant mass  $M_{ee}$ . In both cases, a maximum is identified in the  $\pi^0$  mass region of below  $M_{ee} \leq 0.15$  GeV/c<sup>2</sup>. The signal to background ratio then falls off two orders of magnitudes from 200 to around 1, with a minimum at  $M_{ee} \approx 0.2$  GeV/c<sup>2</sup>. The significance is found to decrease consistently with increasing invariant masses  $M_{ee}$ .

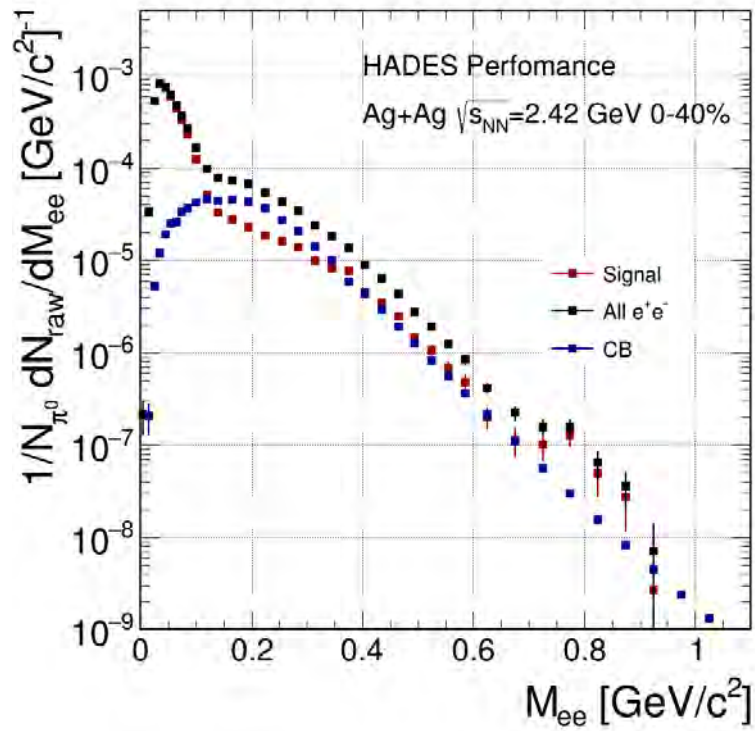
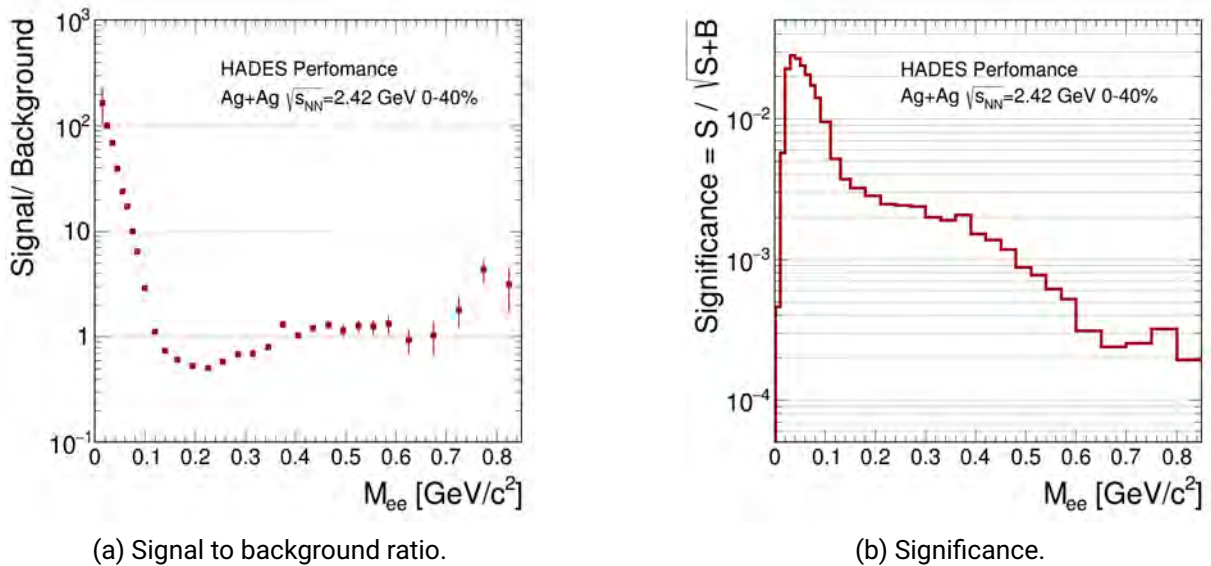


Figure 3.9: Example of combinatorial background subtraction and the resulting signal for Ag+Ag collisions, 0-40% centrality, at  $\sqrt{s_{NN}} = 2.42$  GeV. Vertical lines represent statistical uncertainties.



(a) Signal to background ratio.

(b) Significance.

Figure 3.10: Signal to background ratio (left panel) and significance (right panel) as a function of invariant mass for Ag+Ag collisions, 0-40% centrality, at  $\sqrt{s_{NN}} = 2.42$  GeV. Vertical lines in signal to background ratio represent statistical errors.

---

## 3.4 Acceptance and Efficiency Corrections

---

The signal extracted in the previous section does not yet provide a full reconstruction of all dileptons produced in the collisions. For one, the detector covers only a limited solid angle in space around the target. Particles flying outside this covered region will be missed. This is referred to as limited acceptance and needs to be corrected by the extrapolation of the signal to the unmeasured region. For another, even if a particle hits the detector region, the track reconstruction as well as lepton identification process is not perfect. Some valid electrons and positrons will not be found or falsely removed from the analysis, a circumstance which leads to imperfect efficiency.

Since the extent of the acceptance and efficiency loss is detector and analysis dependent, this renders a direct comparison of the measured raw signal with other experiments or theory meaningless. Instead, corrections need to be made to the experimental data, such that the resulting dilepton spectra reflect all virtual photons from the collision.

In general, the acceptance  $\epsilon_{Acc}$  is the ratio of leptons in acceptance  $N_{Acc}$  over the total number of leptons produced in the collision  $N_{Total}$ :

$$\epsilon_{Acc} = \frac{N_{Acc}}{N_{Total}} \quad (3.6)$$

Similarly, the efficiency  $\epsilon_{Eff}$  is defined as the ratio of reconstructed leptons  $N_{reco}$  over the leptons in acceptance:

$$\epsilon_{Eff} = \frac{N_{reco}}{N_{Acc}} \quad (3.7)$$

While conceptually easy to grasp, the challenge lies in finding ways to approximate the actual number of leptons while avoiding model dependencies as far as possible.

### 3.4.1 Single Lepton Efficiencies

In this analysis, the central tool to estimate acceptance and efficiency are simulations. In a first step, this is done on the level of individual electrons and positrons. Several millions of these single leptons are generated using the Pluto event generator [38], with homogeneous momentum (0-1 GeV/c), polar angle ( $0^\circ$ - $90^\circ$ ) and azimuthal angle ( $0^\circ$ - $360^\circ$ ). Based on their properties, i.e. momentum and angle, these leptons are then processed via a digitizer and the simulation package GEANT [39]. In GEANT (GEometry ANd Tracking), a detailed representation of all HADES detector materials and their digitizers is implemented, allowing for a realistic simulation of what detector signals the generated leptons would have produced. The end result are Hades List Data files, analogous to the results of real experiments.

Subsequently, these HLD files can then undergo the same procedure of track reconstruction and lepton identification as the real experimental data. Since the original number of generated leptons is known, this allows an estimation of the acceptance, based on the GEANT simulation, as well as the efficiency, based on the missing electrons after reconstruction from HLD.

In reality, a large influence on the achieved efficiency is the overall particle multiplicity from the collision. More particles lead to more possible combinations of matching tracks segments and detector hits, which in

turn, leads to higher likelihoods of falsely matched or entirely missed particle tracks. Therefore, it is not sufficient to only use single leptons as input for the efficiency corrections. There needs to be a background, simulating the full event and all its particles to allow for a reasonable estimation. This is done by embedding the generated  $e^+/e^-$  either to real data or to full events generated via UrQMD (Ultra relativistic Quantum Molecular Dynamics) [40]. The former is likely to give more accurate results, but the latter can be used for cross checks and has the advantage that the number of all input particles, as well as their properties, are known.

Altogether, almost  $3 \cdot 10^8$  single electrons and positrons are embedded into around  $2 \cdot 10^8$  UrQMD events and around  $2 \cdot 10^8$  real events. These events are then passed through the reconstruction and lepton identification methods discussed in previous chapters. On this basis, 3D histograms, counting the number of reconstructed electrons and positrons in dependence of  $p$ ,  $\theta$  and  $\phi$  are filled. With equation 3.6 and 3.7, this gives the single lepton efficiencies and acceptance according to the particles kinematics.

Figure 3.11 shows the results for electrons (left panel) and positrons (right panel) for Ag+Ag collisions at  $\sqrt{s_{NN}} = 2.42$  GeV and 0-40% centrality. Slight differences between embedding to real data vs embedding to UrQMD are visible. In addition, the efficiencies for electrons are slightly higher than for positrons. In both cases, a maximum efficiency is reached at  $p \approx 300$  MeV/c. In the region of higher momenta between  $1400 \text{ MeV/c} < p < 1800 \text{ MeV/c}$  the efficiency is found to be approximately constant at about 40%.

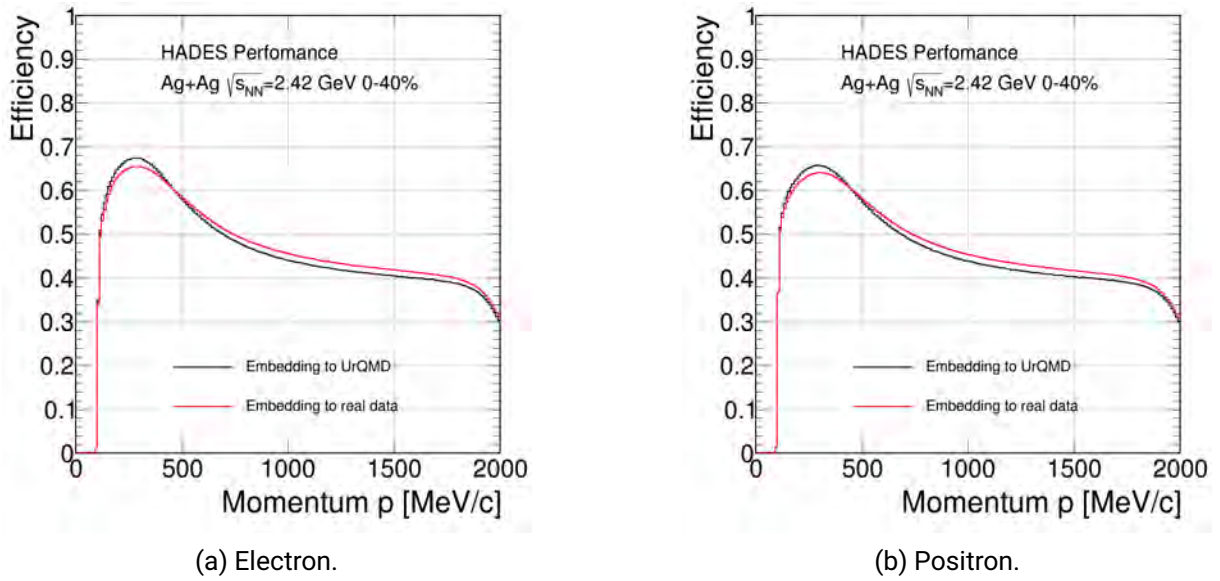


Figure 3.11: Single lepton efficiencies projected on the momentum for Ag+Ag collisions, 0-40% centrality, at  $\sqrt{s_{NN}} = 2.42$  GeV.

### 3.4.2 Momentum Smearing

In the above described procedure, the original kinematics, i.e.  $p$ ,  $\theta$  and  $\phi$ , are known and used in the filling of histograms. This is only appropriate, however, if the corrections are applied to leptons whose ideal kinematics are available. In real data, a small curvature in the magnetic field might lead to an substandard determination of the momentum  $p$ . With roughly equal probability, the reconstructed value might be shifted up or down from the truth. Further, especially for low momenta, leptons lose energy when transversing through the detector,

i.e. via Bremsstrahlung or interaction with the detector material. These effects lead to a so-called "momentum smearing" where the reconstructed momentum differs from the original, "true" momentum.

To account for this phenomenon, a first investigation can be made by comparing ideal vs reconstructed momentum in simulations. GEANT properly simulates the described effects. Figure 3.12 shows the resulting distributions.

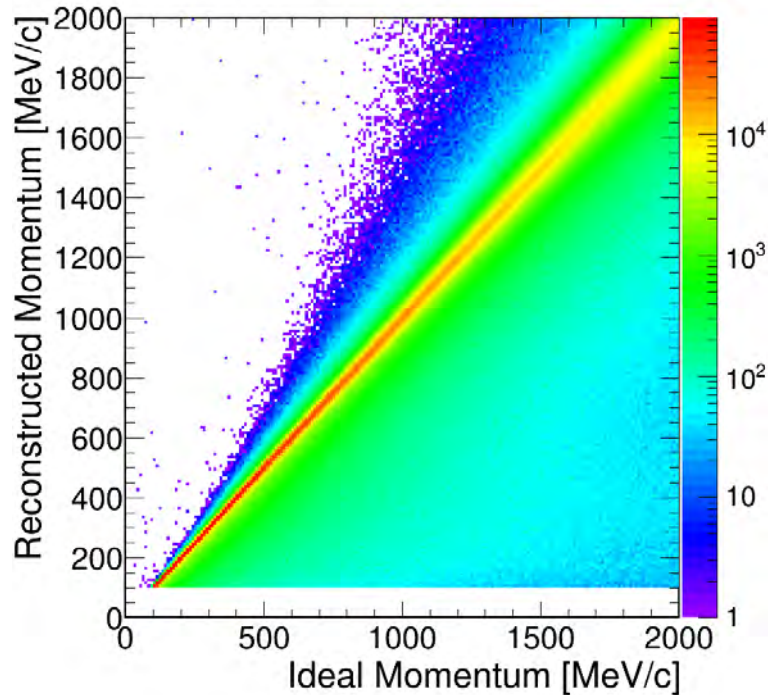
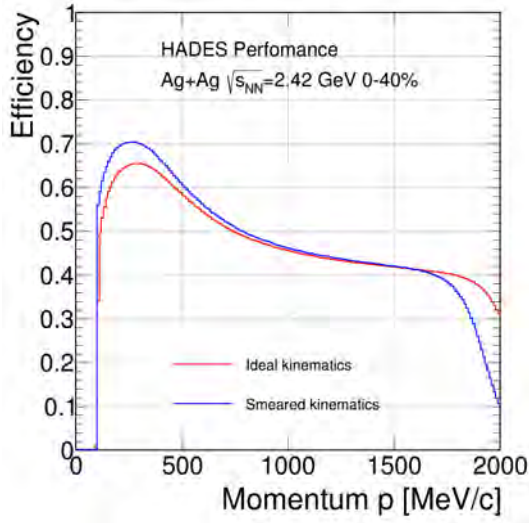
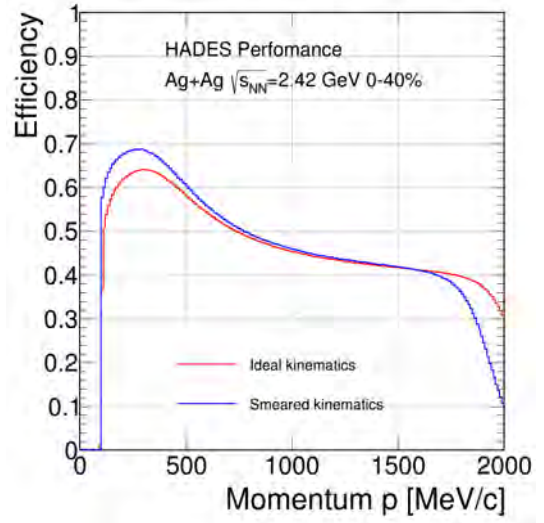


Figure 3.12: Distributions of ideal vs reconstructed momentum of electrons at  $0^\circ < \theta < 35^\circ$  for Ag+Ag collisions at  $\sqrt{s_{NN}} = 2.42$  GeV.

It can be noted that the majority of momenta are reliably reconstructed, as indicated by the red straight line. Yet, at the same time, a general momentum smearing is visible. In fact, for one ideal value of momentum, there is whole distribution of possible reconstructed momenta, and vice versa. This makes a direct correction for this effect impractical, if not unattainable. Still, it needs to be considered in the calculation of efficiency corrections. This can be done by filling the  $p$ ,  $\theta$  and  $\phi$  dependent 3D histograms, used for the calculation of the single lepton efficiencies, with the smeared kinematics of the particle. Figure 3.13 shows a comparison of single lepton efficiencies, projected on the momentum, when using ideal vs reconstructed values. As before, electron efficiencies are slightly higher than efficiencies for positrons. Other than that, the smeared kinematics lead to an increased efficiency at low momenta and a decreased efficiency for high momenta.



(a) Electron.



(b) Positron.

Figure 3.13: Single lepton efficiencies, calculated by embedding to real data, with and without smearing projected on the momentum for Ag+Ag collisions, 0-40% centrality, at  $\sqrt{s_{NN}} = 2.42$  GeV.

### 3.4.3 Pair Efficiency Corrections

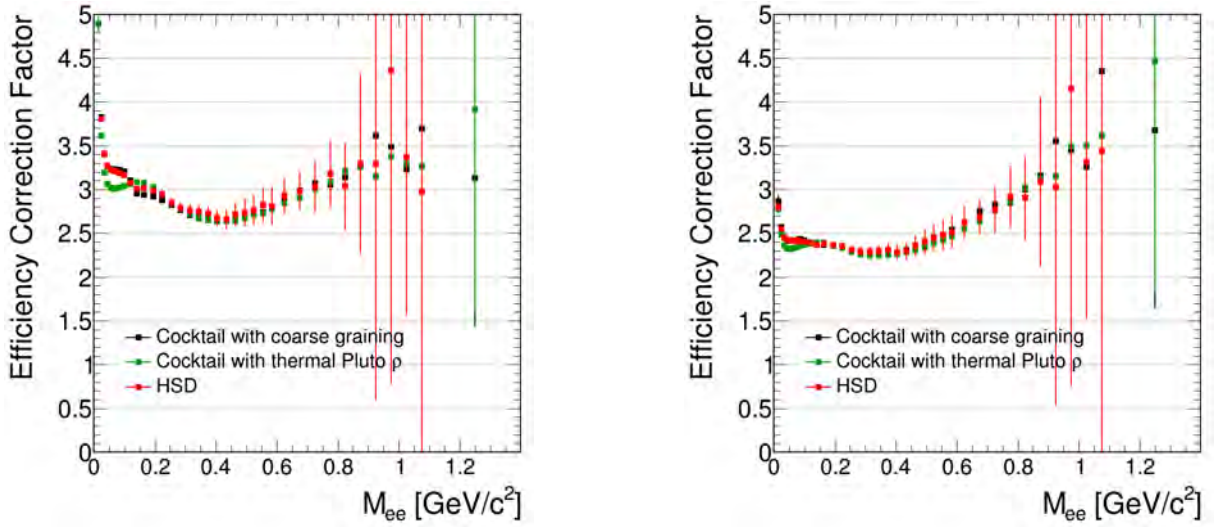
In the next stage, the corrections need to be extended from the single lepton level to the pair level for the invariant mass spectra. Arguably, the most straightforward approach would be to weigh each pair with its corresponding inverse efficiency while filling up the invariant mass histograms from the data. In this case, the combined efficiency for one pair can be estimated by the product of the individual parts  $\epsilon_1 \cdot \epsilon_2$ . Although this method has the great advantage that no further model dependencies are needed. It also comes with two major downsides. First, the combinatorial background calculation in equation 3.4 has been derived under the assumption of no further scaling factors, but only raw number of counts. A pair correction as described would violate this premise and a more sophisticated approach for the CB calculation would be required. Second, the number of reconstructed dileptons decreases exponentially for higher invariant masses. A direct, event-by-event correction in regions with only a few reconstructed pairs, would be prone to large statistical uncertainties.

On this basis, an altogether different approach has been chosen for this analysis. Instead of relying purely on experimental data, the lepton distribution of momentum  $p$  as well as of angles  $\theta$  and  $\phi$  is estimated using simulations. For this purpose, events of all essential dilepton sources ( $\pi^0$ ,  $\eta$ ,  $\omega$ ,  $\rho$ ,  $\phi$ ) are generated using Pluto. For each source, the invariant mass spectra are plotted. One with all pairs from the collision, describing the whole  $4\pi$  solid angle; one with all pairs in the acceptance as can be determined with the single lepton acceptances known from previous steps; and finally, one with all pairs in acceptance but additionally weighted with their respective efficiencies  $\epsilon_1 \cdot \epsilon_2$ . The ratio of the spectrum in acceptance over the spectrum scaled down for efficiency, gives then an efficiency pair correction factor  $\epsilon_{Pair}$  in dependence of the invariant mass  $M_{ee}$ .

A correction factor for the measured data will need to be based on a realistic cocktail, generated by properly mixing of the individual dilepton sources. The weight of each source can be estimated by the product of branching ratio and multiplicity per event as discussed in section 3.4.4 for the freeze-out cocktail.

In addition, the  $\rho$  meson contributes to the dilepton signal from the hottest and densest stage. Since it is a probe known to be produced and to decay within the fireball, a broadening of the spectral function is expected. The exact extent of this is one goal of the measurement, yet for the purpose of the efficiency correction, some predictions need to be made already in order to simulate a full cocktail. From previous analysis, coarse-graining models have been shown to yield reliable results [36]. As another option, the  $\rho \rightarrow e^+e^-$  can also be generated thermally. Finally, an alternative to generating the cocktail components individually, Hadron-String-Dynamics (HSD) [41] allow the simulation of the whole cocktail at once.

In the end, all three models are employed to generate a cocktail that includes all notable dilepton sources. In addition, efficiencies have been determined with ideal and smeared kinematics, as well as embedding to UrQMD and embedding to real data. First, the effect of the utilised kinematics can be see in figure 3.14.



(a) With ideal kinematics and embedding to real data. (b) With smeared kinematics and embedding to real data.

Figure 3.14: Pair efficiency factors in dependence of the invariant mass for Ag+Ag collisions, 0-40% centrality, at  $\sqrt{s_{NN}} = 2.42$  GeV. Vertical lines represent statistical uncertainties.

It can be noted how ideal kinematics lead to a greater correction factor than smeared kinematics. This can be understood from figure 3.13 where, on average, smearing leads to smaller reconstructed momenta due to Bremsstrahlung effects. This results in higher single lepton efficiencies for the low to medium range of momenta. Only at very large momenta of  $p > 1800$  MeV/c is a decreased efficiency noticeable. Because the majority of leptons in the cocktail will have smaller momenta than this, an overall increased pair efficiency is observed.

Apart from this, all models lead to very similar estimations, supporting the assumption of an adequate cocktail simulation and no model dependence in the spectra corrections. For the remaining analysis, the mean of all models is taken as the final pair efficiency correction factor. Deviations from this mean from each model are added to the systematic uncertainties.

With this average correction factor, one can further compare the impact of embedding single leptons to data vs embedding to UrQMD events. Figure 3.15 indicates how differences due to embedding are smaller than variations due to smearing effects. Still, embedding to real data suggests an overall smaller efficiency than embedding to UrQMD. This indicates that UrQMD alone should not be trusted to perfectly reproduce realistic

conditions. Since embedding to actual data does not introduce any further model dependency, this approach has been chosen for the remaining analysis.

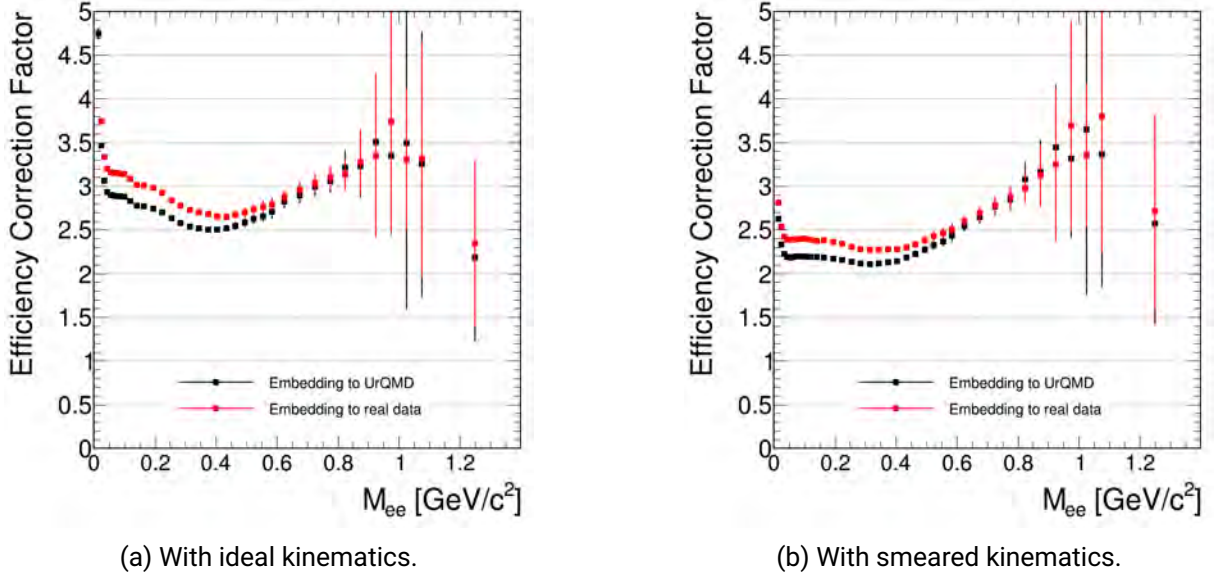


Figure 3.15: Mean pair efficiency factors with embedding to UrQMD vs embedding to real data in dependence of the invariant mass for Ag+Ag collisions, 0-40% centrality, at  $\sqrt{s_{NN}} = 2.42$  GeV. Vertical lines represent statistical uncertainties.

### 3.4.4 Freeze-out Cocktail Multiplicities

An important element of the correction procedure is the simulation of a realistic cocktail. While the  $\rho$  meson is assumed to decay within the fireball itself, further dilepton decay possibilities during the freeze-out can be identified for the collision energies of  $\sqrt{s_{NN}} = 2.42$  GeV [8]:

- $\pi^0 \rightarrow \gamma + e^+e^-$
- $\eta \rightarrow \gamma + e^+e^-$
- $\omega \rightarrow \pi^0 + e^+e^-$
- $\omega \rightarrow e^+e^-$
- $\phi \rightarrow e^+e^-$

Events with each of these decays are generated using Pluto. The resulting spectra of the individual dilepton sources are combined into a spectrum that reflects the whole freeze-out cocktail. This is only possible, however, if each source is properly normalised to its yield per event. Therefore, the multiplicities of all dilepton sources need to be known in order to generate the cocktail sum. Ideally this is based on experimental measurements.

First, in case of pions, one can approximate the number of neutral pions based on the measurements of their charged counterparts [42]:

$$N_{\pi^0} \approx \frac{1}{2}(N_{\pi^+} + N_{\pi^-}) \quad (3.8)$$

While final results are still to be determined, first evaluations have estimated the number of pions per participating nucleon and per event at 0.055 during the Ag+Ag experiment at 1.23A GeV. Further, a linear  $\langle A_{part} \rangle$  scaling of pions is well established [42], allowing for the extrapolation of  $\pi^0$  multiplicity to all centrality bins.

Second, the  $\eta$  yield is determined from TAPS measurements [43]. Figure 3.16 shows the behavior of  $\pi^0$  and  $\eta$  at different energies and for two collisions systems of Ca+Ca and C+C. On this basis, a yield of  $8 \cdot 10^{-4}$  per event and participating nucleon is extracted for Ag+Ag at  $\sqrt{s_{NN}} = 2.42$  GeV. As is investigated in section 4.3, a linear scaling of  $\eta$  with  $\langle A_{part} \rangle$  is again assumed. Other than that, the TAPS measurements [43] also provide a first cross check of expected pion multiplicities at 1.23A GeV. In this context, the value from HADES at 0.055 is found to be consistent.

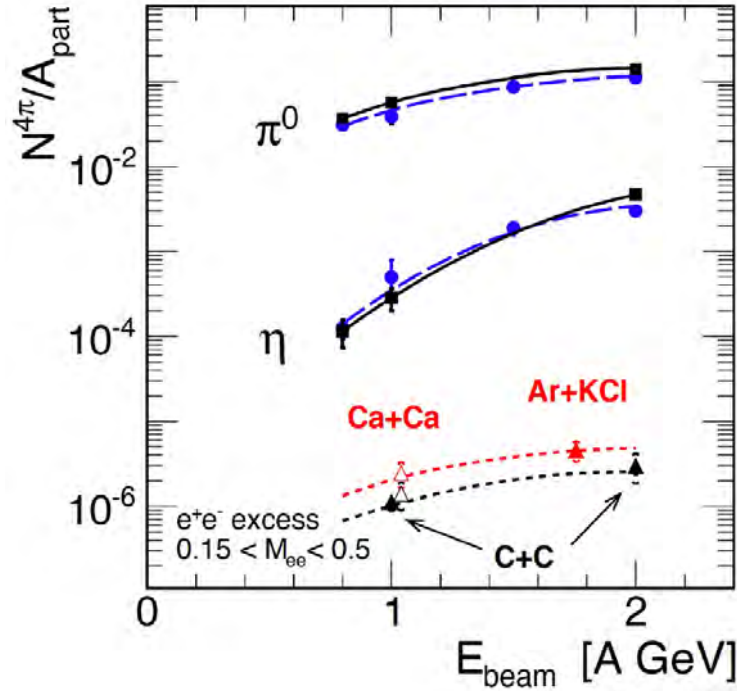


Figure 3.16:  $\eta$  and  $\pi^0$  multiplicity for different systems and energies. Figure taken from [44].

Third, no direct measurements of  $\phi$  or  $\omega$  mesons for Ag+Ag collisions at  $\sqrt{s_{NN}} = 2.42$  GeV are available. However, the HADES collaboration also recorded Ag+Ag events at 1.58A GeV and Au+Au events at 1.23A GeV. For these experiments, analyses have been conducted where the  $\phi$  yield is determined via its dominant decay into  $K^+K^-$ . From this, it has been concluded that the number of  $\phi$  mesons per event and per participating nucleon is at  $3 \cdot 10^{-7}$  in Ag+Ag collisions at 1.58A GeV. In order to translate this to an energy of 1.23A GeV, an energy dependence factor  $e$  is determined by the comparison to Au+Au:

$$e = \left( \frac{102}{193} \right)^{4/3} \frac{Mult_{\phi}(Au + Au; 1.23AGeV)}{Mult_{\phi}(Ag + Ag; 1.58AGeV)} \approx 0.2 \quad (3.9)$$

Where 102 and 193 are the mean number of participants in the investigated centrality classes.

In this context, the scaling per number of participants also needs to be taken into account. For vector mesons, previous analyses have estimated a dependence of  $\propto \langle A_{part} \rangle^{4/3}$  [29].

Finally, the  $\omega$  signal has been reconstructed for Ag+Ag collisions at 1.58A GeV in the analysis of dilepton spectra. As with the  $\phi$  meson, this measurement is translated to energies of 1.23A GeV by the analogous application of the energy factor  $e$  from equation 3.9.

Table 3.2 summarises the multiplicities of the freeze-out cocktail components:

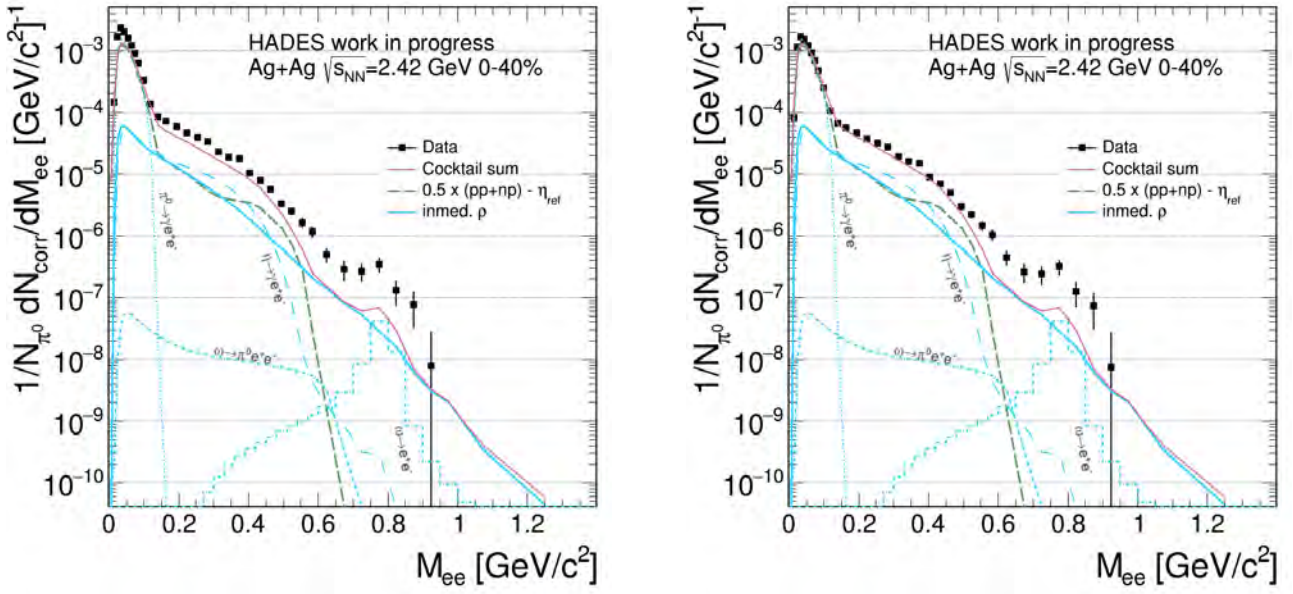
Dilepton Source	Branching Ratio: $e^+e^-$	Multiplicity/ $A_{part}$
$\pi^0 \rightarrow \gamma + e^+e^-$	$1.174 \cdot 10^{-2}$	$5.5 \cdot 10^{-2}$
$\eta \rightarrow \gamma + e^+e^-$	$6.9 \cdot 10^{-3}$	$8 \cdot 10^{-4}$
$\omega \rightarrow \pi^0 + e^+e^-$	$7.7 \cdot 10^{-4}$	$6.91 \cdot 10^{-6}$
$\omega \rightarrow e^+e^-$	$7.3 \cdot 10^{-5}$	$6.91 \cdot 10^{-6}$
$\phi \rightarrow e^+e^-$	$2.95 \cdot 10^{-4}$	$4.15 \cdot 10^{-8}$

Table 3.2: Freeze out cocktail sources and their multiplicities for Ag+Ag at  $\sqrt{s_{NN}} = 2.42$  GeV.

It can be noted that the yield of the  $\phi$  meson is by far the smallest in comparison to the other dilepton sources. In fact, it is about two orders of magnitude smaller than the multiplicity of the  $\omega$  meson. Consequently, it has a negligible contribution to the overall cocktail and is not taken into account in this analysis.

### 3.4.5 Comparison of Dilepton Cocktail to Data

A first validation of the credibility of the cocktail and of the determined efficiency correction can be made by comparison of the measured invariant mass spectrum to the cocktail in acceptance. Figure 3.17 shows how the freeze-out cocktail sources, the reference spectrum from elementary NN-collisions and the inmedium  $\rho$  contribute to the dilepton signal. In this case, the inmed.  $\rho$  is simulated for Au+Au collisions via coarse graining methods and scaled to each centrality class by the mean number of participants by assuming  $\propto \langle A_{part} \rangle^{\frac{4}{3}}$  [29].



(a) With ideal kinematics and embedding to real data. (b) With smeared kinematics and embedding to real data.

Figure 3.17: Efficiency corrected signal in comparison with Pluto cocktail for Ag+Ag collisions, 0-40% centrality, at  $\sqrt{s_{NN}} = 2.42$  GeV. The cocktail sum consists out of the  $\eta$ ,  $\omega$ ,  $\rho$  signal as well as the signal from elementary  $pp$  and  $np$  collisions. The latter has been measured at 1.25A GeV. The inmed.  $\rho$  is based on coarse-graining calculations. Vertical lines represent statistical uncertainties.

For ideal kinematics, the corrected data clearly overshoots the cocktail sum. This could potentially be a sign of over-correction. For smeared kinematics, the corrected data consists within 30% with the cocktail sum at mass regions below  $0.5 \text{ GeV}/c^2$ . The remaining difference could be attributed to the possibility that the cocktail spectra from Pluto do not yet accurately describe reality. Another explanation for the deviation is that the inmedium  $\rho$ , calculated with a coarse-graining approach, needs to be calculated for the Ag+Ag system. All in all, further investigations will be necessary to confirm the efficiency corrections. For the purpose of this analysis, the efficiencies based on smeared kinematics have been found to be closer to the calculated cocktail. They are also an arguably more realistic approach to do efficiency corrections, and, as such, will be used for the rest of the analysis.

Therefore, an analogous comparison of Pluto cocktail to corrected data can be presented for every 10% centrality class in figure 3.18.

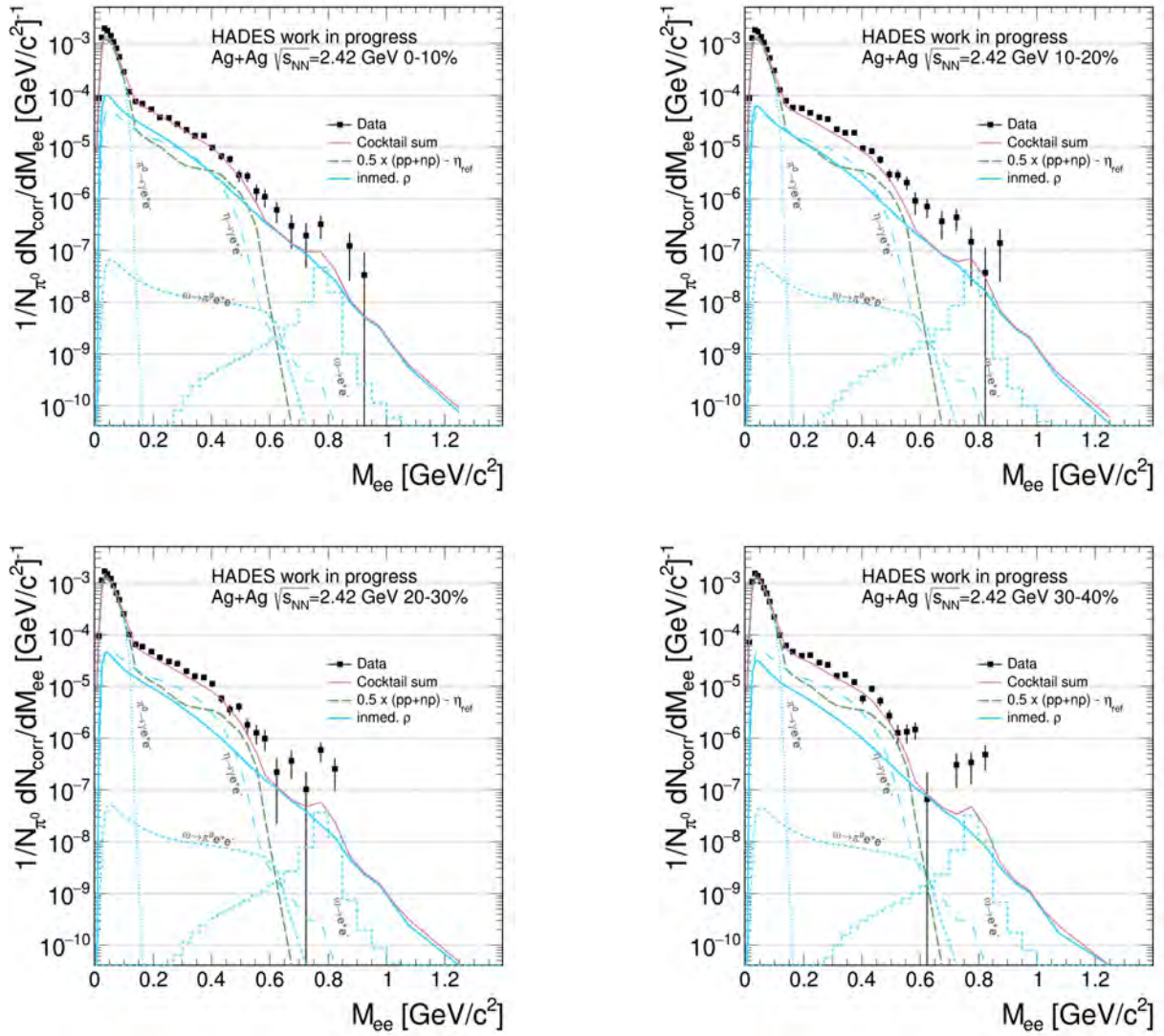


Figure 3.18: Efficiency corrected signal in comparison with Pluto cocktail for Ag+Ag collisions at  $\sqrt{s_{NN}} = 2.42$  GeV. Efficiency correction is based on embedding to real data and smeared kinematics. The cocktail sum consists out of the  $\eta, \omega, \rho$  signal as well as the signal from elementary  $pp$  and  $np$  collisions. The latter has been measured at 1.25A GeV. The inmed.  $\rho$  is based on coarse-graining calculations. Vertical lines represent statistical uncertainties.

### 3.4.6 Acceptance Corrections

On top of the efficiency correction, the same procedure, described above, is utilised to estimate necessary acceptance corrections, which includes the extrapolation to the unmeasured region of phase space. The central method to determine whether a given single lepton with momentum  $p$ , azimuthal angle  $\phi$  and polar angle  $\theta$  will hit the detector, is the detailed representation of the HADES detector in GEANT. On its basis, single lepton acceptance matrices can be calculated when embedding  $e^\pm$  to real or simulated events. Figure 3.19 shows the resulting single lepton acceptances. For the azimuthal angle  $\phi$ , the sector structure of the HADES detector is visible. For the momentum  $p$ , one can recognise a constant acceptance above around  $p = 200$  MeV/c. Hence, some momentum is necessary to reliably reach the detector but otherwise the directions of the particles are the determining factor for the acceptance. In contrast to efficiencies, the acceptance is, as expected, independent of embedding to real data or UrQMD since the detector coverage is analogous in both cases.

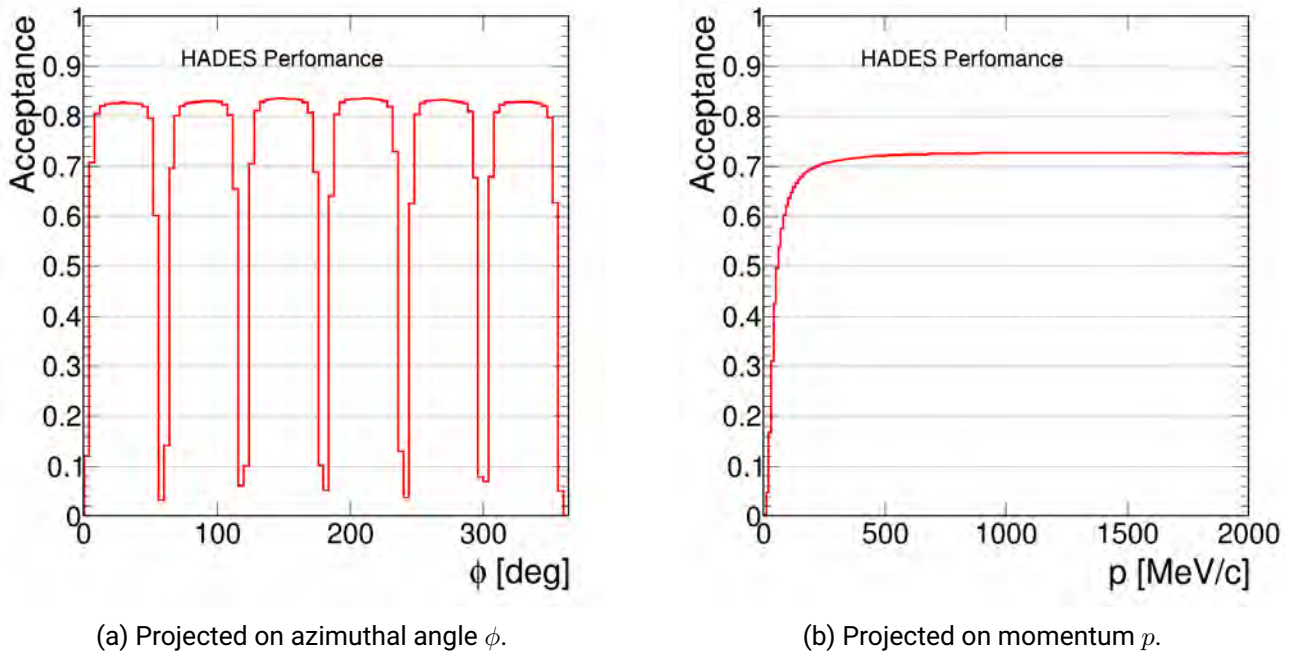


Figure 3.19: Single lepton acceptances projected on  $\phi$  and  $p$  for Ag+Ag collisions, 0-40% centrality, at  $\sqrt{s_{NN}} = 2.42$  GeV.

The single lepton acceptances are then used to simulate the cocktail with Pluto. Given a simulated lepton with kinematics  $p$ ,  $\phi$  and  $\theta$ , the acceptance is looked up in the single lepton acceptance matrix. Further, a random number  $x$  is generated from a uniform distribution between 0 and 1. If  $x$  is smaller than the looked-up acceptance, the lepton will be regarded as accepted. As long as this is repeated with a sufficient number of individual leptons, the overall acceptance will converge to the single lepton acceptances. In the end, applying this procedure in the Pluto simulations gives then an acceptance pair correction factor in dependence of the invariant mass  $M_{ee}$  as the ratio of the invariant mass spectrum of the whole  $4\pi$  region over the spectrum with accepted pairs.

Analogous to the efficiency corrections, see section 3.4.3, three models are implemented for the simulation of the cocktail. The resulting pair acceptance factors are presented in figure 3.20. While the model dependency

is greater than it has been for efficiency corrections, all models still lead to similar results. For the rest of the analysis, the mean of all models is used as the pair efficiency correction factor. Deviations from this mean are considered in the systematic uncertainties.

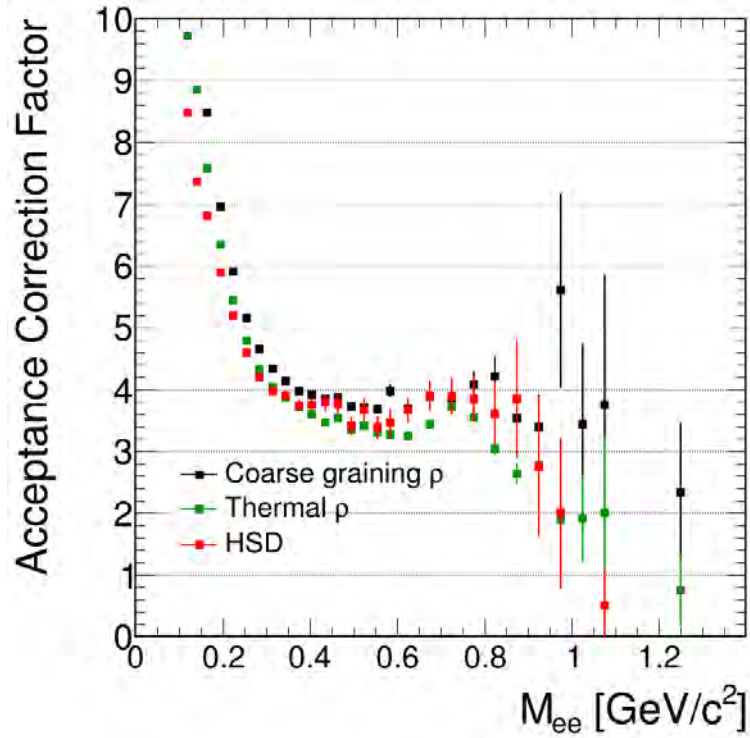


Figure 3.20: Pair acceptance factor in dependence of the invariant mass for Ag+Ag collisions at  $\sqrt{s_{NN}} = 2.42$  GeV. Vertical lines represent statistical uncertainties.

---

## 4 Analysis of Au+Au Data

---

Along with the Ag+Ag experiments at 1.23A GeV from March 2019, the HADES collaboration also measured Au+Au collisions at the same energy in April 2012. To allow for a direct comparison between the two systems, the Au+Au analysis needs to include more peripheral events, such that the number of participants overlap with the semi-central events from the Ag+Ag collisions. This extension to peripheral events causes some additional difficulties in the analysis which are to be discussed in this chapter.

---

### 4.1 Differences to the Ag+Ag Analysis

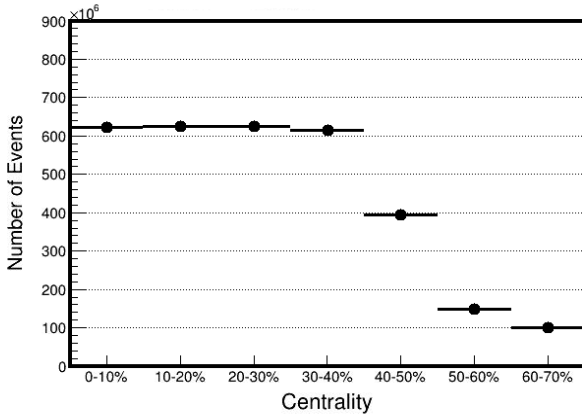
---

In principle, the steps needed to reconstruct the invariant mass spectrum are analogous between the Au+Au and Ag+Ag experiments. In fact, most methods described in chapter 2 for Ag+Ag were already tested and established in the course of the Au+Au analysis. One focus of this work is set to extend already existing Au+Au results to peripheral events and tackle the thereby emerging challenges. This has been started in previous works [27]. Nevertheless, at least an overview of the additional steps shall be given in this section. Moreover, the main differences to the current Ag+Ag analysis are to be emphasised.

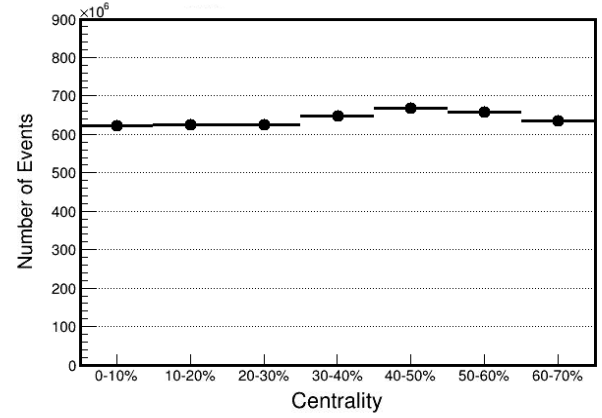
#### 4.1.1 Inclusion of PT2 Events

In a typical collision experiment at HADES, vast amounts of data are generated continuously in the course of the beam time. Ideally, the goal is to achieve high reaction rates and a sufficiently quick processing of data such that as many events as possible can be recorded in the shortest amount of time. However, not all registered signal are equally interesting for the later physics analyses. A dedicated trigger system needs to be implemented to immediately identify and remove background noise. Otherwise, the data acquisition system (DAQ) is occupied with processing such background and is unable to respond to more interesting events. In addition, the amount of required data storage would exceed capabilities. In order to counteract this situation, one important factor used to decide if a signal is saved or rejected are the physics triggers [45]. In the Au+Au experiment, a minimum requirement of 20 registered hits at the TOF detector defines the physics trigger 3 (PT3). A second conditions with at least 6 TOF hits is classified as physics trigger 2 (PT2). While every PT3 events is recorded, only every  $n$ -th PT2 events is stored. This is called down-scaling and leads to a reduction of unnecessary noise.

The effects of this are visible when looking at the number of recorded events per centrality class in figure 4.1. Up to 40% centrality, almost all events classify as PT3, but beyond that the number of recorded events decreases significantly. In order to analyse peripheral Au+Au collisions past 40% centrality, the procedure needs to be reversed by weighing each PT2 event by the inverse down-scaling factor  $1/n$ . From the beam log book,  $n$  is known to have been set at  $n = 4$  before the 15.04.2012 and  $n = 8$  afterwards. A corresponding correction leads to the expected roughly equal number of events for every centrality class.



(a) With down scaling.



(b) Corrected for down scaling.

Figure 4.1: Event Counter for different centrality classes with and without the effects of the down scaling procedure for Au+Au collisions at  $\sqrt{s_{NN}} = 2.42$  GeV.

#### 4.1.2 Lepton Identification via Multivariate Analysis

The lepton identification described in section 3.2 relies on a succession of individual conditions. Every cut by itself is likely to be insufficient for the dilepton analysis, but in sequence a satisfactory selection is achieved. A further improvement is theoretically possible by evaluating all particle characteristics simultaneously in a multivariate analysis. While still in development for Ag+Ag, such a procedure has been developed for the available Au+Au data from HADES via a multilayer perceptron (MLP) [36]. It takes as input a particle candidate and its features, and outputs the probability for the given candidate to be an electron/positron.

The input variables for the MLP can be listed in the following [36]:

- Particles velocity  $\beta$
- Energy loss  $dE/dx$  in the MDC.
- Kinematics of the particle in terms of momentum  $p$  and polar angle  $\theta$ .
- Distance of the track to the matched hit at the META detector.
- Information from RICH detector.

As such, it utilises similar information as described in section 3.2. But, in contrast to the sequential cuts, the MLP can take all these features into account at the same time. This also allows to consider correlations between the input features. All in all, it serves as a more sophisticated method to identify leptons reliably and is the method of choice for this analysis of Au+Au collisions.

---

## 4.2 Removal of Au+C Contamination

---

A large focus in the Au+Au analysis needs to be set on the investigation of so-called Au+C contamination. Such a contamination can occur due to the fact the HADES is a fixed target experiment. In the April 2012

experiment, the gold target was made up of thin gold foils, see section 2.1. To hold these metal plates securely in place, Kapton foils were used as structural material. While the best care is set on keeping only gold foils within the beam line, the beam itself is not guaranteed to hit the target perfectly. A slightly misaligned or dispersed beam has a chance to hit the surrounding Kapton foils, leading to Au+C contamination. In addition, the beam might hit surrounding detector material, i.e. the START detector, which similarly leads to Au+C collisions. In the case of the latter situation, a reconstruction of the event vertex is precise enough to see the where the collision originated. A simple vertex cut, see event selection in section 3.1, removes such samples from the analysis. Unfortunately, this is not sufficient to remove Au+C contamination coming from the target region itself. For this purpose, more sophisticated methods need to be implemented.

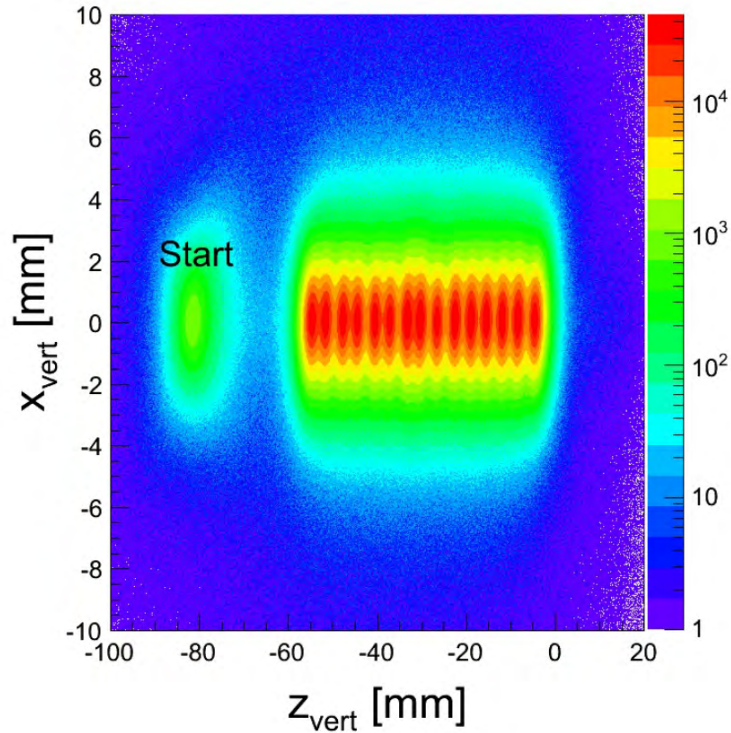


Figure 4.2: Events vertex positions in x-z plane for Au+Au collisions at  $\sqrt{s_{NN}} = 2.42$  GeV. One can recognise the START detector in front of the target material. Collision originating from detector material can be removed by a vertex cut.

In central Au+Au collisions, the number of participating nucleons is significantly higher than for any centrality of Au+C collisions. Since most analyses so far have been performed at 0-40% centrality, no further Au+C contamination countermeasures were needed. For the more peripheral events of 40-60% centrality in this analysis, however, the extent of Au+C contamination needs to be investigated. Essentially, a decision rule is to be found which can distinguish the collision system based only on the measured event characteristics. Different approaches have been suggested to develop such a tool, for example using information from the forward wall [46], but for this analysis a machine learning algorithm [47] is applied.

---

## 4.2.1 Functionality of Event-Purifier

The event-purifier, which aims to identify Au+C collision, consists out of two stages: First, an expectation-maximization algorithms divides the data into two clusters, one representing Au+C and the other one Au+Au events. It is therefore a process of unsupervised clustering. At the end of this phase, every event is assigned a probability of how likely it belongs to either cluster. Afterwards, the second stage is based on a neural network. It takes a number of measured event characteristics as well as the probabilities from the first stage as input, and outputs a value between 0 and 1, representing the probability that the given event is from an Au+Au collision. Ideally, this means an Au+C collision as input should result in a probability close to 0.

To train the neural network, Au+C events have been generated with UrQMD simulations. While one needs to keep in mind that this might not perfectly reproduce reality, it is the only way to reliably feed the neural network with correctly labelled training data. For the training of the purifier, the following event characteristics were evaluated [47]:

- Event vertex position along z-axis.
- Number of hits in TOF and RPC detector.
- Number of reconstructed tracks.
- Average event rapidity.
- Rapidity of an average particle.
- Ratio of total longitudinal energy to transverse energy.
- Ratio of total longitudinal momentum to total transverse momentum.
- Average longitudinal and transverse momentum.
- Average polar angle.

On this basis, two separate models have been trained due to the wide range of investigated centralities. To yield a better performance, model A is trained for more central (0-50% centrality) and model B for more peripheral (50-70% centrality) events. In the end, the performance of the combined model was validated in terms of purity and efficiency. On the one hand, all Au+C should be removed. On the other hand, the number of removed Au+Au should be minimal. Assuming less than 50% overall Au+C contamination, a purity of over 95% and efficiency of above 80% is estimated in simulations [47]. This proves promising and allows to extend the application of the purifier to the experimental data. However, along the way, it needs to be kept in mind that the true performance might be lower.

## 4.2.2 Effects of the Event-Purifier

The output of event-purifier is the confidence of the model that a given event is from an Au+Au collision. This gives the end user the freedom to choose which level of certainty is desired in the analysis by choosing a decision threshold  $p$  between 0 and 1. If the confidence is above  $p$ , the event will be kept in the analysis pool. If it is below  $p$ , the event will be rejected. To get a first insight of the effects of the purifier, the number of events with and without purifier can be plotted as in figure 4.3 with  $p = 0.5$ .

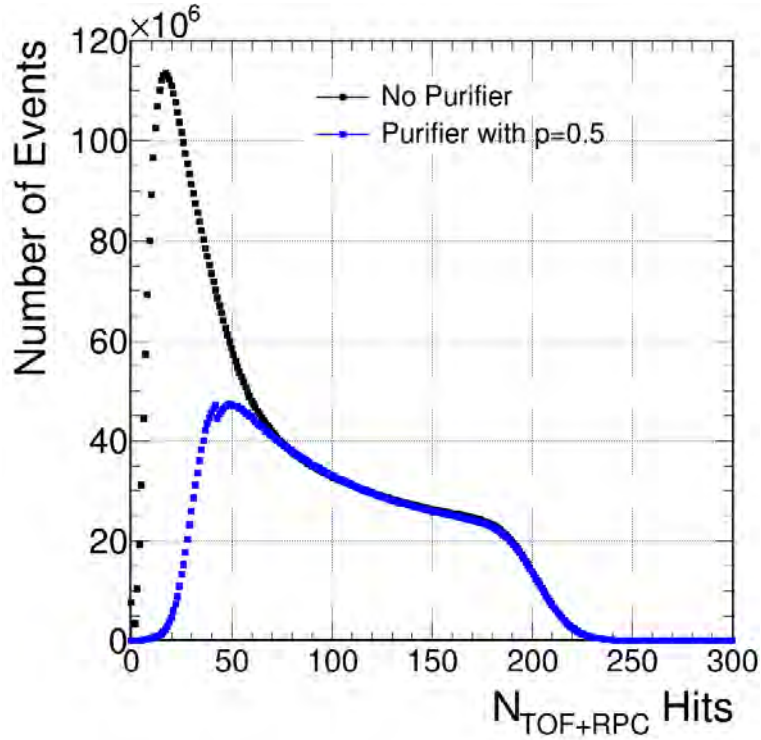


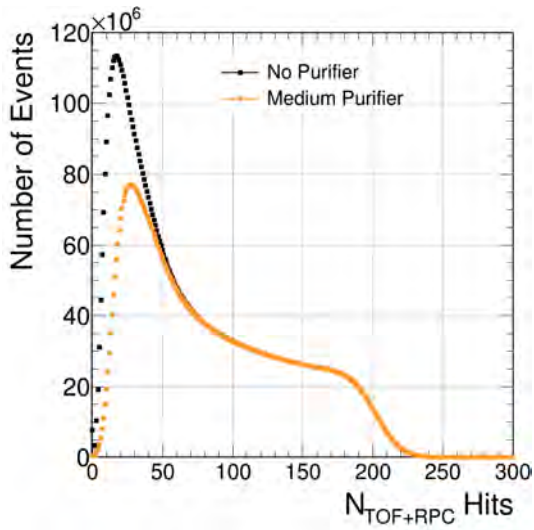
Figure 4.3: Number of events over number of TOF+RPC hits for Au+Au collisions at  $\sqrt{s_{NN}} = 2.42$  GeV.

Here, a discontinuity at  $N_{Hits}^{TOF+RPC} = 43$  is noticeable. This reflects the structure of the purifier. All events below  $N_{Hits}^{TOF+RPC} = 43$  are processed by model A, all events above by model B. Due to their independent training, the two models demonstrate a different level of strictness in how quickly they remove events from the sample. In order to take this contrariety into account, the decision thresholds of both models are set separately, such that it leads to a continuous distribution of events over  $N_{Hits}^{TOF+RPC}$ . In this analysis, three different settings are applied to investigate the effects of purifier: A strict setting, a medium setting, and no purifier usage at all. The corresponding decision thresholds  $p$  can be summarised in the following table:

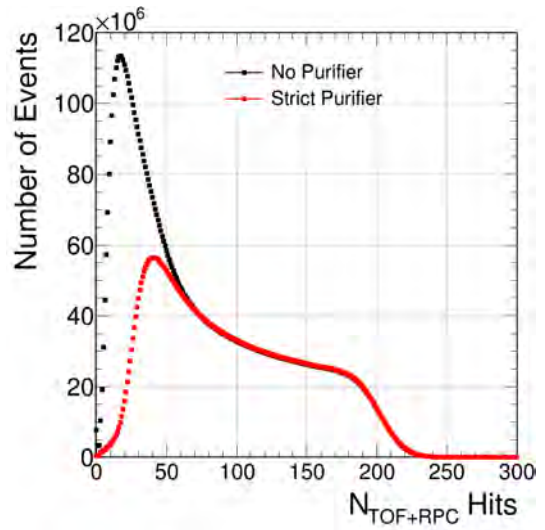
	$p_A$	$p_B$
<b>No Purifier</b>	0	0
<b>Medium Purifier</b>	$10^{-20}$	0.003
<b>Strict Purifier</b>	$10^{-9}$	0.3

Table 4.1: Decision thresholds for different Purifier settings.  $p_A$  and  $p_B$  are the thresholds for model A and B respectively.

Figure 4.4 demonstrates how these settings lead to a smooth distribution of events.



(a) Medium Purifier.



(b) Strict Purifier.

Figure 4.4: Number of events over number of TOF+RPC hits with different purifier settings for Au+Au collisions at  $\sqrt{s_{NN}} = 2.42$  GeV.

For all three settings, the dilepton analysis is performed. In order to investigate the effects of the purifier, a first insight is gained by looking at the number of events per 10% centrality bin. As seen in figure 4.5, collisions up to 40% centrality are not subject to Au+C contamination as the same number of events are measured with and without purifier. From 40% centrality onwards, the purifier starts to remove a noticeable number of identified Au+C events from the sample. In all cases, the strict purifier leads to the most significant deviations compared to the event pool without a purifier. This is seen most prominently at 50-60% centrality where almost one third of all measured events are rejected.

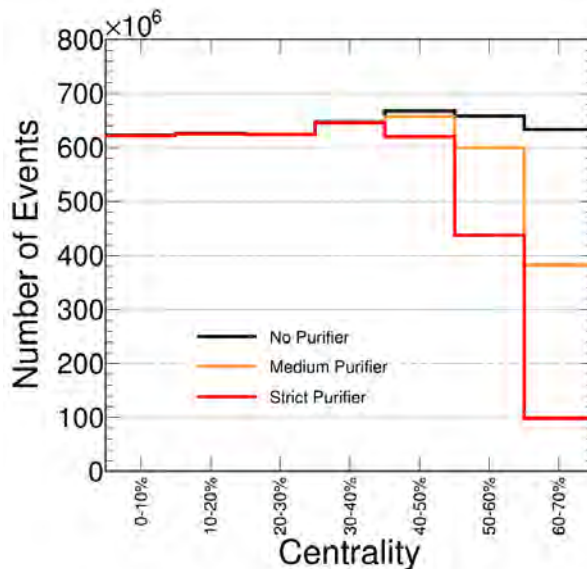


Figure 4.5: Number of events per centrality class with different purifier settings for Au+Au collisions at  $\sqrt{s_{NN}} = 2.42$  GeV.

Typically, one would, by definition, expect a roughly equal number of events per centrality class. Figure 4.5 demonstrates how the number of events is shifted considerably by the application of the purifier. This, in turn, could be an indication that the centrality bin borders, which were defined with unpurified data, are no longer valid. It is therefore necessary to verify that the existing centrality calculations hold true even after the application of the event-purifier.

### 4.2.3 Influence of Purifier on Centrality Selection

As has been seen in figures 4.4 and 4.5, the application of the event-purifier leads to a significant reduction of events in the analysis. It is therefore possible that the centralities determined in [18], which were based on all measured events, are no longer sustainable. To investigate this potential concern, a Glauber Monte Carlo simulation, see section 1.3.1, has been performed for the present analysis. The resulting Glauber MC model is then fitted to the event pool before and after application of the purifier. The resulting centrality bin borders are summarised in table 4.2:

Centrality Class	$N_{TOF+RPC}$ Reference	$N_{TOF+RPC}$ New - No Purifier	$N_{TOF+RPC}$ New - Medium Purifier	$N_{TOF+RPC}$ New - Strict Purifier
0-10%	158 - 312	157 - 285	157 - 281	161 - 282
10-20%	118 - 157	117 - 156	117 - 156	121 - 160
20-30%	83 - 117	84 - 117	84 - 116	87 - 120
30-40%	56 - 82	57 - 83	57 - 83	60 - 86
40-50%	37 - 55	37 - 56	37 - 56	39 - 59
50-60%	23 - 36	22 - 36	22 - 36	23 - 38

Table 4.2: Centrality class definitions for Au+Au collisions at  $\sqrt{s_{NN}} = 2.42$  GeV. Previous determinations made at HADES serve as a reference.

In order to verify that the Glauber MC model is properly implemented, the first comparison can be made between the results of this analysis without any purifier and previous centrality investigations performed at HADES. In general, the borders are in good agreement. Minor differences are most likely due to slightly different settings used for the fit, namely the fit range or starting values of the fit parameters. This is most prominently seen in the most central class of 0 – 10% centrality. Here, previous determination includes events up to  $N_{TOF+RPC} = 312$  instead of  $N_{TOF+RPC} = 285$ . While this might seem like a large discrepancy at first glance, figure 4.6 shows how the number of event in this extended range is almost negligible relative to the overall event count. Therefore, the newly performed Glauber Monte Carlo analysis is found to be consistent with previous results. As such, it is again repeated after application of the event-purifier with medium and strict settings. In case of the former, deviations from the original definitions are similarly minimal. Only the application of the strict purifier leads to some shifts. However, for every centrality class the relative change of  $N_{TOF+RPC}$  is below 10%. Figure 4.6 shows the the fitted Glauber MC, based on data without any purifier, with the data of all purifier settings:

As expected already from figure 4.5, the number of events is unchanged for central collisions. Only once the number of participants, and thereby the number of produced charged particles  $N_{TOF+RPC}$  decreases, a decline in counted events after purification is visible. Noticeably, this reduction does not necessarily lead to a worse alignment of fit vs data. Instead, the data without any purifier is found to have a higher cross section between around  $N_{TOF+RPC} > 15$  and  $N_{TOF+RPC} < 50$ . In this range, the Glauber MC model based

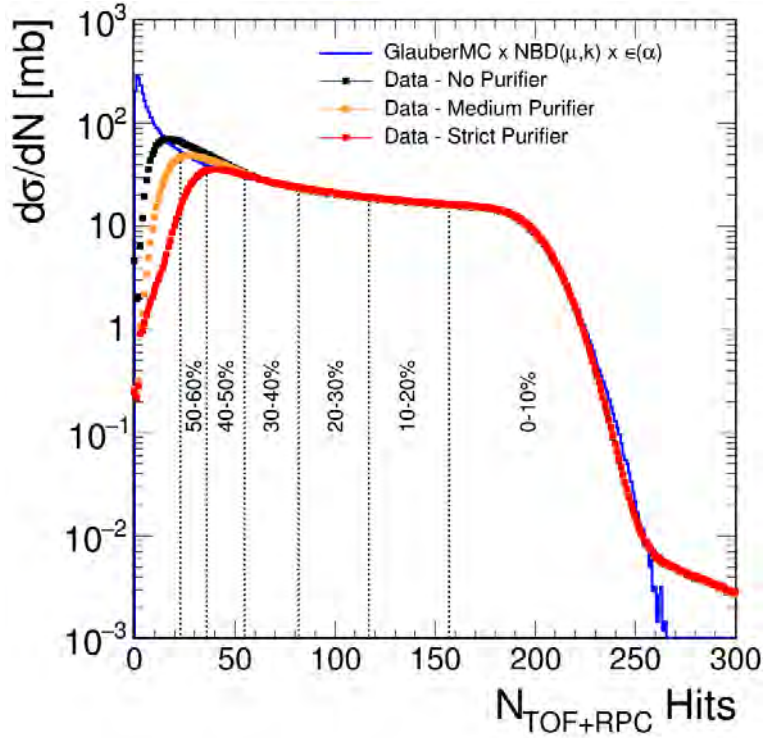


Figure 4.6: Comparison of cross section as function of  $N_{TOF+RPC}$  with different purifier settings for Au+Au collisions at  $\sqrt{s_{NN}} = 2.42$  GeV.

on Au+Au collisions shows a noticeable deviation from the data. One explanation for this behavior is Au+C contamination, something not accounted for in the Glauber MC model. This assumption is supported by the fact that the purifier causes an apparent convergence of data to fit.

In the end, the data after purifier application continues to have a good alignment with the fitted Glauber MC. Minor shifts in the centrality class definitions are only found for the strict purifier. However, this shift is within systematic uncertainties originating from the input parameters as well as from the fit settings [18]. Consequently, the official centrality class definitions can be used for this analysis even after application of the event-purifier.

### 4.3 Isolation of Excess Pairs

On the basis of the methods described in chapter 3, the invariant mass spectra for the Au+Au collisions at  $\sqrt{s_{NN}} = 2.42$  GeV have been reconstructed. For both Ag+Ag and Au+Au, the region of greatest interest is at invariant masses of around  $0.2 \text{ GeV}/c^2$  to  $0.8 \text{ GeV}/c^2$ , as this is where the inmedium  $\rho$  acts as the most prominent dilepton source. However, as seen in figure 3.17, a significant contribution to the dilepton signal in this range also comes from elementary nucleon-nucleon collisions in the early stages of the collision, as well as from the decay of  $\eta$  mesons at the freeze out. In order to isolate the signal coming from the hottest and densest stage, these components need to be subtracted.

While the reference spectrum is known from the measurement of elementary  $np$  and  $pp$  collisions at 1.25A GeV, the  $\eta$  spectrum needs to be estimated by other means.

The starting point for this endeavour is the  $\eta$ -spectrum generated in Pluto simulations. In order to subtract it from the measured dilepton signal, this spectrum needs to be normalised in terms of  $\eta$ -multiplicity in the given collision system and centrality. However, a precise estimation of the multiplicities is not always available. In case of Au+Au, the  $\eta$  yield has been determined for 0-40% centrality [44]. This determination is based on the decays of  $\eta$  mesons to  $\gamma\gamma$  with subsequent conversion of both photons into dilepton pairs. This is referred to as the photon conversion method and is accompanied with an increasing experimental challenge to measure a precise yield for smaller centrality bins with less statistics.

One can instead extrapolate the single measurement from 0-40% centrality via the mean number of participants  $\langle A_{part} \rangle$ :

$$\frac{dN_{\eta}}{dM} \propto \langle A_{part} \rangle^{\alpha} \quad (4.1)$$

From [43] the values of  $\alpha$  are known to be  $\alpha = 0.8$  at 2A GeV and  $\alpha = 1.2$  at 1A GeV. These can be understood as upper and lower limits for the experiments at 1.23A GeV.

On this basis, a linear scaling of  $\eta$  with  $\langle A_{part} \rangle$  is assumed in this analysis. In order to evaluate the uncertainty of this hypothesis, the excess spectrum is also extracted with  $\alpha = 0.8$  and  $\alpha = 1.2$ . The relative, maximum deviations between a linear scaling to the lower and upper bound can then be shown in figure 4.7. One can identify the relative differences to be below 10% in the whole invariant mass range. This can be taken into account in the overall systematic error estimation and is found to be acceptable in comparison to the overall accuracy of the experiment.

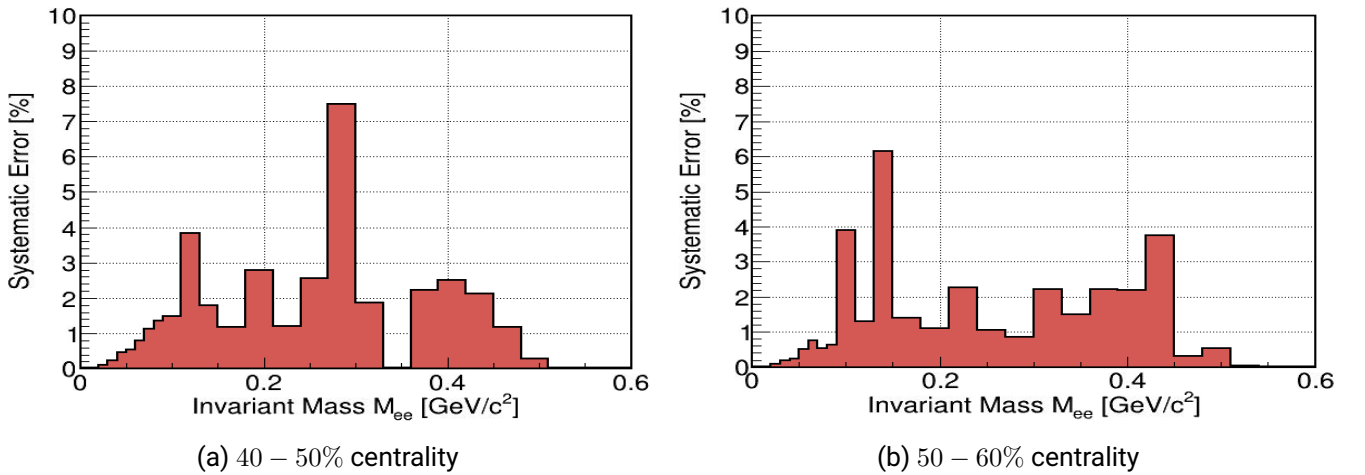


Figure 4.7: Relative systematic errors over mass due to extrapolated  $\eta$ -spectrum for Au+Au collisions at  $\sqrt{s_{NN}} = 2.42$  GeV.

Once the reference and  $\eta$  contribution have been subtracted, the remaining dilepton signal can be interpreted as the excess dilepton pairs relative to elementary collisions.

---

## 4.4 Estimation of Systematic Uncertainties

---

Virtually every assumption and procedure employed in this analysis is subject to systematic uncertainties. It is therefore necessary to estimate the confidence of each step in order to come to a trustworthy conclusion. For the purpose of this analysis, the following aspects are taken into account:

- **Calculation of Combinatorial Background:** While the like-sign method is well established and lies on a mathematically sound foundation, one still needs to do confirm that the background is accurately described. This has been done in the Au+Au analysis in simulations [36]. The resulting maximum relative systematic error has been estimated to be at  $0.02 \cdot B/S$ , where  $B/S$  is the ratio of background to signal. This evaluation holds true also for Ag+Ag and is therefore employed in this analysis.
- **Acceptance and Efficiency Corrections:** For the Ag+Ag analysis, the acceptance and efficiency corrections have been performed on the basis of three models to generate the dilepton cocktail. Differences between these models are taken as systematic uncertainties in the corrections. For the Au+Au analysis, an additional error of 20% is added for the extrapolation of efficiencies to peripheral events [27].
- **Normalisation to the number of pions:** The pion multiplicity per event, as discussed in section 3.4.4 is subject to systematic uncertainties. In this analysis, a relative error of 10% is introduced.
- **Reference subtraction:** The reference spectrum, used for the isolation of excess pairs, is the result of a previous measurement of elementary  $np$  and  $pp$  collisions. In the spectrum reconstruction of this measurement, systematic uncertainties have been estimated and need to be propagated accordingly.
- **Eta subtraction:** The uncertainties of the eta spectrum are rooted in the  $\langle A_{part} \rangle$  scaling. Their extent is estimated in section 4.3 via an upper and lower bound on the scaling parameter  $\alpha$ .

Assuming all errors to be independent from one another, the total systematic uncertainty is finally calculated by adding the contributions in squares.

## 5 Evaluation of Dilepton Invariant Mass Spectra

At this point, the acceptance corrected invariant mass spectra can be presented in figure 5.1 and 5.2. They serve as the measured dilepton signal from excess pairs after subtraction of  $\eta$  and reference. They are also fully corrected for efficiency and acceptance. The shown temperature fit as well as the extraction of the dilepton excess yield will be described in the following sections.

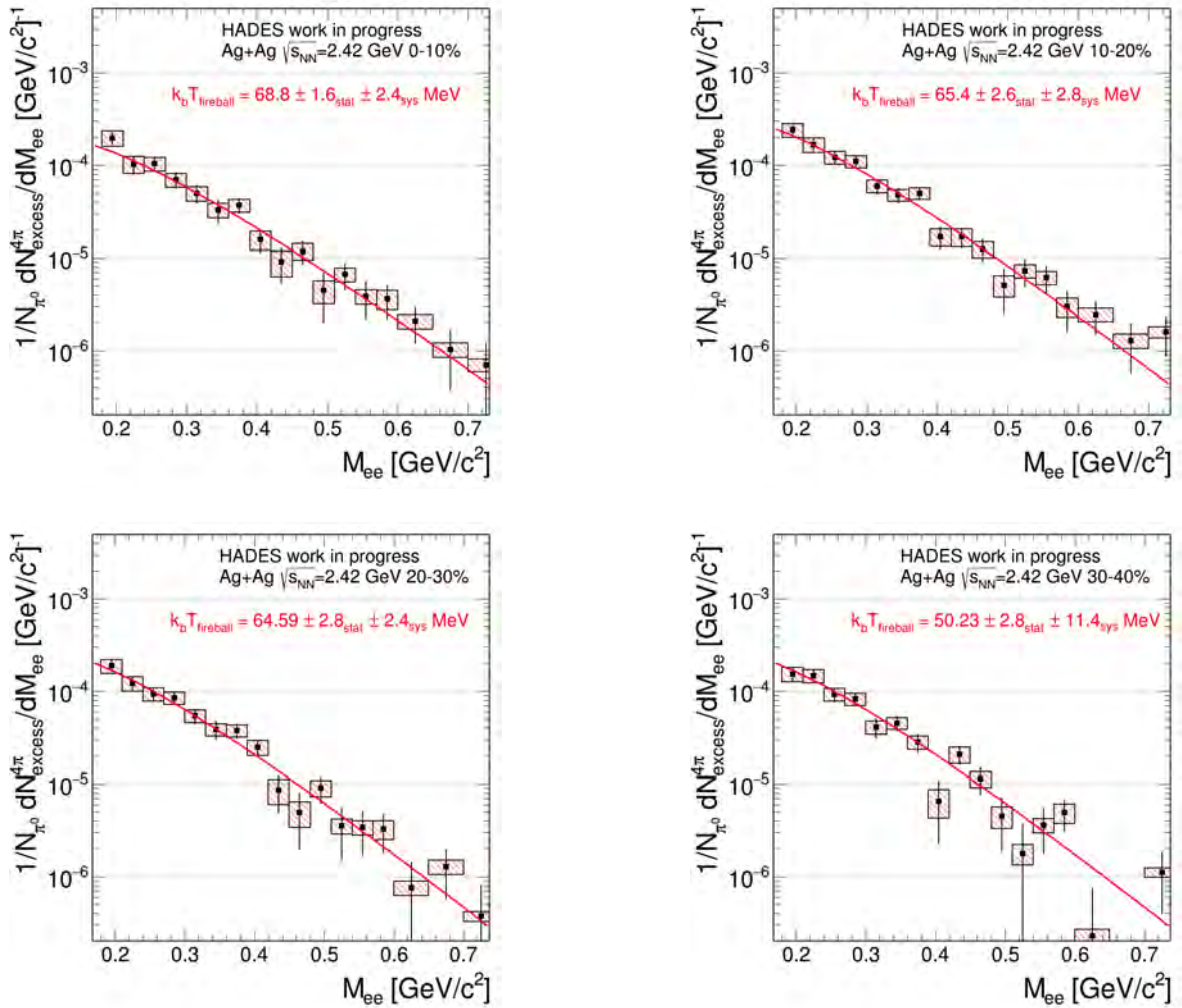


Figure 5.1: Acceptance corrected excess spectrum and temperature Boltzmann fit, see equation 5.2, for Ag+Ag collisions at  $\sqrt{s_{NN}} = 2.42$  GeV. Vertical lines represent statistical uncertainties. Boxes represent systematic uncertainties.

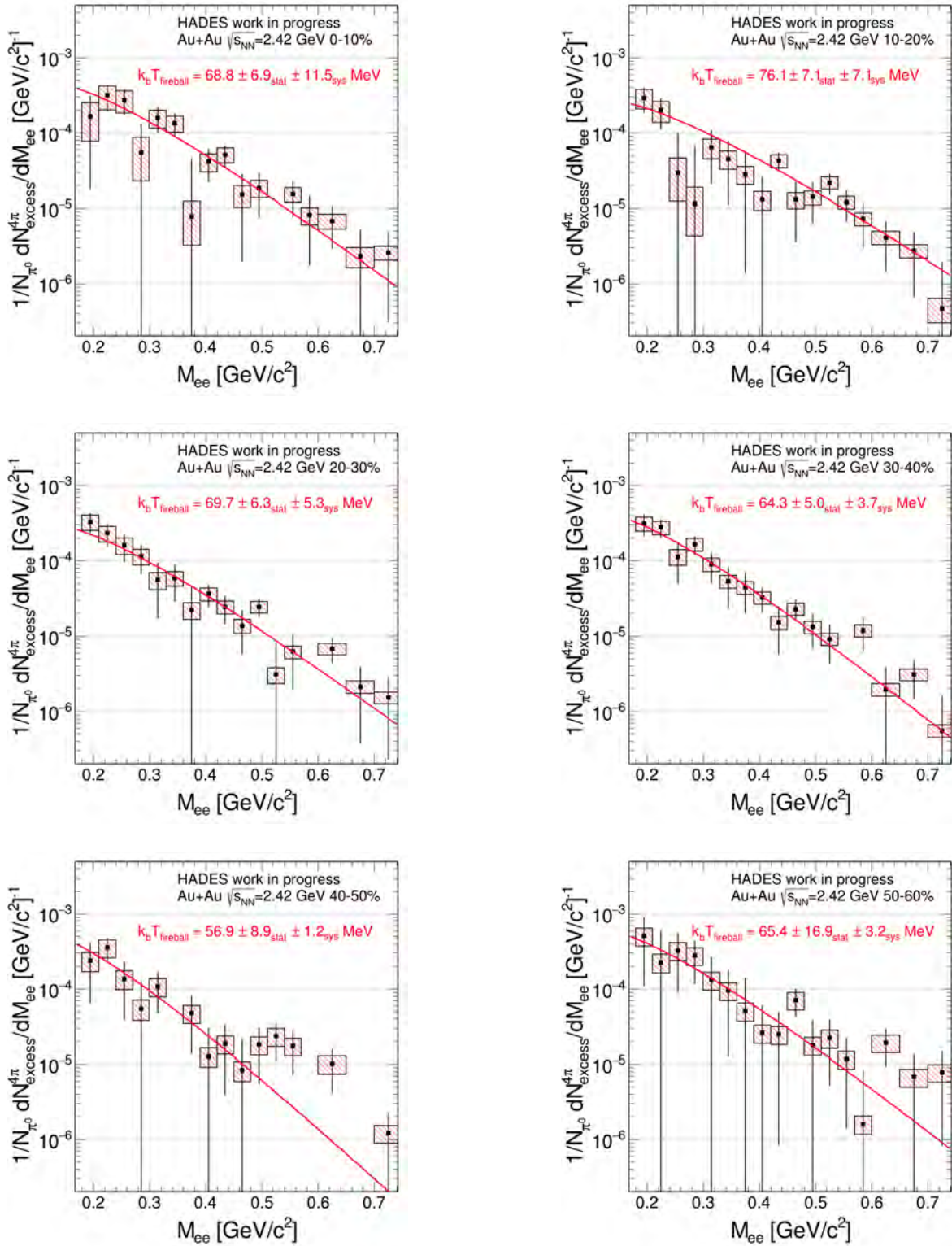


Figure 5.2: Acceptance corrected excess spectrum and temperature Boltzmann fit, see equation 5.2, for Au+Au collisions at  $\sqrt{s_{NN}} = 2.42$  GeV. The event-purifier with medium settings has been applied. Vertical lines represent statistical uncertainties. Boxes represent systematic uncertainties.

## 5.1 Comparison of Excess Spectra between System Sizes

The reconstructed invariant mass spectra can further be compared between the two different collision systems. Figure 5.3 shows the total reconstructed spectrum of Au+Au (0-60% centrality) and Ag+Ag (0-40% centrality).

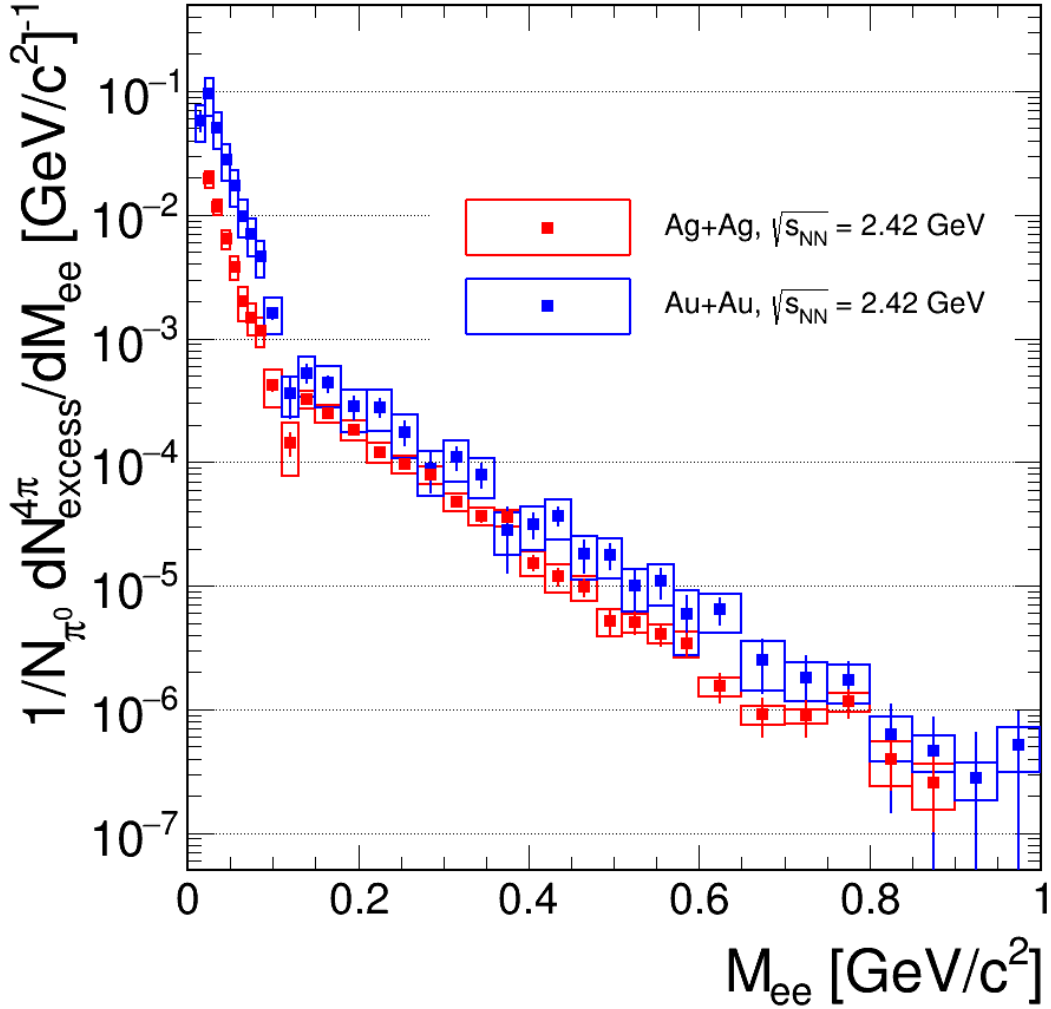


Figure 5.3: Reconstructed invariant mass spectrum of excess pairs. Au+Au is from 0-60% centrality. Ag+Ag is from 0-40% centrality. The event-purifier with medium settings has been applied for Au+Au. Boxes represent systematic uncertainties. Vertical lines represent statistical uncertainties.

The mean number of participants is known to be  $\langle A_{part} \rangle \approx 144$  for Au+Au at 0-60% centrality [48], and  $\langle A_{part} \rangle \approx 102$  for Ag+Ag at 0-40% centrality, see table 3.1. Therefore, a generally higher excess yield would be expected in the plotted Au+Au spectrum. Indeed, the number of dilepton pairs is larger for Au+Au in virtually every mass bin. Even if systematic and statistical uncertainties are taken into account, one can assume this statement to hold true.

In order to allow for a more direct comparison, one can find centrality bins of both collision systems with similar number of participants. Figure 5.4 shows the invariant mass spectra for Au+Au at 30-40% centrality

vs Ag+Ag at 10-20% centrality. These centralities both correspond to a mean number of participants of  $\langle A_{part} \rangle \approx 103$ .

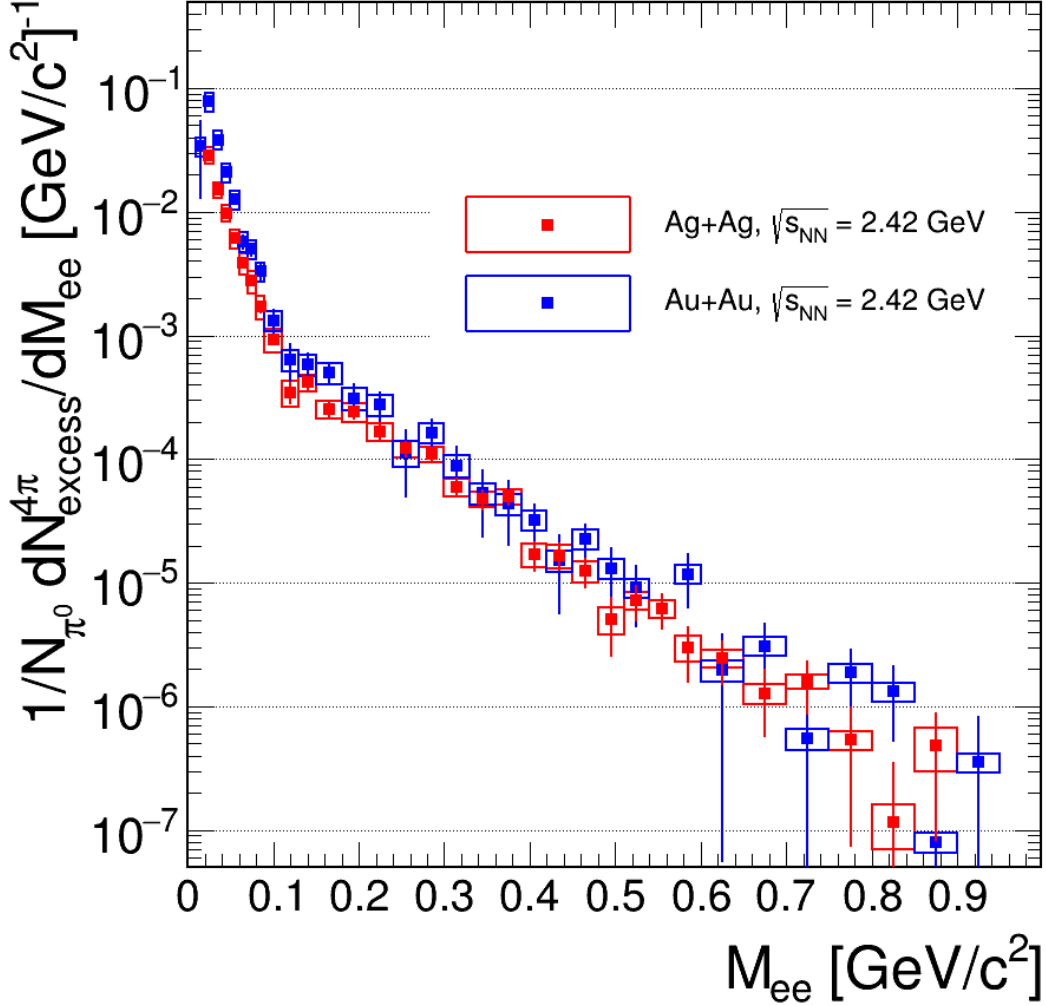


Figure 5.4: Reconstructed invariant mass spectrum of excess pairs. Au+Au is from 30-40% centrality. Ag+Ag is from 10-20% centrality. The event-purifier with medium settings has been applied for Au+Au. Boxes represent systematic uncertainties. Vertical lines represent statistical uncertainties.

On this basis, a few observations can be made. First, one should note that these smaller centrality bins lead to higher statistical errors. This, in turn, is also reflected in more statistical fluctuations, which become more and more apparent at higher invariant masses. Second, since the underlying number of participants is the same, any differences can be attributed to the system size. As both spectra have a similar shape, deviations are difficult to interpret when taking uncertainties into account. Only looking at the lower invariant masses of below  $0.24 \text{ GeV}/c^2$  the signal from Au+Au collisions is found to be definitely larger than Ag+Ag. However, this is also the region most strongly effected by the efficiency and acceptance corrections. In order to investigate any differences more quantitatively, the integrated excess yield and the temperature need to be determined.

## 5.2 Excess Yield Dependence on System Size and Centrality

As discussed in section 4.3, the greatest interest is in mass regions where the inmedium  $\rho$  contributes most strongly. To quantify this contribution at different centralities and for different systems, one can define an excess yield  $N_{excess}$  as the number of excess pairs in the integral from  $0.3 \text{ GeV}/c^2$  to  $\text{GeV}/c^2$ :

$$N_{excess} = \int_{0.3 \text{ GeV}/c^2}^{0.7 \text{ GeV}/c^2} \frac{dN}{dM} dM \quad (5.1)$$

Thereby, the integrated excess yield is a measure of the number of produced dileptons from the hottest and densest stage. In a first step,  $N_{excess}$  is determined for the Au+Au collisions with and without application of the purifier. The results can be presented in figure 5.5:

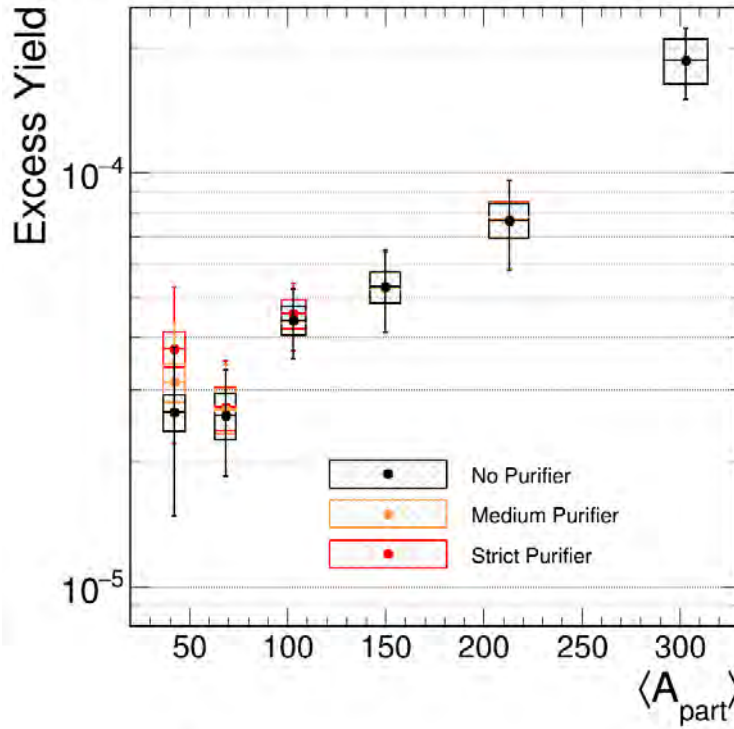


Figure 5.5: Excess yield of Au+Au collisions over  $\langle A_{part} \rangle$  with different purifier settings. Each data point represents a 10% centrality bin. Boxes represent systematic uncertainties. Vertical lines represent statistical uncertainties.

It can be noted, that the impact of the purifier is minimal up to 40% centrality. Afterwards, the application of the purifier leads to an increased yield relative to the unpurified data. This effect is most prominent at 50-60% centrality where this shift leads to a higher yield than at 40-50% centrality. Although statistical errors are similarly significant, such a behavior is generally unexpected and would challenge common understanding of decreasing yields with decreasing  $\langle A_{part} \rangle$ . This could occur, when the purifier has a bias to remove events without any dileptons. In this case, normalisation to the number of events, as it is done for the excess yield, leads to an apparent increase in signal per event. The overall number of measured dileptons is the same, but the reconstruction is based on fewer events. In this way, it remains an unanswered question for which

further investigations will be necessary. A similar application of a Ag+C purifier on the Ag+Ag will show if this behavior can be confirmed.

In addition to the Au+Au collision, the excess yield has analogously been extracted for the Ag+Ag collisions at the same energy. Figure 5.6 shows the comparison of the excess yield between the two collision systems.

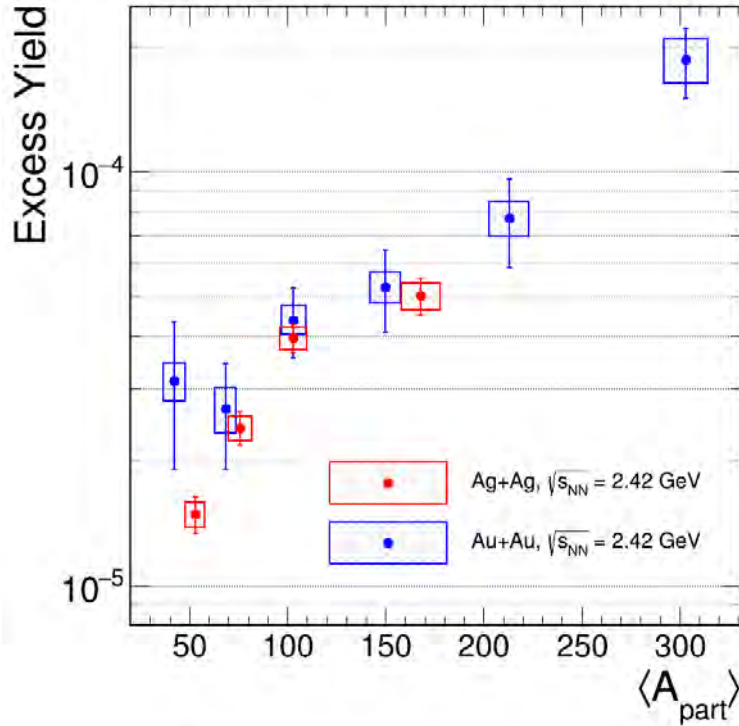


Figure 5.6: Excess yield over  $\langle A_{part} \rangle$  of Au+Au vs Ag+Ag collisions Each data point represents a 10% centrality bin. Medium purifier is applied to Au+Au data. Boxes represent systematic uncertainties. Vertical lines represent statistical uncertainties.

Here, differences between Au+Au and Ag+Ag are not definitive. A slightly higher excess yield for Au+Au relative to Ag+Ag is observed over all centralities. However, the systematic and statistical uncertainties would allow for the excess yield to be the same except for the 30-40% centrality bin of Ag+Ag. This serves as the only data point where the Ag+Ag yield is found to be clearly below the Au+Au collisions. In this regard, further evaluations will be essential. This includes additional systematic checks for both analyses in order to verify the procedures and assumptions made. If systematic and statistical uncertainties can be reduced, more confident conclusion can be made.

Furthermore, one can find more centrality bins, outside the 10% centrality bins used in this analysis, where the mean number of participating nucleons is the same for Ag+Ag and Au+Au collisions. Such investigations at the same  $\langle A_{part} \rangle$  will provide a more direct comparison between the two collision systems.

### 5.3 Temperature Dependence on System Size and Centrality

The produced invariant mass spectra, isolated to their excess pairs, is interpreted as the signal of the thermal dilepton radiation from the medium. As discussed in section 1.4.2, the spectra therefore entail the information about the fireball temperature  $T$ . It can be estimated by a Boltzmann fit of the form [36]:

$$\frac{dN}{dM} \propto M^{\frac{3}{2}} \exp(-M/T) \quad (5.2)$$

Hence, an exponential shape of the invariant mass spectrum is expected. From figure 5.3, this can be confirmed for the mass regions above  $0.2 \text{ GeV}/c^2$  as this is where the  $\rho$  meson is the dominant contribution. For lower masses, some  $\pi^0$  contribution is still visible. As a consequence, a fit range from  $0.2$  to  $0.7 \text{ GeV}/c^2$  is chosen for the temperature determination.

In a first step, the temperature is determined for the Au+Au collisions with and without application of the purifier. The results can be presented in figure 5.7:

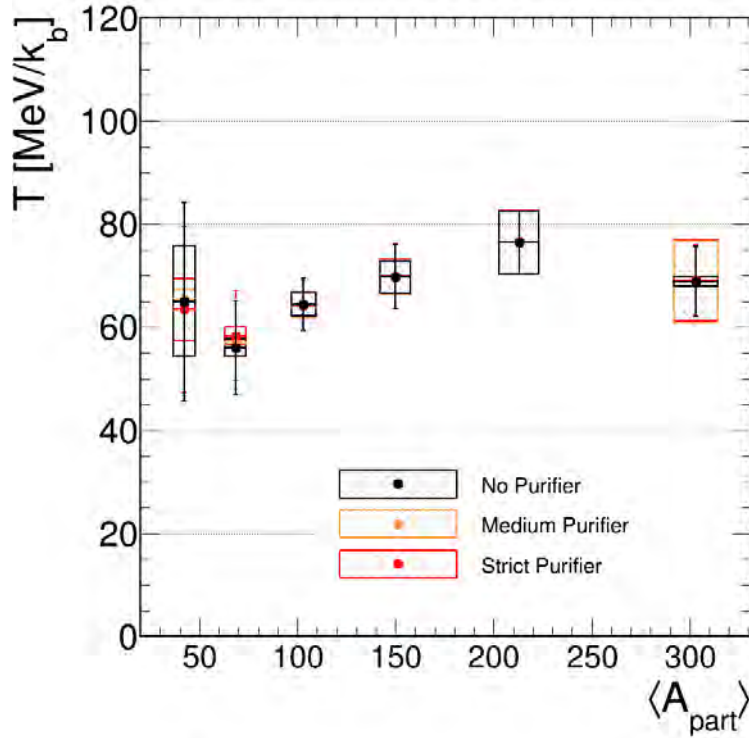


Figure 5.7: Fireball temperature of Au+Au collisions over  $\langle A_{part} \rangle$  with different purifier settings. Each data point represents a 10% centrality bin. Boxes represent systematic uncertainties. Vertical lines represent statistical uncertainties.

In general, a temperature downtrend for decreasing  $A_{part}$  can be observed. One exception of this trend is visible at 10-20% centrality where the temperature appears to be greater than for 0-10%. However, within errors this behavior can be understood. Apart from this, differences between the purifier settings remain minimal, even for peripheral collisions. One can conclude that the event-purifier does not impact the shape of the invariant mass spectrum significantly.

With this in mind, these results can be compared with the extracted fireball temperatures in Ag+Ag collisions:

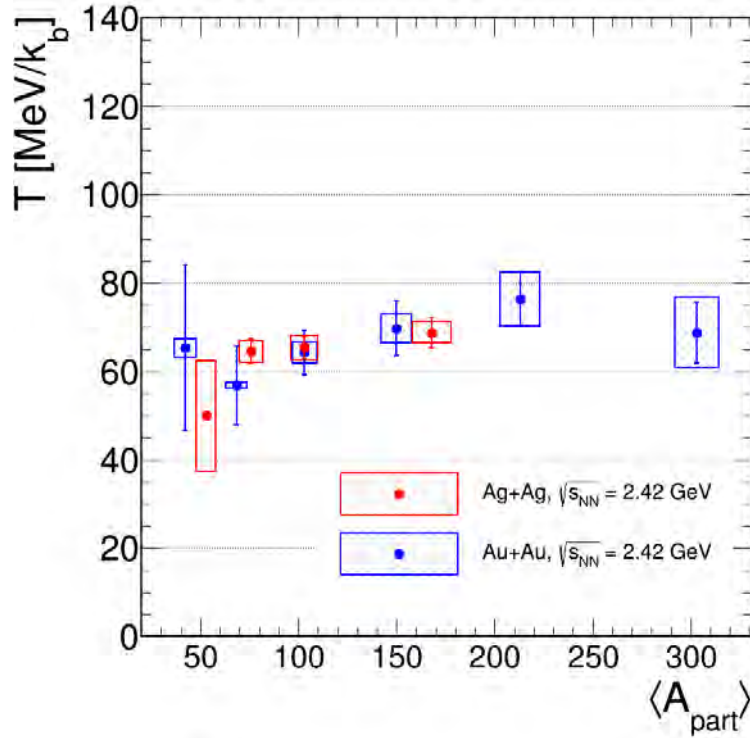


Figure 5.8: Fireball temperature over  $\langle A_{part} \rangle$  of Au+Au vs Ag+Ag collisions. Each data point represents a 10% centrality bin. Medium purifier is applied to Au+Au data. Boxes represent systematic uncertainties. Vertical lines represent statistical uncertainties.

As before, the Ag+Ag collisions show smaller temperatures with decreasing  $\langle A_{part} \rangle$ , although the differences between the three most central centrality bins is less pronounced than it is for Au+Au. In all cases, no significant deviations can be identified between the two collision systems. It can be concluded that current results indicate no notable impact of the system size on fireball temperatures.

## 5.4 Comparison to UrQMD Simulations

The centrality and system size dependence of the dilepton yield is also investigated on the basis of simulations [49]. They provide a prediction for dilepton spectra which can be compared to the experimental results. Figure 5.9 shows the dilepton spectra of the most central Ag+Ag and Au+Au collisions resulting from UrQMD calculations. In these 0-10% centrality bins, the underlying number of participants is 306 for Au+Au and 168 for Ag+Ag respectively. If one assumes a scaling of  $\propto \langle A_{part} \rangle^{\frac{4}{3}}$  [29], the Ag+Ag spectrum is to be expected to be approximately 0.45 times smaller than its gold counterpart. This factor matches closely to their ratio, plotted in the right panel, which stays virtually constant at about 0.4.

As a consequence, the depicted UrQMD model suggests no significant system size dependence on either the temperature of the fireball or the dilepton yield. This would be in agreement to the results in this analysis where any differences in the excess yield are still within uncertainties, and no impact of the ion species to the fireball temperatures is found. However, UrQMD is one of several transport models that allow for such a

comparison. From [49], it is known that they can lead to sizeable differences in the predictions. Therefore, a more detailed comparison of the experimental data with several models, and with centrality bins of the same mean number of participants, will allow for more definite conclusions.

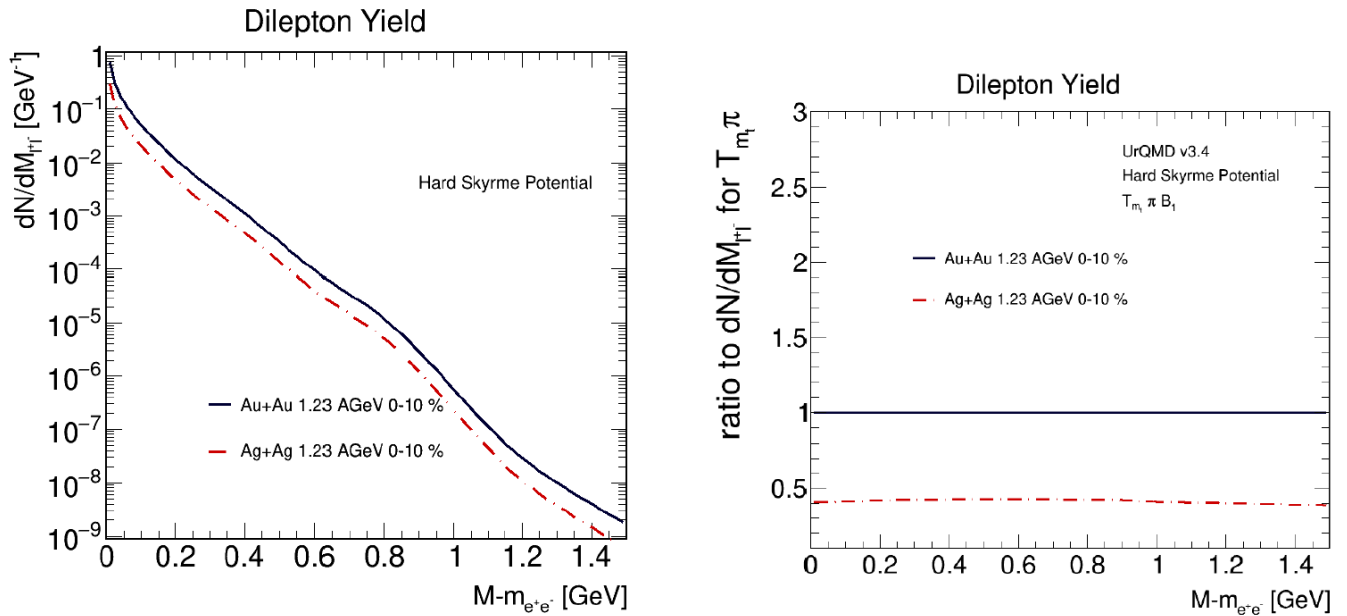


Figure 5.9: UrQMD predictions of invariant mass spectrum of Ag+Ag and Au+Au collisions at the same energy of 1.23AGeV and centrality of 0-10 %. The right panel shows their ratio. Figure taken from [49].

---

## 6 Summary and Outlook

---

In the course of this work, the thermal dilepton radiation of Ag+Ag and Au+Au collisions at 1.23A GeV has been investigated. The central tool for this purpose are the invariant mass spectra.

Starting with Au+Au, peripheral events up to 60% centrality have been included in the analysis, exceeding previous research with additional data points in the region of 40-60% centrality. In this context, an event-purifier has been applied in order to identify and remove potential Au+C contamination. Its effects have been investigated on the basis of three settings: No purifier usage, a medium setting, and a strict setting. Since a noticeable number of events is removed in the peripheral centrality bins, the impact on the centrality class definition needed to be checked by means of a Glauber MC analysis. Here, no change in the centrality borders has been found.

In addition to the Au+Au analysis, a first reconstruction of the Ag+Ag invariant mass spectrum up to 40% centrality has been performed. Because this is the first dilepton analysis of the Ag+Ag data at HADES, the acceptance and efficiency corrections needed to be done from the ground up. A comparison of smearing vs ideal kinematics as well as embedding into real data vs embedding into UrQMD events has been carried out. In the end, usage of smeared kinematics and embedding to real data is identified as the best way to realistically reproduce efficiencies. However, further checks are necessary to achieve a full understanding of the introduced corrections.

Nevertheless, by isolation of the excess pairs in both collision systems, the excess yield as well as the fireball temperature were determined. While definitive conclusion are not yet cemented, the yield for Au+Au is possibly larger than for Ag+Ag. In contrast to this, no system size dependence is recognised for the fireball temperature. Furthermore, for both temperature and excess yield, a downtrend with decreasing  $\langle A_{part} \rangle$  is identified. In a future step, this can be further quantified by a fit of the form  $\propto \langle A_{part} \rangle^\alpha$ .

All in all, this work can serve as a foundation to built upon and improve and concretise current findings. Notable improvements could be achieved by:

- **Multivariate analysis for lepton identification in Ag+Ag:** Previous research of Au+Au collisions has demonstrated the effectiveness of multivariate analysis for lepton identification. By taking several features into account at once, the efficiency as well as sample purity can be improved.
- **Self-consistency checks of corrections:** Acceptance as well as efficiency corrections should be consistent when different dilepton sources, i.e.  $\pi^0$  or  $\eta$  decaying into  $e^+e^-$  pairs and  $\gamma$ , are embedded into UrQMD or real data events. The resulting pair corrections can be compared to the pair corrections based on single lepton corrections. This serves as an important prerequisite to signify current estimations are realistic.
- **Advances on the event purifier:** In this work, the Au+C purifier and its effects have been tested. While this purifier is found to be not entirely satisfactory yet, a lot of experience has been gained. Since

---

carbon contamination is a reoccurring issue, also for peripheral Ag+Ag analyses, the development of an improved event-purifier will be beneficial.

---

## Bibliography

---

- [1] Peter W. Higgs. “Broken Symmetries and the Masses of Gauge Bosons”. In: *Phys. Rev. Lett.* 13 (1964). Ed. by J. C. Taylor, pp. 508–509. DOI: 10.1103/PhysRevLett.13.508.
- [2] Joseph D. Lykken. “Beyond the Standard Model”. In: May 2010. arXiv: 1005.1676 [hep-ph].
- [3] Georges Aad et al. “Observation of a new particle in the search for the Standard Model Higgs boson with the ATLAS detector at the LHC”. In: *Phys. Lett. B* 716 (2012), pp. 1–29. DOI: 10.1016/j.physletb.2012.08.020. arXiv: 1207.7214 [hep-ex].
- [4] [Online; last accessed 05-August-2021]. URL: <https://www.nobelprize.org/prizes/physics/2013/summary/>.
- [5] [Online; last accessed 26-July-2021]. URL: [https://en.wikipedia.org/wiki/File:Standard\\_Model\\_of\\_Elementary\\_Particles.svg](https://en.wikipedia.org/wiki/File:Standard_Model_of_Elementary_Particles.svg).
- [6] Akitomo Tachibana. *New Aspects of Quantum Electrodynamics*. 1st ed. 2017. 2017. ISBN: 9789811031328.
- [7] Harvey B. Meyer Huey-Wen Lin. *Lattice QCD for Nuclear Physics*. 1st ed. 2015. Vol. 889. 2015. ISBN: 9783319080222.
- [8] M. Tanabashi et al. “Review of Particle Physics”. In: *Phys. Rev. D* 98.3 (2018), p. 030001. DOI: 10.1103/PhysRevD.98.030001.
- [9] Volker Koch. “Introduction to chiral symmetry”. In: (Dec. 1995). arXiv: nucl-th/9512029.
- [10] K. Akerstaff et al. “Measurement of the strong coupling constant  $\alpha(s)$  and the vector and axial vector spectral functions in hadronic tau decays”. In: *Eur. Phys. J. C* 7 (1999), pp. 571–593. DOI: 10.1007/s100529901061. arXiv: hep-ex/9808019.
- [11] Paul M. Hohler and R. Rapp. “Evaluating chiral symmetry restoration through the use of sum rules”. In: *EPJ Web Conf.* 36 (2012). Ed. by Angela Badala et al., p. 00012. DOI: 10.1051/epjconf/20123600012. arXiv: 1209.1051 [hep-ph].
- [12] Szabolcs Borsanyi et al. “Is there still any  $T_c$  mystery in lattice QCD? Results with physical masses in the continuum limit III”. In: *JHEP* 09 (2010), p. 073. DOI: 10.1007/JHEP09(2010)073. arXiv: 1005.3508 [hep-lat].
- [13] Yoichiro Nambu and G. Jona-Lasinio. “Dynamical Model of Elementary Particles Based on an Analogy with Superconductivity. 1.” In: *Phys. Rev.* 122 (1961). Ed. by T. Eguchi, pp. 345–358. DOI: 10.1103/PhysRev.122.345.
- [14] Yoichiro Nambu and G. Jona-Lasinio. “Dynamical Model of Elementary Particles Based on an Analogy with Superconductivity. 2.” In: *Phys. Rev.* 124 (1961). Ed. by T. Eguchi, pp. 246–254. DOI: 10.1103/PhysRev.124.246.
- [15] Chihiro Sasaki. “Signatures of chiral symmetry restoration in dilepton production”. In: *Phys. Lett. B* 801 (2020), p. 135172. DOI: 10.1016/j.physletb.2019.135172. arXiv: 1906.05077 [hep-ph].

- 
- [16] Paul M. Hohler and R. Rapp. “Is  $\rho$ -Meson Melting Compatible with Chiral Restoration?” In: *Phys. Lett. B* 731 (2014), pp. 103–109. DOI: 10.1016/j.physletb.2014.02.021. arXiv: 1311.2921 [hep-ph].
- [17] [Online; last accessed 02-August-2021]. URL: <https://www.int.washington.edu/stephanov.html>.
- [18] J.Adamczewski-Musch et al. [HADES Collaboration]. “Centrality determination of Au + Au collisions at 1.23A GeV with HADES”. In: *The European Physical Journal A* 54.5 (May 2018). ISSN: 1434-601X. DOI: 10.1140/epja/i2018-12513-7. URL: <http://dx.doi.org/10.1140/epja/i2018-12513-7>.
- [19] J.Adamczewski-Musch et al. [HADES Collaboration]. “Probing dense baryon-rich matter with virtual photons”. In: *Nature Physics* 15 (2019). ISSN: 1040-1045. URL: <https://doi.org/10.1038/s41567-019-0583-8>.
- [20] Michael L. Miller et al. “Glauber modeling in high energy nuclear collisions”. In: *Ann. Rev. Nucl. Part. Sci.* 57 (2007), pp. 205–243. DOI: 10.1146/annurev.nucl.57.090506.123020. arXiv: nucl-ex/0701025.
- [21] Micah Buuck and Gerald Miller. “Corrections to Eikonal Approximation for Nuclear Scattering at Medium Energies”. In: *Physical Review C* 90 (June 2014). DOI: 10.1103/PhysRevC.90.024606.
- [22] Tetyana Galatyuk. “Di-electron spectroscopy in HADES and CBM: from  $p + p$  and  $n + p$  collisions at GSI to  $Au + Au$  collisions at FAIR”. PhD thesis. Frankfurt, 2009.
- [23] J. J. Sakurai. “Theory of strong interactions”. In: *Annals Phys.* 11 (1960), pp. 1–48. DOI: 10.1016/0003-4916(60)90126-3.
- [24] Y.F. Zhang T. Galatyuk R. Rapp. “Electromagnetic Radiation”. In: (). In preparation.
- [25] D. Dittert. “Electromagnetic Radiation from Au + Au Collisions at  $\sqrt{s_{NN}} = 2.4$  GeV Measured with HADES”. In: *Ukr. J. Phys.* 64.7 (2019). Ed. by Laszlo Jenkovszky and Rainer Schicker, pp. 560–565. DOI: 10.15407/ujpe64.7.560.
- [26] Dominique Dittert. “Azimuthal Anisotropy of Virtual Photons in Au+Au Collisions at  $s_{NN} = 2.4$ GeV”. Master Thesis. Darmstadt, 2018.
- [27] Niklas Schild. *Reconstruction of  $e+e^-$  in peripheral Au+Au collisions at  $\sqrt{s_{NN}}=2.42$  GeV with HADES*. Darmstadt, 2018. URL: <http://tuprints.ulb.tu-darmstadt.de/7771/>.
- [28] G. Agakishiev et al. “The High-Acceptance Dielectron Spectrometer HADES”. In: *Eur. Phys. J. A* 41 (2009), pp. 243–277. DOI: 10.1140/epja/i2009-10807-5. arXiv: 0902.3478 [nucl-ex].
- [29] Patrick Seilheim. “Reconstruction of the low-mass dielectron signal in 1.23A GeV Au+Au collisions”. PhD thesis. Frankfurt, 2017.
- [30] Jan Michel. *DAQ 2020 planned upgrades and wishlist*. Contribution to HADES Collaboration Meeting XXXVI. Frankfurt, 2019. URL: <https://indico.gsi.de/event/7689/contributions/34079/attachments/24726/30920/Daq2020.pdf>.
- [31] [Online; last accessed 03-August-2021]. URL: [https://hades-wiki.gsi.de/foswiki/pub/Collaboration/HadesLogos/HADES3D\\_AgAg\\_3840x2160\\_Labels.png](https://hades-wiki.gsi.de/foswiki/pub/Collaboration/HadesLogos/HADES3D_AgAg_3840x2160_Labels.png).
- [32] [Online; last accessed 26-July-2021]. URL: [https://www.gsi.de/forschungbeschleuniger/forschung\\_ein\\_ueberblick/hades\\_experiment/aufbau\\_des\\_hades\\_experiments](https://www.gsi.de/forschungbeschleuniger/forschung_ein_ueberblick/hades_experiment/aufbau_des_hades_experiments).
- [33] O. Svoboda et al. “Electromagnetic calorimeter for the HADES@FAIR experiment”. In: *JINST* 9 (2014). Ed. by Pietro Govoni et al., p. C05002. DOI: 10.1088/1748-0221/9/05/C05002.

- 
- [34] Adrian Rost. “Design, installation and commissioning of new read-out electronics for HADES ECAL and diamond detectors for T0-reconstruction and beam diagnostics”. PhD thesis. Darmstadt: Technische Universität Darmstadt, 2020. URL: <http://tuprints.ulb.tu-darmstadt.de/12235/>.
- [35] Szymon Harabasz. *Dileptons from Ag+Ag 1.23A GeV*. Contribution to Virtual IV HADES Physics Analysis Meeting. Darmstadt, 2021. URL: [https://indico.gsi.de/event/12556/contributions/54722/attachments/36379/48435/SzymonHarabasz\\_dileptons\\_HAM\\_June2021.pdf](https://indico.gsi.de/event/12556/contributions/54722/attachments/36379/48435/SzymonHarabasz_dileptons_HAM_June2021.pdf).
- [36] Szymon Harabasz. “Reconstruction of virtual photons from Au+Au collisions at 1.23 GeV/u”. Bachelor thesis. PhD thesis. Darmstadt, 2017.
- [37] Marek Gazdzicki and Mark I. Gorenstein. “Background subtraction from the dilepton spectra in nuclear collisions”. In: (Mar. 2000). arXiv: hep-ph/0003319.
- [38] I. Fröhlich et al. “Pluto: A Monte Carlo Simulation Tool for Hadronic Physics”. In: *PoS ACAT (2007)*, p. 076. DOI: 10.22323/1.050.0076. arXiv: 0708.2382 [nucl-ex].
- [39] S. Agostinelli et al. “GEANT4—a simulation toolkit”. In: *Nucl. Instrum. Meth. A* 506 (2003), pp. 250–303. DOI: 10.1016/S0168-9002(03)01368-8.
- [40] S. A. Bass et al. “Microscopic models for ultrarelativistic heavy ion collisions”. In: *Prog. Part. Nucl. Phys.* 41 (1998), pp. 255–369. DOI: 10.1016/S0146-6410(98)00058-1. arXiv: nucl-th/9803035.
- [41] W. Ehehalt and W. Cassing. “Relativistic transport approach for nucleus nucleus collisions from SIS to SPS energies”. In: *Nucl. Phys. A* 602 (1996), pp. 449–486. DOI: 10.1016/0375-9474(96)00097-8.
- [42] J.Adamczewski-Musch et al. [HADES Collaboration]. “Charged-pion production in Au + Au collisions at  $\sqrt{s_{NN}} = 2.4$  GeV”. In: *The European Physical Journal A* 56.10 (Oct. 2020). ISSN: 1434-601X. DOI: 10.1140/epja/s10050-020-00237-2. URL: <http://dx.doi.org/10.1140/epja/s10050-020-00237-2>.
- [43] R. Averbeck et al. “Neutral pions and  $\eta$  mesons as probes of the hadronic fireball in nucleus-nucleus collisions around 1A GeV”. In: *Phys. Rev. C* 67 (2 Feb. 2003), p. 024903. DOI: 10.1103/PhysRevC.67.024903. URL: <https://link.aps.org/doi/10.1103/PhysRevC.67.024903>.
- [44] Claudia Behnke. “Reconstruction of  $\pi^0$  and  $\eta$  Mesons via Conversion in 197 Au+ 197 Au at 1.23 GeV/u with the HADES Spectrometer”. PhD thesis. Frankfurt, 2016.
- [45] Erik Lins. “Entwicklung eines Auslese- und Triggersystems zur Leptonenidentifizierung mit dem HADES-Flugzeitdetektor”. ger. PhD thesis. Gießen, 2001. URL: <http://geb.uni-giessen.de/geb/volltexte/2001/440>.
- [46] Aleksander Glodkowski. “Analysis of Au+C contribution from reactions outside target in Au+Au run with HADES”. Darmstadt, 2019.
- [47] Mateusz Wasiluk. “Subtraction of Au+C contamination in Au+Au experiment with HADES using Machine Learning techniques”. Get Involved report. Darmstadt, 2019.
- [48] [Online; last accessed 16-November-2020]. URL: <http://web-docs.gsi.de/~misko/overlap/interface.html>.
- [49] Maximilian Justus Wiest. “Dileptons as probes of strongly interacting matter”. Master Thesis. Darmstadt, 2020.
- [50] Jaroslav Bielcik. “Dilepton spectroscopy with HADES”. PhD thesis. Darmstadt, Oct. 2004. URL: <http://tuprints.ulb.tu-darmstadt.de/489/>.
- [51] Jurgen Mifsud. “Optical Glauber Modeling in High-Energy Nuclear Collisions”. CERN, 2013.
- [52] Ariana Caiati. “Glauber Model Monte Carlo Simulation of Pb+Pb Collisions”. London, 2018.

- [53] Florian Seck. “Development of a Realistic Event Generator for In-Medium and QGP Dileptons”. Master Thesis. Darmstadt, 2015.
- [54] Patrick Seilheim and HADES Collaboration. In: *J. Phys.: Conf. Ser.* 599 (2015). URL: <http://iopscience.iop.org/article/10.1088/1742-6596/599/1/012027/pdf>.
- [55] G. Agakishiev et al. [HADES Collaboration]. “Dielectron production in Ar + KCl collisions at 1.76A GeV”. In: *Phys. Rev. C* 84 (1 July 2011), p. 014902. DOI: 10.1103/PhysRevC.84.014902. URL: <https://link.aps.org/doi/10.1103/PhysRevC.84.014902>.
- [56] K.A. Olive et al. “Review of Particle Physics”. In: *Chin. Phys. C* 38 (2014), p. 090001. DOI: 10.1088/1674-1137/38/9/090001.
- [57] A. Bialas, M. Bleszynski, and W. Czyz. “Multiplicity Distributions in Nucleus-Nucleus Collisions at High-Energies”. In: *Nucl. Phys. B* 111 (1976), pp. 461–476. DOI: 10.1016/0550-3213(76)90329-1.
- [58] Ulrich W. Heinz and Kang Seog Lee. “The rho peak in the dimuon spectrum as a clock for fireball lifetimes in relativistic nuclear collisions”. In: *Phys. Lett. B* 259 (1991), pp. 162–168. DOI: 10.1016/0370-2693(91)90152-G.
- [59] David J. Gross and Frank Wilczek. “Ultraviolet Behavior of Nonabelian Gauge Theories”. In: *Phys. Rev. Lett.* 30 (1973). Ed. by J. C. Taylor, pp. 1343–1346. DOI: 10.1103/PhysRevLett.30.1343.
- [60] N. Rathod et al. “Hyperon Studies and Development of Forward Tracker for HADES Detector”. In: *Acta Phys. Polon. B* 51 (2020), pp. 239–243. DOI: 10.5506/APhysPolB.51.239.
- [61] K. Zeitelhack et al. “The HADES RICH detector”. In: *Nucl. Instrum. Meth. A* 433 (1999). Ed. by A. Breskin, R. Chechik, and T. Ypsilantis, pp. 201–206. DOI: 10.1016/S0168-9002(99)00371-X.
- [62] C. Muntz et al. “The hades tracking system”. In: *Nucl. Instrum. Meth. A* 535 (2004). Ed. by M. Jeitler et al., pp. 242–246. DOI: 10.1016/j.nima.2004.07.232. arXiv: physics/0404011.
- [63] M Mamaev, O Golosov, and I Selyuzhenkov. “Directed flow of protons with the event plane and scalar product methods in the HADES experiment at SIS18”. In: *Journal of Physics: Conference Series* 1690 (Dec. 2020), p. 012122. DOI: 10.1088/1742-6596/1690/1/012122.
- [64] J. Adamczewski-Musch et al. “Identical pion intensity interferometry at  $\sqrt{s_{NN}} = 2.4$  GeV: HADES collaboration”. In: *Eur. Phys. J. A* 56.5 (2020), p. 140. DOI: 10.1140/epja/s10050-020-00116-w. arXiv: 1910.07885 [nucl-ex].
- [65] Gojko Vujanovic et al. “Dilepton emission in high-energy heavy-ion collisions with viscous hydrodynamics”. In: *Phys. Rev. C* 89.3 (2014), p. 034904. DOI: 10.1103/PhysRevC.89.034904. arXiv: 1312.0676 [nucl-th].
- [66] M. M. Aggarwal et al. “Azimuthal anisotropy of photon and charged particle emission in Pb-208 + Pb-208 collisions at 158-A-GeV/c”. In: *Eur. Phys. J. C* 41 (2005), pp. 287–296. DOI: 10.1140/epjc/s2005-02249-2. arXiv: nucl-ex/0406022.
- [67] Enrico Speranza, Amaresh Jaiswal, and Bengt Friman. “Virtual photon polarization and dilepton anisotropy in relativistic nucleus–nucleus collisions”. In: *Phys. Lett. B* 782 (2018), pp. 395–400. DOI: 10.1016/j.physletb.2018.05.053. arXiv: 1802.02479 [hep-ph].
- [68] Payal Mohanty et al. “Elliptic flow of thermal dileptons as a probe of QCD matter”. In: *Phys. Rev. C* 85 (2012), p. 031903. DOI: 10.1103/PhysRevC.85.031903. arXiv: 1111.2159 [nucl-th].
- [69] Charles Gale et al. “Production and Elliptic Flow of Dileptons and Photons in a Matrix Model of the Quark-Gluon Plasma”. In: *Phys. Rev. Lett.* 114 (2015), p. 072301. DOI: 10.1103/PhysRevLett.114.072301. arXiv: 1409.4778 [hep-ph].

- 
- [70] Jian Deng et al. “Dilepton flow and deconfinement phase transition in heavy ion collisions”. In: *Phys. Lett. B* 701 (2011), pp. 581–586. DOI: 10.1016/j.physletb.2011.06.027. arXiv: 1009.3091 [nucl-th].
- [71] R. Arnaldi et al. “First results on angular distributions of thermal dileptons in nuclear collisions”. In: *Phys. Rev. Lett.* 102 (2009), p. 222301. DOI: 10.1103/PhysRevLett.102.222301. arXiv: 0812.3100 [nucl-ex].
- [72] Behruz Kardan. “Collective flow measurements with HADES in Au+Au collisions at 1.23A GeV”. In: *PoS CPOD2017* (2018), p. 049. DOI: 10.22323/1.311.0049.
- [73] Rupa Chatterjee et al. “Exploring evolution of anisotropy with electromagnetic radiation”. In: *Indian Journal of Physics* 84.12 (Dec. 2010), pp. 1795–1799. DOI: 10.1007/s12648-010-0175-z.
- [74] J. Adams et al. “Azimuthal anisotropy in Au+Au collisions at  $s(NN)^{1/2} = 200$ -GeV”. In: *Phys. Rev. C* 72 (2005), p. 014904. DOI: 10.1103/PhysRevC.72.014904. arXiv: nucl-ex/0409033.
- [75] H. van Hees R. Rapp. “Thermal Dileptons as Fireball Thermometer and Chronometer”. In: *Phys. Lett. B* 753 (2016), pp. 586–590. DOI: 10.1016/j.physletb.2015.12.065. arXiv: 1411.4612 [hep-ph].
- [76] David J. Griffiths. *Introduction to elementary particles*. 1987. ISBN: 9783527618460.